Device Physics of Two-Dimensional Crystalline Materials

Sanfeng Wu

A dissertation

submitted in partial fulfillment of the

requirements for the degree of

Doctor of Philosophy

University of Washington

2016

Reading Committee:

Xiaodong Xu, Chair

David Henry Cobden

Anton Andreev

Subhadeep Gupta

Program Authorized to Offer Degree:

Department of Physics

University of Washington

Abstract

Device Physics of Two-Dimensional Crystalline Materials

Sanfeng Wu

Chair of the Supervisory Committee:
Associate Professor Xiaodong Xu
Department of Physics

The study of two-dimensional (2D) electrons in condensed matter physics has two milestones: quantum Hall effects in semiconductor heterostructures and superconductivity in cuprates. In both, the 2D electrons are embedded in complex material structures. The discovery of graphene allows for the isolation of 2D electrons in their simplest form, existing merely in a single crystalline atomic layer and exposing the states to external controls. Triggered by graphene, the interest in a variety of other 2D crystals, such as atomically thin transition metal dichalcogenides (TMDs), has recently exploded, revising the physics of 2D electrons in the ultimate confinement limit. At the same time, constructing heterostructures based on 2D crystals, either by placing the atomic layer on a special substrate or by combining different 2D crystals together, promises a bright future for observing novel electronic phenomena and engineering new device functionalities. In this thesis, the device physics of atomically thin semiconducting TMDs, such

as MoS_2, $MoSe_2$ and WSe_2, and semi-metallic graphene will be explored, in the form of both individual crystals and heterostructures. We show how these 2D crystalline systems can give rise to unique electronic behaviors and also application potentials by demonstrating the possibility of 2D-crystal based valleytronics, nanoscale lasing, and multiple photo-excited carrier collection. Subsequently, we demonstrate a scalable way to synthesize TMD monolayers, as well as a method to achieve epitaxial growth within an atomic plane, leading to the formation of lateral semiconductor heterostructures in 2D.

TABLE OF CONTENTS

LIST OF FIGURES

LIST OF TABLES

ACKNOWLEDGEMENTS

I thank my Ph.D. advisor, Prof. Xiaodong Xu. Back in the spring of 2010, I was struggling with my graduate school application while I was doing undergraduate research in Prof. Jiangfeng Du's lab at University of Science and Technology of China. One day, Du told me that a former "undergraduate superstar" in his group was going to start a lab in Seattle, and he recommended that I join the new lab. The superstar was Xiaodong. Shortly after, Xiaodong and I talked over phone for the first time and it was this phone call that started my journey into graduate research. No doubt, it was the most important and influential phone call that I have ever made because it set the initial conditions for all the evolutions in the following years. Xiaodong has created an excellent research environment in the lab. He is a great scientist with a super-efficient work ethic. His exceptional intuition in science and his enthusiasm always inspired me and guided me. He has always been supportive and responsive, and has always tried his best to shape me into the excellent. I have obtained the best education and scientific training from him. It is my best luck to work with him, learn from him, be shaped by him and be friends with him.

I thank Prof. David Cobden. Dave is my second advisor during this Ph.D. study. I cannot count how many hours I have spent in his lab searching, transferring, wire bonding, AFMing, spin-coating, talking, reading, and sleeping. He is always encouraging and supportive. I was so lucky to have so many discussions with him and to write several papers together with him. He has an excellent taste of what good science is and what a good scientist should be. I have learned from him not only talking and writing skills but also his attitude towards science.

I thank my committee members, Prof. Anton Andreev and Prof. Subhadeep Gupta. Anton is so knowledgeable and is always there if I have any questions. It is most enjoyable to join or listen to discussions with a theorist like Anton. I enjoyed so much in Deep's class that I have always dreamed about connecting my own research to his field of atomic physics. I thank Deep for being so patient helping me in class, with practice for my job talk, and for joining my thesis committee.

I thank all of my collaborators whom I have had the immense pleasure of working with: Prof. Wang Yao and Prof. Di Xiao were our theoretical backbone; Dr. Jiaqiang Yan, and Dr. David Mandrus provided the best samples of all kinds; Dr. Takashi Taniguchi and Dr. Kenji Watanabe gave us their quality-guaranteed BN crystals; Dr. Ana Sanchez and Prof. Richard Beanland let us see the amazingly beautiful lattice structures of our grown monolayers; Prof. Arka Majumdar, Prof. Jelena Vučković and Dr. Sonia Buckley fabricated high quality photonic crystal cavities; Prof. Zhiqiang Li and You Lai were always ready to help in Maglab; Prof. James Hone, Prof. Cory Dean and Dr. Lei Wang had generously shared their world-class graphene devices. Thank you all!

I thank all my labmates, past and present. Without these talented people, my thesis would be impossible to complete. Thanks to: Dr. Grant Aivazian, Dr. Xinhan Cai, Dr. Chunming Huang, Dr. Aaron Mitchel Jones, Dr. Jason Ross, Dr. John Schaibley, Genevieve Clark, Boris Dzyubenko, Zaiyao Fei, Bevin Huang, Paul Nguyen, Pasqual Rivera, Marie Scott, Kyle Seyler, Jacob Watkins, Nathan Wilson, and Ding Zhong. Without these people, research wouldn't be fun and life wouldn't have been so fun. Thanks to Grant for cooking the most delicious deep-fried turkeys for Thanksgiving. Thanks to Mitch for teaching me many tips for optics. I thank Jason

for writing EBL for me so many times. I thank many of you for every poker night (and sorry that I have won so many times)!

I thank all my friends in Seattle. Life is so enjoyable because of all the fun that we have made, gaming, hiking, cooking and road tripping Thank you for providing such a bright side of life, which is otherwise dark in the optics lab or the rainy Seattle streets.

I thank my family. Perhaps the thing that worries my Dad and Mom the most is my safety in the states. The frequent gun-shooting news from US always worried them. Thank you to Mom and Dad, for your never-ending support and love! And finally, thank you to my fiancée, Yue, for so many great moments that we have spent together and for every sweet thing that you have done for me!

DEDICATION

To my father and mother,

for their never-ending love and support.

Chapter 1. INTRODUCTION TO 2D ELECTRONIC SYSTEMS

Two of the hallmark discoveries in modern condensed matter (CM) physics are the integer/fractional quantum Hall effects (QHE) and the high temperature superconductivity (High-Tc). Intriguingly, the essential ingredients in the hosting material systems of the two discoveries are similar: electrons that are highly mobile in two directions but not in the third direction (i.e., a layer of 2D or quasi-2D electrons). The QHE was observed in the low-density region of the electron gas ($10^{10} \sim 10^{12}$ cm^{-2}), while the High-Tc was observed in the high-density region ($\sim 10^{14}$ cm^{-2}). After decades of development, the physics of QHE is now relatively well understood, with the exception of a few extraordinary states, while the underlying picture of High-Tc is still hotly debated. Concepts derived from both phenomena are rich. These include topological order, symmetry protected topological phases and quantum spin liquids, highlighting the central themes of current CM research. Many of these fascinating concepts are still in their infancy. Hence, experimentally searching for new 2D electronic systems distinct from the conventional ones, under variant density regimes, is of great interests in solving the long-standing mysteries (such as High-Tc), as well as establishing new physics.

This could also potentially benefit the next generation of electronics, photonics and optoelectronics, because 2D electrons are also essential to a variety of modern semiconductor technologies, such as transistors, light-emitting diodes, and lasers. New 2D electronic system, especially with simplified material constructions, could possibly provide solutions to improve, at least in some aspects, the semiconducting technologies existing today. In this chapter, we will first review the conventional 2D electronic systems and then introduce a class of atomically thin crystals as a new form, and more importantly, perhaps the simplest form, of material systems that

host 2D electrons. The focus of this thesis will be on the 2D crystals that host relatively low electron densities, and exhibit either metallic or semiconducting phases. Additionally, some excellent samples in the high-density regime will be pointed out without exploring their physics in great detail.

1.1 CONVENTIONAL 2D ELECTRONIC SYSTEMS

There are two categories of the conventional 2D electronic systems. In one kind the 2D electrons are induced at heterojunctions of different 3D bulk materials. Examples include metal-oxide-semiconductor structures used in field effect transistor (FET), GaAs heterostructures and oxide interfaces (upper panel, Figure 1.1). In the case of GaAs semiconductor heterojunctions, a 2D electron gas can be induced by band bending and remote doping effects, which creates a layer of 2D electron gas in the intrinsic GaAs layer. Such structures play a key role in observing fractional QHE and also in developing high electron mobility transistors. In the case of oxides interfaces (e.g. $LaAlO_3/SrTiO_3$ interface), although the exact mechanism is not yet known, the induced 2D electrons have led to several unique behaviors that are not expected from their 3D bulk, including the emergence of superconductivity. The second category includes those (quasi-) 2D electrons that exist naturally in layered compound structures. The best examples may be the two classes of High-Tc materials, i.e., cuprates and the iron-based superconductors (lower panel, Figure 1.1). Electrons in these materials essentially move only in 2D planes (copper-oxide plane or the iron-pnictide / iron-chalcogenide planes).

While exhibiting fascinating phenomena, these conventional systems, however, are rather complicated. Although the physics is essentially within the 2D atomic planes (e.g. High-Tc materials), the multilayer construction certainly adds complexity to the theoretical understanding

of the materials. Also, the induced 2D electrons are hidden and embedded in 3D systems, leaving very limited room to manipulate and tailor their properties.

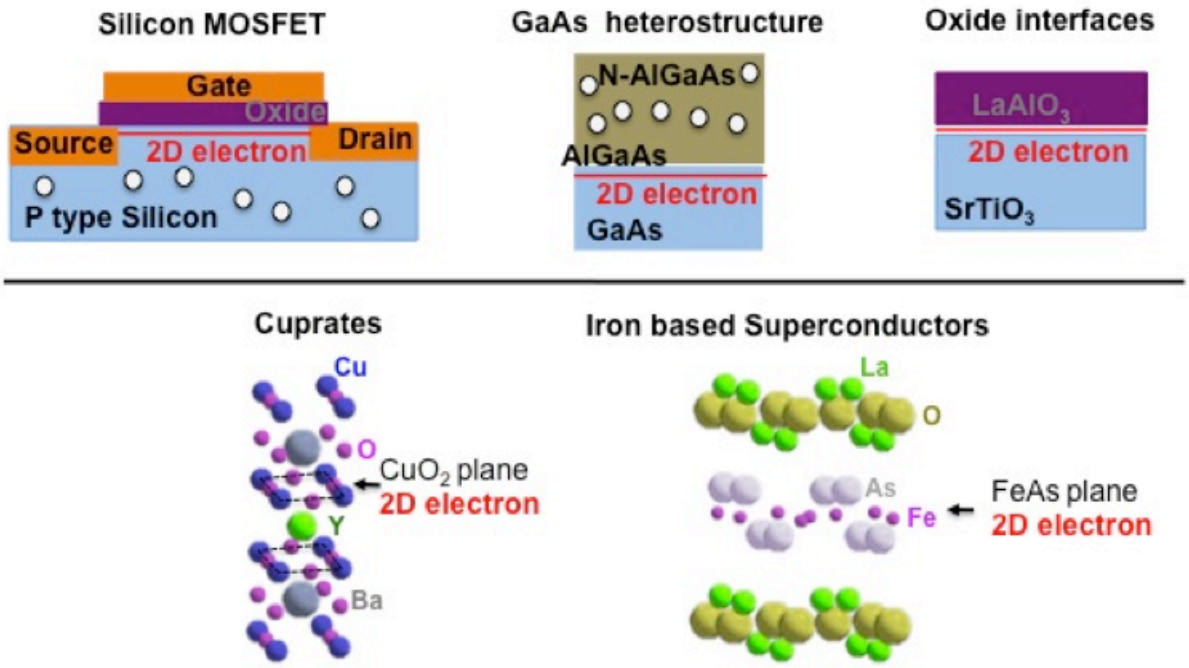

Figure 1.1. Conventional material systems hosting 2D electrons. Upper panel: 2D electronic systems induced at heterojunctions of 3D bulk materials, exhibiting QHE and superconductivity. Lower panel: typical 2D electronic systems naturally formed in layered compounds, exhibiting High-Tc superconductivity.

1.2 THE SIMPLEST: 2D CRYSTALLINE GRAPHENE

The discovery of graphene provides a unique way to isolate the 2D electrons from complicated material systems to perhaps their simplest existence, consisting of merely a single atomic layer (*1*). In graphene, carbon atoms occupy a 2D hexagonal lattice, where the simple tight binding model captures essential aspects of its electronic structure: two linearly dispersed (Dirac) cones located at the six corners (K points) of its hexagonal Brillouin zone (BZ). Immediately after its

synthesis, the integer QHE (*2*, *3*) and the fractional QHE (*4*), the hallmark physics of 2D electrons at low-density end, were observed in graphene, demonstrating the high quality of the 2D electrons in such atomically thin crystals. The ongoing research of graphene is revising the physics of QHE, especially when one considers the recent observations in graphene superlattices (*5*–*8*) (see Section 1.4).

1.3 A LIBRARY OF 2D CRYSTALS

The method to obtain single layer graphene, i.e., mechanical exfoliation, is not limited to this particular structure. It is universally applicable to all the layered materials stacked by van der Waals force. Consequently, a large number of single layer crystals can be extracted from their layered bulks, giving rise to a library of 2D crystals (*9*, *10*) (Table 1.1). The electronic structures and properties of these crystals spread over a broad range, whose phases include semimetal (graphene, etc), insulator (Boron nitride, etc), semiconductor (MoS_2, etc) and strongly correlated states such as density waves (TaS_2, etc) and superconductivity ($NbSe_2$, etc). Future developments may also lead to the examination of 2D magnetic materials and 2D crystals exhibiting topological phases. Only a small portion of these 2D crystals have been studied to date and they have already demonstrated fascinating physics and application potentials. Many of them, however, are still unexplored and there may be a significant number of crystals are not listed in the table. Hence, we should not be surprised if, in both the near and distant future, certain currently unexplored 2D crystal may arise as new superstars or as new platforms exhibiting novel phenomena.

Many 2D crystals are chemically unstable, e.g., they will easily be oxidized after being exposed to ambient environment. Examples include $NbSe_2$, WTe_2, and $TiSe_2$ etc. The single layers are sometimes extremely fragile and even under the encapsulation with hexagonal boron

nitride (hBN) they can still oxidize easily. This creates difficulties in fabricating devices. Such problem can be overcome using of nitrogen glove box, which allows almost entire fabrication procedures to be in inert atmosphere and paves the way to uncovering the intrinsic physics of fragile crystals.

Table 1.1.. A library of 2D crystals. Taken from Ref. (*10*), with permission.

<table>
<tr><td>Graphene family</td><td>Graphene</td><td colspan="2">hBN
'white graphene'</td><td>BCN</td><td>Fluorographene</td><td>Graphene oxide</td></tr>
<tr><td rowspan="2">2D chalcogenides</td><td colspan="2" rowspan="2">MoS_2, WS_2, $MoSe_2$, WSe_2</td><td colspan="2" rowspan="2">Semiconducting dichalcogenides:
$MoTe_2$, WTe_2,
ZrS_2, $ZrSe_2$ and so on</td><td colspan="2">Metallic dichalcogenides:
$NbSe_2$, NbS_2, TaS_2, TiS_2, $NiSe_2$ and so on</td></tr>
<tr><td colspan="2">Layered semiconductors:
GaSe, GaTe, InSe, Bi_2Se_3 and so on</td></tr>
<tr><td rowspan="2">2D oxides</td><td>Micas, BSCCO</td><td colspan="2">MoO_3, WO_3</td><td colspan="2" rowspan="2">Perovskite-type:
$LaNb_2O_7$, $(Ca,Sr)_2Nb_3O_{10}$,
$Bi_4Ti_3O_{12}$, $Ca_2Ta_2TiO_{10}$ and so on</td><td>Hydroxides:
$Ni(OH)_2$, $Eu(OH)_2$ and so on</td></tr>
<tr><td>Layered Cu oxides</td><td colspan="2">TiO_2, MnO_2, V_2O_5,
TaO_3, RuO_2 and so on</td><td>Others</td></tr>
</table>

1.4 HETEROSTRUCTURES BASED ON 2D CRYSTALS

In contrast to the conventional systems, electronic states in 2D crystals are completely exposed to external environment and controls. This is a great advantage because one can tune or manipulate the states in much more direct ways and with many more degrees of freedom. Firstly, field effect, such as electrostatic doping and potential, can be very significant. Its power has been repeatedly demonstrated in devices of graphene field effect transistors (FET). Secondly, the single atomic layers can be placed on top of any surface, constructing unique heterostructures that do not exist in nature. For example, the substrates could be another 2D crystals, which will consequently form atomically thin van der Waals heterostructures(*10*). Such engineered interface can provide remarkable opportunities in observing novel phenomena. This is impossible for conventional systems.

Two great examples of heterostructure must be mentioned here. The first is about the physics at the low density-end: by placing graphene on top of an hBN substrate with precise lattice alignment, a long wavelength moiré superlattice forms and gives rise to an elegant demonstration of the long-pursued Hofstadter's butterfly (*5*–*7*). The observed Hofstadter's spectrum is described by two quantum numbers, the Bloch filling factor and the Landau filling factor, instead of one in the conventional QHE, and it leads to fractal QHE (*5*). Interestingly, both quantum numbers can be fractionalized due to interaction effects, but the mechanism is currently unknown (*8*), representing new aspects of QHE. The second is about the physics at the high electron-density end: by placing a piece of single layer iron selenide (FeSe) on top of an $SrTiO_3$ substrate, one can achieve a remarkably enhanced superconductivity transition temperature (~100 K) in the system compared to its bulk (~8 K) (*11*). These results differ strikingly from expectations because reducing the thickness usually decreases the transition temperature, a consequence of the enhanced effects from thermal fluctuations. Such interface engineered 2D superconductivity has not only inspired a new way to search for High-Tc systems but also highlighted the power of heterostructure engineering based on 2D crystals. These examples, of course, are just the beginning of 2D interface engineering. For observing and discovering unique phenomena, one only needs imaginations, to wisely pick up the right crystals, the right substrate and combine them in the right way.

1.5 THE FOCUS OF THIS THESIS

The focus of this thesis will be the device physics in graphene and atomically thin transition metal dichalcogenides (TMDs), and the interface effects arising in their heterostructures. The contents will be divided into several disciplines that may benefits from 2D crystals:

valleytronics, nano-photonics, and optoelectronics. We will also discuss the scalable growth of 2D materials. The chapters will follow these disciplines.

In the second chapter, we will introduce how a new external degree of freedom, namely valley pseudo-spin, emerges in the 2D semiconducting TMDs such as MoS_2. The valley-associated physics provides a key ingredient to understand the electronic and optical properties of this class of materials, such as the formation and dynamics of valley excitons. Interestingly, such valley excitons naturally offer a means to initialize, manipulate and read out the states of valley pseudo-spin, potentially allowing for a new way of informatics. This is now termed as "valleytronics". We will also demonstrate how one can tune the valley-associated physics by symmetry control in bilayer TMDs.

In the third chapter, we will explore interface effects between monolayer TMDs and a special substrate, namely photonic crystals (PhCs) and cavities (PhCCs). We show that, by placing a piece of monolayer TMD on top of a PhCC, spontaneous emission rate of the 2D emitter can be enhanced significantly and we consequently observed the signatures of nanoscale lasing in a high quality version of such heterostructures. Compared to the conventional nanolaser systems, such as the quantum-well or quantum dots / PhCC coupled system, there are obvious advantages by using 2D crystals, including scalability and compatibility with existing electronic technologies. These observations therefore highlight a promising routine for on-chip nanophotonics based on 2D crystal.

In the fourth chapter, we will explore the optoelectronic response of graphene/hBN heterostructures. In such structures, the formation of long-wavelength morié pattern gives rise to dramatic band engineering, the generation of secondary Dirac points and a fractal quantum spectrum (i.e., the Hofstadter's butterfly). We will demonstrate that van Hove singularities

(VHSs) emerge in the low-energies spectrum of the structure and lead to an enhanced photo-response. At low magnetic field, the zero-bias photoresponsivity of such a graphene photodetector (based on photo-Nernst effect) is remarkably enhanced, leading to multiple carrier collection per absorbed photon. At high magnetic fields, the photocurrent generation turns out to be a good indicator of the topological transitions in the fractal quantum Hall systems, including both the step transitions of Chern number at Landau levels and the collapse of Chern numbers at VHSs.

In the fifth chapter, we will introduce a scalable method to grow the monolayer semiconducting MX_2 (M=W, Mo; X=Se, S). The scalable synthesis of 2D materials is necessary because the production yield from mechanical exfoliation is too low to be suitable in any future applications. Our method is based on physical vapor deposition (PVD), in contrast to the popular chemical vapor deposition (CVD). We will show our results by demonstrating the growth of single-layer flakes, bilayer flakes and also the continuous single-layer films. Based on PVD, we will also introduce a method for 2D epitaxial growth, which results in the formation of seamless lateral heterojunctions between two different monolayer semiconductors. This may eventually leads to electronic and photonics devices integrated within a single atomic plane.

Chapter 2. 2D VALLEYTRONICS: EXCITONS IN MONOLAYER SEMICONDUCTORS

In this chapter, we introduce the 2D semiconducting TMDs along with their valley-associated physics by examining their optical properties.

2.1 MONOLAYER SEMICONDUCTING TMDS

Group VI transition metal dichalcogenides (TMDs), with chemical formula MX_2 (M=Mo, W; X=S, Se), are of layered van der Waals structure. Mechanical exfoliation can be used to obtain their atomically thin crystals, down to the monolayer (see optical image in Fig. 2.1a) and bilayer limit. Owing to their unique physical and chemical properties (*12*, *13*), the monolayer and bilayer crystals have attracted much attention recently as a new class of 2D crystals. The monolayer TMD, viewed from above, has a hexagonal lattice structure (with trigonal prismatic coordination) in its 2H form, similar to graphene (*14*). However, the A and B sublattices are occupied by different atoms in TMDs, while in graphene they are the same. This leads to inversion symmetry breaking (ISB) in the TMD monolayer lattice, in contrast to the inversion symmetric graphene, as show in Fig. 2.1b and c.

The band structure of graphene, as shown in Fig. 2.1d, describes degenerate massless Dirac fermions at low energies, located at two indistinguishable corners (K and –K valleys) of the first Brillion zone (BZ). The ISB in TMD monolayer alters two fundamental properties of its band structure (Fig. 2.1e) (*14–16*). (1) A direct band gap opens in the visible regime at the K and –K valleys. (2) Equivalency between K and –K is broken, and the valleys become distinguishable experimentally due to the emergent Berry phase effects (detail in section 2.4). The first aspect defines TMD monolayers as 2D semiconductors. This then allows for the

potential development of many useful devices out of these ultrathin materials, such as solar cells (*17*, *18*), transistors (*19*), photo-detectors (*20*), light emitting diodes (LED) (*18*, *21–23*) and even nanoscale lasers (*24–26*). The second aspect allows for the emergence of a new, external and measurable degree of freedom for electrons residing in the crystals, i.e., the valley pseudo-spin degree of freedom (*14*, *27–30*) (see section 2.3, 2.4). Rich physical consequences, as well as potential device applications utilizing such valley pseudo-spin will be discussed in the following sections.

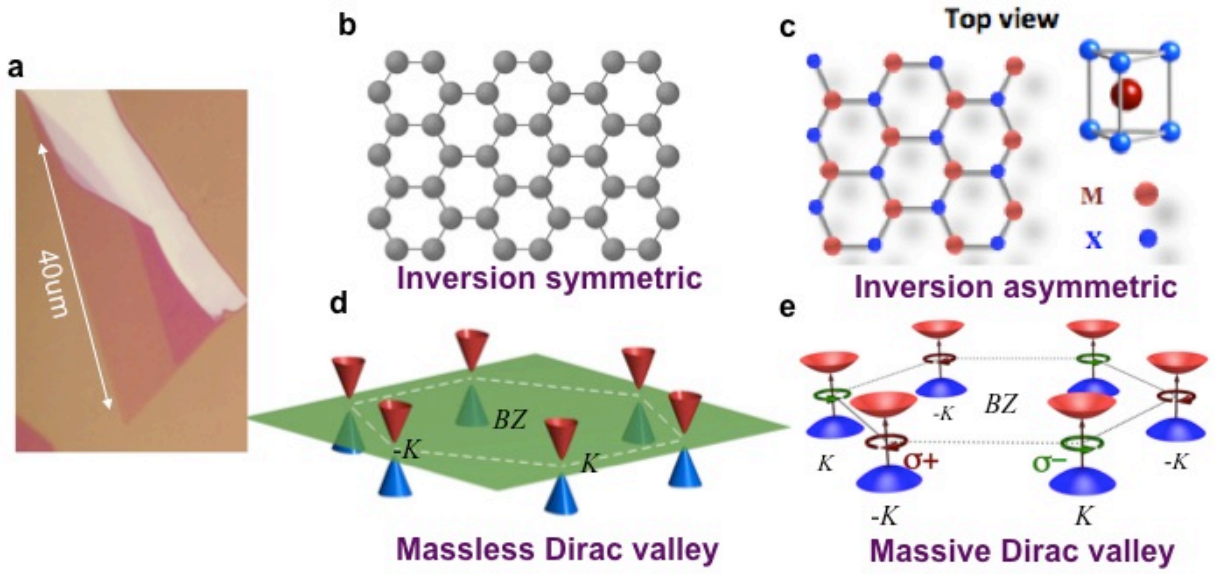

Figure 2.1. Crystal and band structures of graphene and monolayer 2H-MX_2. a, optical image of a single layer WSe_2, mechanically exfoliated on SiO_2 substrate. b, crystal structure of graphene, showing hexagonal lattice with C atoms occupying the sites. c, top view of 2H-MX_2 monolayer lattice, similar to graphene but the sub-lattice are occupied with different atoms. Such configuration thus breaks the space inversion symmetry, in contrast to graphene. d, Low energy band structure of graphene, depicted by the massless Dirac valley at the BZ corners. e, low energy band structure of 2H-MX_2, with band-gap opening in visible. The gapped (massive) Dirac cones are selectively accessible by circularly polarized light, giving rise to valley optical selection rule (details in section 2.2 and 2.3).

2.2 EXCITONS: FINGERPRINTS OF 2D SEMICONDUCTORS

Due to the visible band-gap opening, TMD monolayers are shining new light on semiconducting physics in new ways. One such aspect is the emergence of novel optical properties of semiconductors with reduced thickness. Optical excitations create electrons and holes in semiconducting materials, while reducing thickness leads to a strong quantum confinement favoring new bound states of attracting electrons and holes (*31*, *32*). Such bound states, which are very similar to hydrogen atoms and ions, are called excitons (Fig. 2.2). A charge-neutral exciton (X^o) is a quasi-particle made up with one electron and one hole bound through their coulomb force, analogous to a hydrogen atom. Charged exciton species can also exist by arresting an additional electron (or hole) to form a three-body bound state (trions) X^- (or X^+), analogous to H^- (or H_2^+). These excitonic quasi-particles are the key to understanding many optical properties of semiconductors and therefore play an important role in a variety of photonics and optoelectronic applications.

One of the essential systems for the observation of excitonic behavior is the conventional (quasi-) 2D semiconducting system, such as quantum wells (*33*), where the electron wavefunctions are typically confined down to tens or hundreds of nanometers by constructing heterostructures. While rich excitonic physics have already been revealed in these systems, the relatively low binding energies and broad spectral width limits our access to tune and utilize the exciton physics. Observations and control of excitons in the ultimate limit of thickness (atomically thin, sub-nanometer) has been an outstanding goal for a long time, motivated by the strong confinement and the expected large exciton and trion binding energies in the 2D limit.

We realize this goal in monolayer TMDs (*31*). In particular, we discuss our observations in monolayer $MoSe_2$ here. In monolayer form, the wavefunctions of low energy electrons located

at the band edges at K and –K valleys are estimated to be strongly confined in the metal layer within ~ 0.2 nm in the direction perpendicular to the plane, representing the ultimate 2D limit. We then investigate the optical response of monolayer samples by differential reflectance and micro-photoluminescence (PL) measurements. The monolayers have also been fabricated into field effect transistors on doped-Si/SiO_2 substrate, where the doping density in the 2D crystal can be continuously tuned from negative to positive by applying gate voltages to silicon. Details of the measurements and data can be found in Ref.(*31*). Here we summarize our main findings.

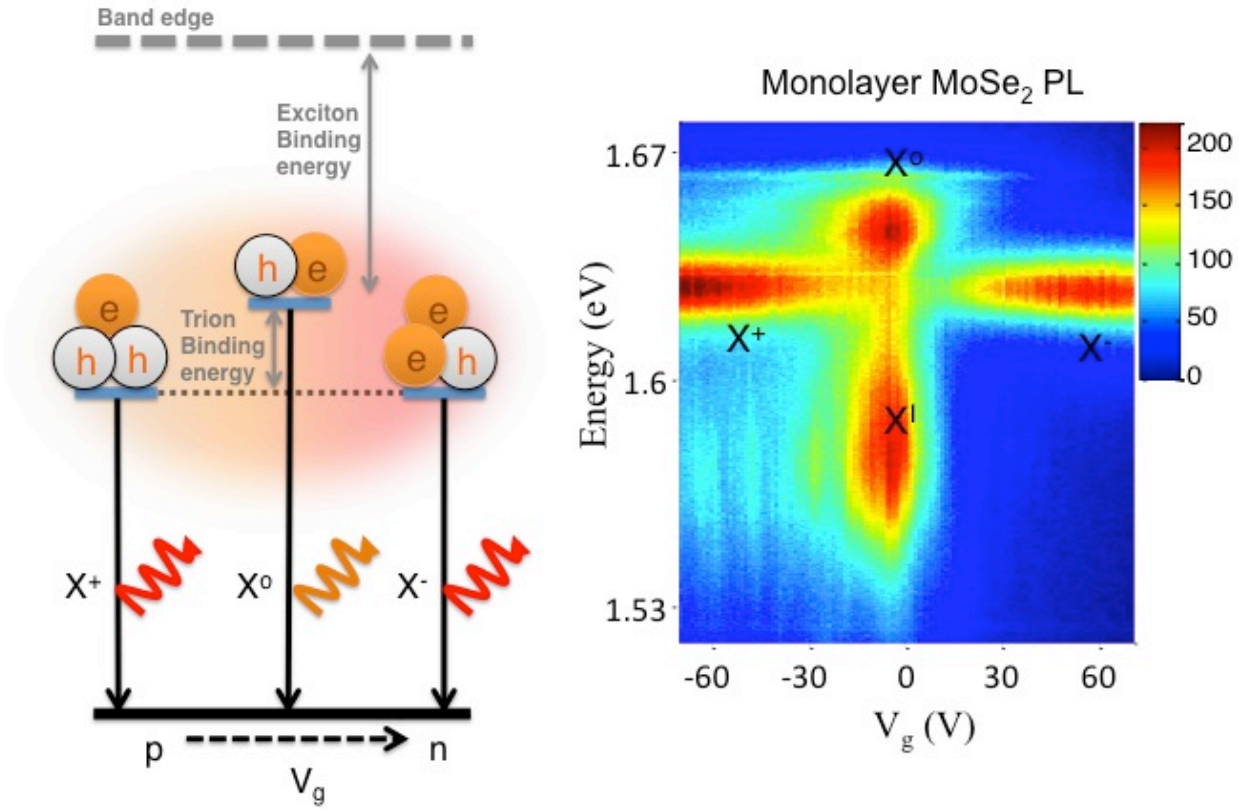

Figure 2.2. 2D excitons. Left, energy diagram of excitons and trions. Right, PL color map of monolayer $MoSe_2$, taken at 30K, showing the islands of emissions that are associated with different exciton spicies.

Figure 2.2 (right panel) shows a PL color map in axes of photon energy and gate voltage. The isolated emission islands in the map clearly reveal that, under different doping (gate) conditions, it is the excitonic quasi-particles that dominate the emissions. At around zero gate (charge neutral), the emission is in relatively high energies together with a broad low energy tail. We identify this higher energy peak as charge neutral excitons (X^o) and the low energy tail corresponds to the impurities or defects bound excitons. At negative gates (< -15V, p doped), it is the positively charged trions (X^+) that are responsible for the PL, while at the positive gate (> 0V, n doped) the negatively charged trions (X^-) dominate. These identifications are further supported by reflection measurements and temperature dependent measurements in ref. (*31*).

We here highlight two exceptional features revealed by the observations. First, the exciton and trion peak separation are about 30 meV (trion binding energy). This is much larger than the typical numbers reported for GaAs quantum wells (*33*). It also indicates that the exciton binding energy is about 250 meV, assuming the hydrogen model. Such binding energies are remarkably large, leading to the robust exciton species even at room temperatures. Second, the peak width are narrow, ~ 5 meV for X^o at low temperature. This allows for the observations with high spectral contrast and thus allows for us to distinguish fine features and uncove the physics hidden in conventional systems, such as exchange interaction, and spin splitting, etc.

The observed excitonic physics here are universal to all the semiconducting TMD monolayers, MoS_2, $MoSe_2$, WS_2, and WSe_2. Similar observations have been reported in all of them (*31*, *32*, *34–37*). Due to the different band gaps, exciton peaks are located at different energies for different monolayers, and therefore serve as fingerprints of these 2D semiconductors. In addition to excitons and trions, the observation of other quasi-particles, such

as bi-exciton (*38*) and exciton-polaritons (*39*, *40*) is also possible in these ultimately thin materials.

2.3 VALLEY EXCITONS AND OPTICAL PROPERTIES

Intriguingly, these excitons live in the Dirac valleys. As we have discussed in section 2.1, the low energy band structure of monolayer TMDs consists of valleys at BZ corners. Optical excitations with energies close to the band edge will generate electrons and holes at the conduction and valence bands with the same valley index (K or -K). These electrons and holes will then relax to the band edges, forming excitons (*41*). The inter-valley carrier-scattering process is suppressed under low-temperature and high sample quality because the two valleys are located far away from each other in momentum space. The bright excitons (i.e., the excitons that emit efficiently) recombine directly. This suggests that excitons that are observed through our PL spectra consist with electrons and holes living in the same valley, K or –K, and are correspondingly named as valley-excitons (Fig. 2.3a) (*41*, *42*). The inter-valley excitons (e.g., e from K and h from –K separately), if they exist, are dark since they require assistance from phonons to emit.

A direct piece of evidence for the existence of valley excitons is the observation of co-polarized PL emission with the excitation (*28–30*, *43*). Fig. 2.3b and c shows the polarization-resolved PL spectra of monolayer MoS_2, taken at 30K, under circularly polarized excitations, σ^+ or σ^-. The high-energy peak (at ~ 650 nm) is identified as free exciton emission and the broad low-energy peak (~ 710 nm) is from the impurities bands (bound excitons). We find that the free exciton peaks are highly polarized in the same manner as the incident laser. This co-polarized emission is unusual, because in general the carriers that are responsible for PL emission have already relaxed, which will remove their memory of the initial excitation.

However, in the case of monolayer TMDs, the helicity of the incidence is well memorized by photo-excited carriers until their recombination.

To understand this process, one needs to adapt the picture of valley-contrasting optical selection rule, i.e., the two valleys are associated with opposite circular dichroism (*14*). Under $\sigma^+(\sigma^-)$ excitation, only electrons at the K (-K) valley will be excited and the generated carriers remain in the same valley due to the weak inter-valley scattering, forming valley excitons after relaxation. These valley excitons emits with the same helicity that is defined by their valley index. Under this picture, it is the discrete (i.e., well-separated) valley index that protects the optical helicity from loss.

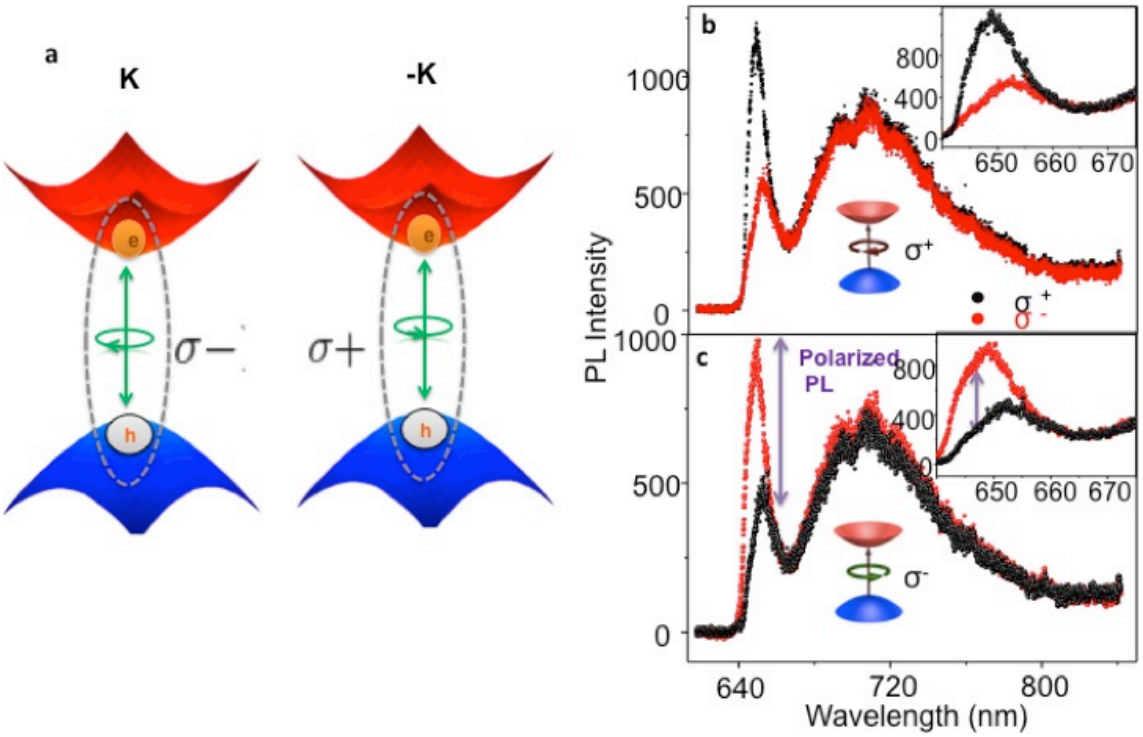

Figure 2.3. Valley excitons in monolayer MoS_2. a, The bright excitons lives in direct-gap valleys, assuring that the electron and hole can recombine without the assistant of phonons. b and c, PL emission at 30K. The excitation laser (632 nm) was circularly polarized (b, σ^+; c, σ^-). The spectra were recorded selectively with cross- and co-polarization, demonstrating a co-polarized

emission with the excitation at the free exciton emissions, but not the emissions associated with the bound excitons.

Indeed, the valley-contrasting optical selection is real. In the next section, we will discuss how such unusual phenomena can arise universally in the monolayer TMDs. We note that the observed co-polarized PL emission has been established not only in MoS_2, but also in WSe_2 and WS_2. However, in the case of $MoSe_2$, no such observation has been made so far, which still challenges our understanding of this particular system.

2.4 INVERSION SYMMETRY AND VALLEY MAGNETIC MOMENT

The valley-contrasting optical selection rule exists is a result of the carriers in different valleys acquiring magnetic moment (**m**) and Berry curvature (**Ω**) with opposite signs. This can be understood by symmetry analysis. The Berry phase related properties, **m** and **Ω**, are related to time reversal symmetry (TRS). If a system preserves TRS, then the total magnitude of the pseudovectors, **m** as well as **Ω**, have to be zero. Consequently, in the case of the two valleys in the BZ, they have the same magnitude, but different sign, in opposite valleys: **m** (k) = - **m** (-k); **Ω** (k) = - **Ω** (-k). If at the same time the spatial inversion symmetry (IS) is also presented, then **m** (k) = **m** (-k); **Ω** (k) = **Ω** (-k), since k and –k are related by spatial inversion. This then leads to zero value for **m** and **Ω** everywhere in the BZ. Such trivial case describes graphene, except that the exact Dirac points are singular valued, instead of zero. The two valleys in graphene therefore cannot be distinguished.

In order to achieve valley contrasting physics, the IS needs to be broken, so that **m** and **Ω** can be nonzero and acquire a valley dependent sign. The theoretical studies of such a case by breaking IS in graphene were performed as early as 2007 (*15*) and 2008 (*16*). However, it wasn't

sure how to experimentally induce such IS broken in graphene at the time. Now, about 8 years later, we have known at least three methods to achieve this goal. (1) A monolayer TMD is naturally analog to IS-broken graphene (*14*). Therefore the valley contrasting physics emerges. (2) When single layer graphene is placed on BN substrate with precisely aligned crystal lattice, a long-wavelength Moiré superlattice forms, inducing the IS breaking in graphene and opening up a bandgap at Dirac points (*6*). With such a structure, the valley-contrasting physics will also arise (*44*). In chapter 4, we will describe this system in detail. (3) When bilayer graphene is placed in an out of plane electric field, IS is broken and a bandgap is opened up in the infrared region (*45*). In this case, valley physics also become available (*46*).

Here we focus on TMD case, which is the first among the three realized platforms for observing valley-contrasting physics. The direct consequence of the valley contrasting magnetic moment is the valley optical selection rule, in which the opposite valleys will respond to optical excitations with opposite helicity (*14*). And this indeed naturally explains our observation in the polarization resolved PL measurements, as we have discussed previously (section 2.3). In the next section, we will try to summarize the physics associated with valley index in TMD monolayers, and conclude that this external pseudo-spin degree of freedom of electrons actually behaves like the real spin (*27*).

2.5 VALLEY POLARIZATION AND VALLEY COHERENCE

One conclusion from the above PL measurements is that we have an optical access to address and read out the valley index. We label $P(\sigma^+)$ and $P(\sigma^-)$ for the detected PL intensity associated with the corresponding helicity and the degree of circular polarization can be defined as $\eta = \frac{P(\sigma^+)-P(\sigma^-)}{P(\sigma^+)+P(\sigma^-)}$ (*43*). This circularly polarized exciton emission originates from the valley-

contrasting optical selection rules and η is determined by both the circular dichroism of the absorption process and the subsequent depolarization process. The degree of circular dichroism is determined by the valley magnetic moment **m** (k), which arises due to the IS as discussed in the previous section.

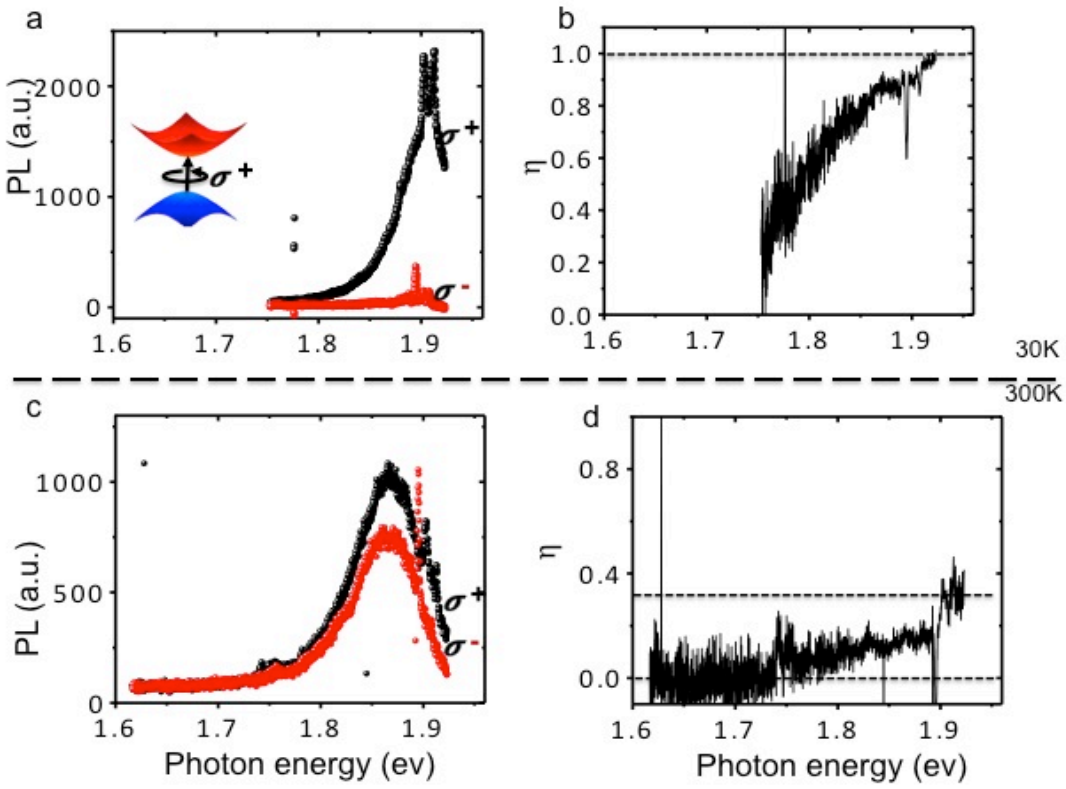

Figure 2.4. Near-unity valley polarization and room temperature valley polarization in physical vapor grown MoS_2. a, Circular-polarization resolved PL taken at 30 K under σ^+ excitation. b, The calculated η as a function of emission energy. c and d, similar data taken at room temprerature.

In the 2D honeycomb lattice of TMDs, the momentum-resolved circular dichroism of direct optical absorption at ±K valleys can be calculated by $\chi(k) = \frac{|P_+^{ns}(k)|^2 - |P_-^{ns}(k)|^2}{|P_+^{ns}(k)|^2 + |P_-^{ns}(k)|^2}$, where $P_\pm^{ns}(k) = \langle u_s(k) | (P_x \pm iP_y) | u_n(k) \rangle$ is the interband (labeled by n and s) matrix element in the

momentum operator and $|u_s(k)\rangle$ and $|u_n(k)\rangle$ are the Bloch wavefunctions (*43*). The magnetic moment is determined by $\mathbf{m_s}(k) = \hat{\mathbf{z}}\frac{\mu_B}{2m_e}\sum_{n\neq s}\frac{|P_+^{ns}(k)|^2-|P_-^{ns}(k)|^2}{\varepsilon_n(k)-\varepsilon_s(k)}$, where μ_B labels the Bohr magneton, m_e labels the free electron mass, $\varepsilon_n(k)$ labels the energy dispersion of the nth band, and $\hat{\mathbf{z}}$ labels the out-of-plane direction. We can see that the χ directly reflects the sign and amplitude of $\mathbf{m}$. The calculated $\chi(\pm K) = \pm 1$ for the band edges of the two valleys in monolayer TMDs, which means that the electrons at K(-K) valley will only be excited by σ^+ (σ^-) light. This indeed supports our previous analysis. The calculated |η| from PL measurements is obviously a lower bound of $|\chi|$ at certain valley since the depolarized process plays a role during the relaxation and emission.

Experimentally, we can define the η as the degree of valley polarization, characterizing the population difference of the excited carriers between K and –K valleys. This value varies from device to device, depending on the sample quality, temperature, and other effects. In exfoliated monolayer MoS_2 samples, the valley polarization can be as high as 80 % at 30 K in our best samples. Interestingly, we find that our physical vapor grown MoS_2 monolayer (*47*) (See chapter 5) yields almost 100% valley polarization (η) at 30 K (Fig. 2.4a,b), and remarkably, even about 30% residual polarization at room temperature (Fig. 2.4c,d). This suggested that not only the circular dichroism is unity, but also the valley excited excitons experience almost no depolarization process before their emission. Such a high optical quality of as-grown TMD monolayers give rise to the possibility of investigating valley associated physics and devices at room temperature.

An interesting finding in such high optical quality MoS_2 is the observation of valley coherence (*34*) at low temperature. Not only memorizing the helicity of the circularly polarized excitation, we find that the PL emission in grown MoS_2 can also memorize the linear

polarization of the incident beam, as shown in Fig. 2.5a and b. If the monolayer is excited by a horizontally (H) polarized laser, the PL emission is also H polarized. So does the vertical (V) polarization. This co-polarization of linearly polarized light emission is very unusual, in a sense that linear polarization of light emission is generally determined by crystal axis or sample environment, such as the existence of a cavity. In our case, the polarized PL emission is a simply memory of the incident beam. An even higher degree of co-linearly polarized emission is observed in exfoliated monolayer WSe_2 samples (*34*) (Fig. 2.5c), suggesting the robustness of such phenomena in 2D TMDs.

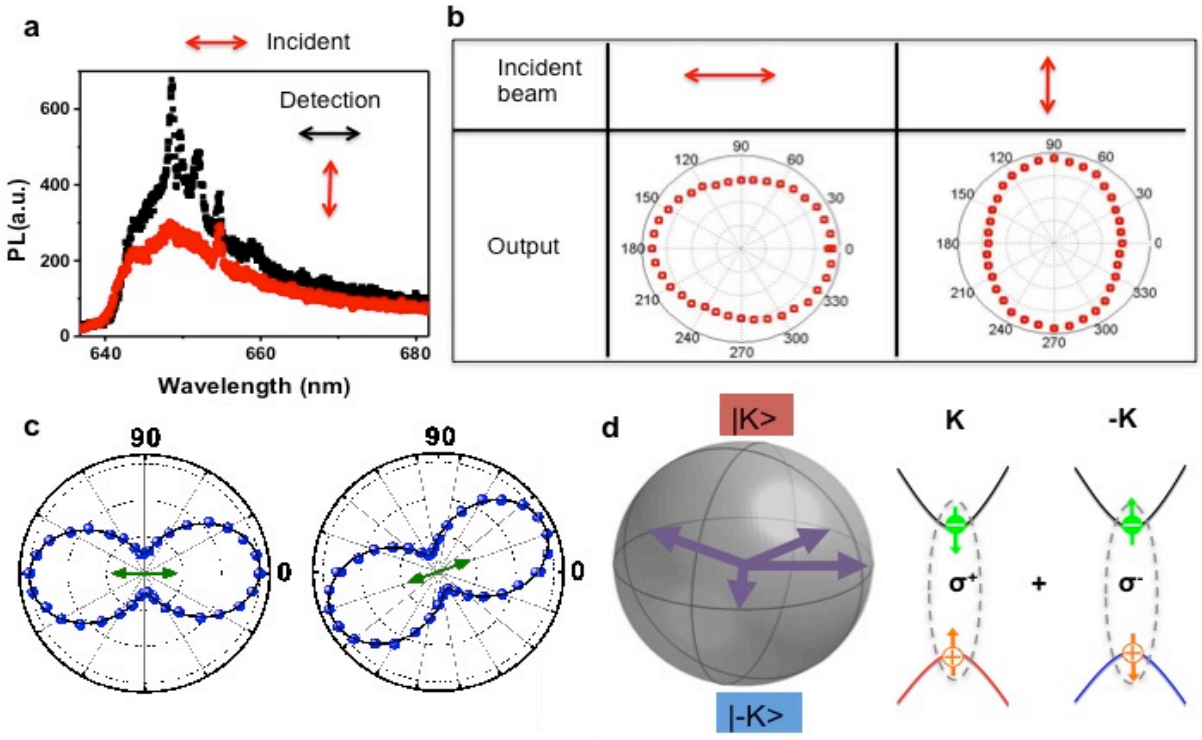

Figure 2.5. Valley coherence. a, Linear-polarization resolved PL spectra under H excitation of physical vapor grown MoS_2. b, Polar plot of PL intensity under both H and V incident beam. We can see that the PL is co-linearly polarized with the excitation laser. c, Similar polar plot of PL emission in WSe_2 exfoliated monolayer sample. The green arrows denote the incident polarization. d, Bloch sphere representations of valley polarized state |K>, |-K> on the north and south pole and the valley coherent state at the equators. The vectors pointing at equators

describes the superposition state of the two equal amplitude |K> and |-K> states with variant phase. The states at the poles are responsible for the circularly polarization and the states at the equators are responsible for the linear polarization.

This co-linear-polarization behavior can be excellently explained under the picture of valley contrasting physics (*34*). A linear polarized state of photons can be decomposed into the coherent superposition of two circularly polarized state, σ^+ and σ^-. When the light excites electrons in monolayer TMDs, both K and –K valley excitons will be created and the coherence information of the photons will be transferred into the coherence between the excited carriers, creating valley coherence. Due to the equivalence between the valleys, we expect that the quantum trajectories of the carriers in the two valleys undergo the same relaxation process to form excitons (involving Coulomb interaction and phonon scattering), assuming the lack of magnetic scattering. The quantum coherence thus can be store in the coherent valley excitons. This can be well depicted by the Bloch sphere (Fig. 2.5d). The radius vector pointing to the north and south poles corresponds to the perfectly valley polarized excitonic state |K> and |-K>. The states at the equators corresponds to the coherent superposition of equally populated valley state |K> + $e^{i\emptyset}$|-K>, where $\emptyset$ is the phase difference. Under the excitation of linearly polarized laser, a state at the equator is created, of which the phase reflects the polarization direction.

The valley coherence is preserved until the radiative emission of the excitons. The excitons are in a superposition of the two valley states, and consequently the photons emitted by these excitons will contain both σ^+ and σ^- with a relative phase $\emptyset$. As a result, the PL will also be linearly polarized, in the same manner as the incident beam. These observations also suggest that we can create and read out a valley coherent excitonic state at an arbitrary position of the equator on the Bloch sphere, using optical pumping. In the future, it will be interesting to see whether one can generate a state that is in between the equator and the poles, which is a coherent

superposition of unequally populated valley excitons. The existence of such a state is crucial to observe other essential quantum behaviors of valley excitons, such as valley Rabi oscillations, and to the possibility of developing valley-based quantum bit (*48*).

2.6 BILAYER TMDS AND SYMMETRY CONTROL

In the above sections we have established the valley contrasting physics emergent from the IS broken of the 2D hexagonal lattice. To further explore this principle and also to control the valley properties, we here study TDM bilayers (*43*). In contrast to the monolayer, the naturally formed bilayer samples (often called 2H TMD, AB stacked) contain a spatial inversion center, located in between the two layers, as shown in Figure 2.6. According symmetry principles, the two valleys at K and –K momentum become indistinguishable and thus the valley associated quantities such as valley magnetic moment and Berry curvature, becomes identical. However, if one applies an out-of-plane electric field, IS breaks and subsequently the valley physics emerges.

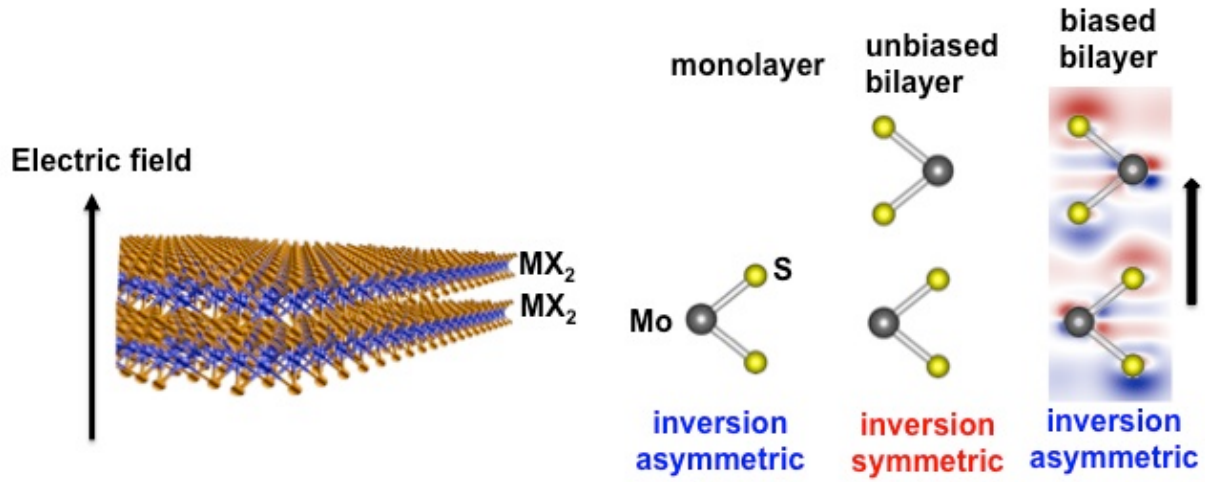

Figure 2.6. Symmetry control in bilayer TMDs. Left, cartoon depiction of bilayer TMDs under electric field. Right, side view of crystal structures of monolayer, unbiased bilayer and biased bilayer. The inversion center of the pristine bilayer is at the center of the two layers. In the biased case, electric field leads to potential difference in different layer. The color map indicates the

change of electron density under the effect of electric field, showing the absence of the inversion center.

Here we employ tight-binding model to estimate how the valley magnetic moment and Berry curvature can be affected by a perpendicular electric field, using 2H bilayer MoS2 as an example. The low-energy effective Hamiltonian of the bilayer can be constructed from its single layer from, which has already been derived in Ref. (*49*). The bilayer tight binding Hamiltonian in the vicinity of K and –K valleys is written as:

$$H_0(\mathbf{k}) = \begin{bmatrix} \Delta & as(\tau k_x + ik_y) & 0 & 0 \\ as(\tau k_x - ik_y) & -\Delta & 0 & r \\ 0 & 0 & \Delta & as(\tau k_x - ik_y) \\ 0 & r & as(\tau k_x + ik_y) & -\Delta \end{bmatrix}$$

where $\Delta = 0.83$ eV is the half value of the band gap of MoS2 monolayer, $a = 3.193\,\text{Å}$ is the hexagonal lattice constant, $s = 1.10$ eV describes the effective intralayer hopping, $r = 0.047$ eV describes the effective interlayer hopping, and $\tau = \pm 1$ labels the valley index. One can see that the diagonal blocks mimic the Hamiltonian of graphene with a bandgap. This captures the essence of valley physics in the single layer form. The off-diagonal block reflects the inter-layer coupling, which should obey the D_{3d} symmetry of the bilayer sample. The four basis of $H_0(\mathbf{k})$ can be expanded:

$$\left|\psi_1\right\rangle = \left|d^{\mathrm{t}}_{z^2}\right\rangle, \quad \left|\psi_2^{\tau}\right\rangle = \frac{1}{\sqrt{2}}(-i\tau\left|d^{\mathrm{t}}_{xy}\right\rangle + \left|d^{\mathrm{t}}_{x^2-y^2}\right\rangle), \quad \left|\psi_3\right\rangle = \left|d^{\mathrm{b}}_{z^2}\right\rangle, \quad \left|\psi_4^{\tau}\right\rangle = \frac{1}{\sqrt{2}}(i\tau\left|d^{\mathrm{b}}_{xy}\right\rangle + \left|d^{\mathrm{b}}_{x^2-y^2}\right\rangle).$$

Here the superscript t and b labels respectively the “top” and “bottom” layers.

To consider the effect of out-of-plane electric field, we introduce a potential difference between the top and bottom layer, 2V. Consequently, we can write the electric-biased Hamiltonian as:

$$H(\mathbf{k}) = \begin{bmatrix} \Delta + V & as(\tau k_x + ik_y) & 0 & 0 \\ as(\tau k_x - ik_y) & -\Delta + V & 0 & r \\ 0 & 0 & \Delta - V & as(\tau k_x - ik_y) \\ 0 & r & as(\tau k_x + ik_y) & -\Delta - V \end{bmatrix}.$$

We can then compute the momentum-resolved orbital magnetic moment $\mathbf{M}_n(\mathbf{k})$ and Berry curvature $\Omega_n(\mathbf{k})$, which are defined respectively as:

$$\mathbf{M}_n(\mathbf{k}) = -i\frac{e}{\mathrm{h}}\langle \nabla_{\mathbf{k}} u_n | \times (H - \varepsilon_n) | \nabla_{\mathbf{k}} u_n \rangle$$

$$\Omega_n(\mathbf{k}) = i\langle \nabla_{\mathbf{k}} u_n | \times | \nabla_{\mathbf{k}} u_n \rangle .$$

Here u_n describes the periodic part of Bloch wavefunction and ε_n is energy dispersion of the n -th band. Experimentally the valley excitons only form at the lowest energy in the vicinity of the K and -K points. For the top most valance band at the K and –K points, under the condition, $\mathrm{r}, \mathrm{V} \ll \Delta$, we then obtain (only z components, due to 2D nature)

$$m = \frac{\tau e a^2 s^2}{2\hbar\Delta}\frac{V}{\sqrt{r^2 + V^2}}.$$

$$\Omega = -\frac{\tau a^2 s^2}{2\Delta^2}\frac{V}{\sqrt{r^2 + V^2}} = -\frac{\hbar}{\Delta e}\mathrm{m}$$

These equations clearly tell us the relation between the valley magnetic moment and the Berry curvature. We can find that both quantities can be continuously tuned by the electric potential V. If $V = 0$, then both $\mathrm{m}, \Omega = 0$, corresponding to the pristine bilayer. If V changes sign, then m and Ω change their polarity. We therefore can tune the valley-associated properties by electrical means.

2.7 ELECTRICAL TUNING OF VALLEY MAGNETIC MOMENT

In this section, we will discuss the experimental demonstration of electrical tuning of valley-associated Berry phase properties in bilayer MoS_2 (*50*). We performed polarization resolved PL measurements on bilayer samples that were fabricated in a FET architecture. An out-of-plane electric field can be induced by applying back gate voltage. The bilayer samples were cooled down to 30K. The primary results are summarized here in Fig. 2.7.

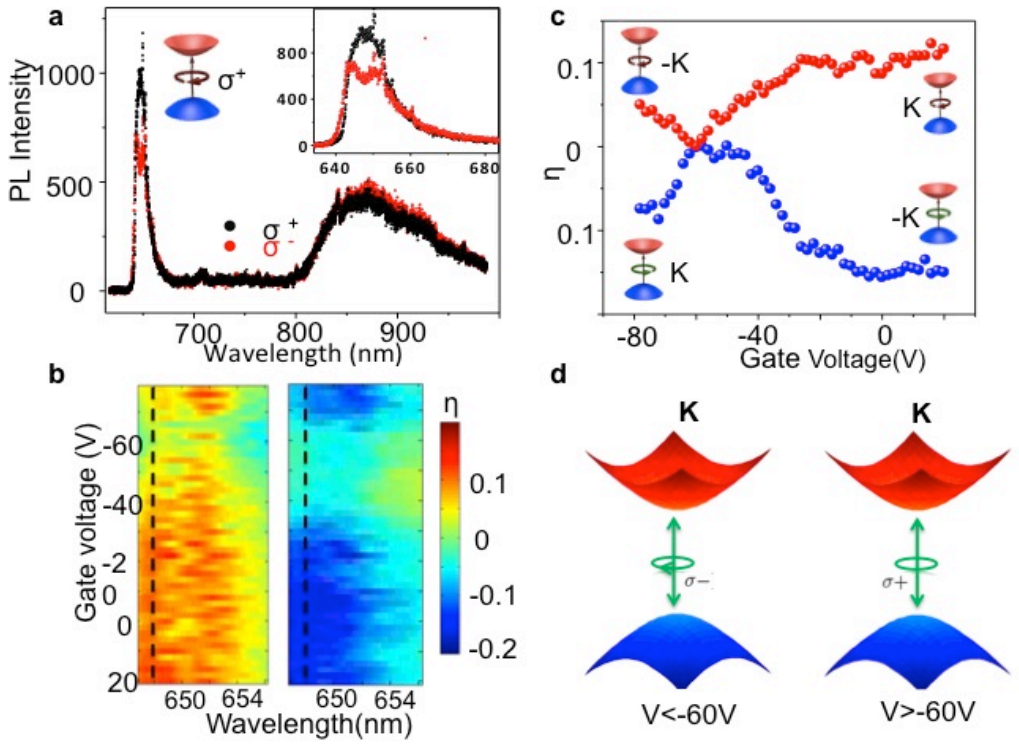

Figure 2.7. Electrical tuning of valley associated Berry phase properties in bilayer MoS_2. a, Polarization resolved PL spectra of the bilayer, showing a non-zero valley polarization. This indicates that there are residual electrostatic potential built in the device. b, The degree of circular polarization as a function of gate voltage and the wavelength. Left panel: σ^+ excitation. Right panel: σ^- excitation. c, Gate dependent circular polarization. The plots correspond to the line cuts indicated by the black dashed lines in b. d, Cartoon depicts optical selection rule of the same valley under different gate voltages. The optical dichroism is completely changed by gate.

The polarization resolved PL spectra taken at zero gate voltage under σ^+ light excitation are shown in Fig. 2.7a. The bilayer sample, due to the indirect band gap emission, has a relatively weak PL emission compared to the monolayer sample, where a direct bandgap forms. However, the emission from the two valleys can still be observed at around 650 nm. Here we can already see the polarized emission for the valley excitons, which contrasts with the theoretical understanding of pristine bilayer. This is due to the residual electrostatic potential in the fabricated devices, leading to nonzero electric field under zero gate voltage. The broad peak at ~ 850 nm corresponds to the impurity bands, which is reasonably unpolarized. Fig. 2.7b plots the degree of circular polarization, η, for both σ^+ and σ^- excitation as a function of gate voltage near the valley exciton wavelength. We can see that the color map is non-uniform, and the amplitude of η becomes minimum at gate voltage about -60 V. Line cuts along the dashed black lines, corresponding to wavelength ~ 647 nm are shown in Fig. 2.7c, which shows the minimum η approaches zero for both excitations at the same gate and can be continuously tuned up to 15% in both negative and positive direction. This striking feature can be described as an "X" pattern of the η.

This "X" pattern behavior of bilayers is very different from the monolayer sample. In monolayers, IS is broken structurally and the electric field should have no effect on the valley magnetic moment. Consequently, the plot of η will yield a uniform map, where no gate dependence can be observed. This is indeed the case, as shown in Ref. (*49*).

Intriguingly, one can explain such "X" pattern very well by considering the electric field effect on the valley magnetic moment. According to the previous section, valley carriers in bilayer MoS_2 will acquire finite valley magnetic moment under nonzero field, whose direction

determines the polarity of the moment. In this device, $\eta = 0$ at gate voltage $V_g \sim$ -60 V, suggesting that the residual electrostatic potential between the two atomic layers from device fabrication process are compensated at this gate. At $V_g >$ -60 V, a net positive field is develop, and consequently the valley carriers develop optical dichroism, i.e., carriers at K (-K) valley will only be excited by σ^+ (σ^-) light. While at $V_g <$ -60 V, net negative field will leads to a opposite valley selection rule (Fig. 2.7d). This then naturally explains the "X" pattern of bilayer.

To summarize, this experiment demonstrates that the IS breaking is indeed essential to the emergent Berry phase related properties associated with valleys. We have also provided a way to continuously tune the valley properties by electrical means.

2.8 ANALOG BETWEEN VALLEY PSEUDO-SPIN AND REAL SPIN

In previous sections, we have established that the discrete two-value index "valley" associated with Bloch electrons in 2D TMDs is a measurable and controllable degree of freedom. To better characterize this new, external degree of freedom, we here summarize the valley-associated effects that have been reported, in comparison with the real spin index (Table 2.1).

We have demonstrated that valley index exhibit the effects of magnetic moment, optical selection rules, polarization and coherence, which are very similar to the effects associated with spin. Recent experimental observations have also demonstrated the valley Hall effect (*51*) and valley Zeeman effect (*52–54*), analog to the spin Hall effect and spin Zeeman effect. Consequently, we can summarize that the valley index behaves as a pseudo-spin, which should be considered very closely related to the real spin. Future development may utilize this valley pseudospin, just like the way we use the real spin, for example, to construct valley-based logic operations and quantum control.

Table 2.1. Comparison between spin and valley indices of Bloch electrons.

Phenomena\index	Spin	Valley
Magnetic moment	✓	✓
Optical selection rule	✓	✓
Polarization	✓	✓
Coherence	✓	✓
Hall effect	✓	✓
Zeeman effect	✓	✓
Rabi Oscillation	✓	✗

We would also like to point to out that, despite the above, there is still dissimilarity between valley pseudo-spin and real spin. One particular difference is that we still don't know how to observe Rabi oscillation, or similar phenomena, for valley. In spin system, Rabi oscillation is one of the hallmark phenomena in the quantum control of a two-level system (e.g. spin ½ system). It corresponds to a cycling of the vector state at the surface of the Bloch sphere. Previously we have shown that one can describe the valley states (polarized states and coherent states) on a Bloch sphere (*34*). Yet it is still not clear how one can kick the valley vector to move on the sphere. There is great interest in achieving such behavior, which would initiate a new region of quantum control purely based on valley pseudospin.

2.9 RECENT DEVELOPMENTS AND FUTURE OUTLOOK

In this chapter, we have mainly focused on the excitonic and valley-associated properties of monolayer and bilayer semiconductors. The field is developing quickly and many new observations and new systems emerge frequently. For example, while the measurement that we mostly discussed is PL, which only uncovers the steady state information, the dynamics of the excitons and valley information are also animportant and interesting subjects. A number of reports have thus far been focused on ultrafast measurements (e,g, (*55*)). In this section, instead of reviewing different kinds of measurements, we selectively list some general topics that are naturally extended from our previous discussions, for both 2D exciton physics and valley physics.

(1) Electrically pumped light emission.

Instead of optical pumping (PL), one can also inject carriers (both electrons and holes) easily into the monolayer TMDs, forming electrically pumped excitons and generating electroluminescence (EL) (*18*, *21–23*). There are several different geometries reported for this purpose, including both lateral p-n junctions and also vertical van der Waals junctions (*56*). These devices are prototypes of 2D-crystal based light emitting diodes (LEDs), which promise novel applications in lighting and information processing technologies.

(2) Single photon emission.

When the monolayers are cooled down to liquid helium temperature (~ 5 K), the excitons that are bound to defects emit quantum light, in which photon statistics exhibits antibunching behavior (*57–60*). The defects in monolayer semiconductors thus become a

single photon source, which has several advantages over conventional sources. To date, both optically pumped and electrically pumped (*61*) single photon emission from monolayer TMDs have been reported.

(3) Interlayer excitons.

In addition to the intralayer excitons in a single monolayer, one can also construct a heterobilayer system to search for interlayer excitons, in which electrons and holes exist in different layers (*62*). These has been successfully achieved by, for example, in a $MoSe_2$ / WSe_2 bilayer. The type-II band alignment of the two layers intriguingly allows for such separation and efficiently generates interlayer excitons in a relatively long wavelength. Compared to the intralayer excitons, these interlayer excitons have significantly improved life times and also preserve their valley information up to orders of magnitude longer time (*63*).

(4) Topological valley transport.

In addition to the optical selection rules, the Berry-phase-related physics associated with the valley index also induces very interesting phenomena in electron transport behavior. Due to the opposite Berry curvature in different valleys, the trajectories of the valley carriers exhibit Hall-like behavior without external magnetic field, leading to topological valley transport. Related observations have been made in monolayer TMDs with optical excitations (*51*), gapped single layer graphene (*44*), electrically biased bilayer graphene (*46*) and bilayer graphene domain walls (*64*). These observations, together with the optical measurements discussed previously, provide a consistent and mature understanding of the valley physics.

(5) Spin-valley locking effect in superconductivity.

The valley physics in 2H-TMD monolayers are important not only in the semiconducting phases but also in the superconducting region. In both ion-gel gating induced superconductivity in MoS_2 samples (*65*, *66*) and the intrinsic superconductivity in mono- and bi-layer $NbSe_2$ samples (*67*), it has been reported that the valleys, which are locked to the electron spins, can protect the superconductivity from very strong magnetic field. This effect leads to the novel Ising-pair superconductivity. In the future, observations originating from the valley index in the non-semiconducting region could be interesting.

Chapter 3. 2D NANOPHOTONICS: THE DEVICE FOR LASING

In addition to the valleytronics and LEDs, the device applications of TMD monolayers have also been explored in many other fields, such as solar cells, photo-detectors, transistors and so on. One reason of such wide interest can be attributed to the unique properties of these monolayers. We thus summarize some of their physical and chemical properties in Table 3.1. Some of these properties have been discussed in previous chapters, such as visible direct bandgap at BZ corners, sub-nanometer thickness, large exciton binding energies, and easy injection of carriers, etc. In addition, the four kinds of monolayer semiconductors, i.e., MoS_2, WS_2, $MoSe_2$, and WSe_2, are stable and flexible, and maintain their quality even exposed to ambient environment. Despite their atomic thickness, they can absorb as strongly as ~10% of incident light. Due to recent development of both wet and dry transfer techniques for 2D crystals, they can be easily integrated with many kinds of structures and surfaces. These superior properties of TMDs allow us to explore novel applications of 2D crystals. In this chapter, we will study the interface effects of monolayer semiconductors on a photonic crystal cavity (PhCC), with a hope to expand the potential of 2D materials in nano-photonics.

Table 3.1. Properties and potential applications of TMD monolayers.

Properties	Advantages	Applications
➢ Direct gap Semiconductor ➢ Atomically thin crystal ➢ Unique electronic behavior ➢ Structurally Stable ➢ Flexible and strong ➢ Electrically tunable ➢ Optically active	➢ Visible gap ➢ Direct electrostatic doping ➢ Flexible and transparent devices ➢ Simple transfer techniques ➢ Large area synthesis ➢ Large exciton binding energies ➢ Strong light absorption	➢ Valleytronics ➢ Transistors ➢ LEDs ➢ Solar Cells ➢ Photo-detectors ➢ Sensors ➢ Nonlinear optics ➢ Nano-lasers ➢ 2D circuits

3.1 THE NEED FOR NANOSCALE PHOTONICS

Electrons and photons are two fundamental energy and information carriers. Owing to the successful miniaturization of the electronic devices, electronics have been developed into large-scale applications for information processing. However, the development of photonics falls far behind. Constructing small-scale (nanometer, or micrometer) photonic devices, which could eventually lead to the miniaturization of photonics, is a long-term goal to meet the need of on-chip optical communication and computation. A miniaturized photonic device should satisfy several requirements including scalability, low power consumption and ultrafast switch.

One essential component that needs to be miniaturized is the laser system. When the laser was invented in the 1960s, it was regarded as "a solution looking for problems". Laser systems are now widely applied in many fields, ranging from physical science, communications, medicine and biology, to manufacturing, defense, and entertainment. Today the situation is of course very different. There are many problems looking for solutions that can be provided by practical nanoscale laser systems. A wide range of relevant fields includes optical computation, biosensing, nanoscale spectroscopy, and the construction of "small machines".

In this chapter, we will introduce a new strategy based on 2D crystals for building nanoscale photonics systems, such as nanolasers (*68*, *69*). Before we go into the details of our system, here we outline a definition of a nanolaser first. A nanolaser should contain three key ingredients: (1) The photons are confined in a nanoscale cavity, whose dimensions are several hundreds of nanometers or less; (2) the underlying mechanism of the lasing, i.e., the photon-emitter interaction, is described by cavity quantum electrodynamics. This is the essential difference between a nanolaser and a traditional laser; (3) the entire system can be integrated into a chip-scale package.

3.2 PHOTONIC CRYSTAL CAVITY

To explore the potential of monolayer semiconductors in nanophotonics, we study the coupling between the materials with a nanoscale optical cavity, namely a photonic crystal cavity (PhCC) (*70*). A PhCC is "defect" defined in a photonic crystal (PhC), which consists of periodic structure of dielectric materials. For example, a 2D photonic crystal can be constructed by inducing an array of empty holes with a size of around hundreds of nanometer in a suspended semiconducting membrane (see Fig. 3.1a) (*71*). Through introducing the missing-hole structure, i.e., the defect, an optical cavity can form and photons with matched energy (resonant mode, Fig. 3.1b) will be confined in the defect region (*70*). This photon confinement can be understood by the satisfaction of total internal reflection of the light in all the in-plane directions in the structure, leading to a small spatial volume of the confined photons. Another way to understand such structure is by adapting the idea from atomic crystals. Photons traveling in a PhC are similar to electrons traveling in an atomic crystal, where energy bands and gaps are developed (*70*). A well-designed PhC will create a photonic band gap with a finite size (Fig. 3.1c). Photons with energy in the bandgap will not be able to travel in the structure, much like electrons don't travel in an insulator. Consequently, photons with energy matched with a cavity resonance in the gap will be strongly confined in the cavity region. Fig. 3.1b shows the in-plane electric field profile of a fundamental mode in an L3-type (3 missing holes in the defect) PhCC made with gallium phosphide (GaP) membrane (*71*).

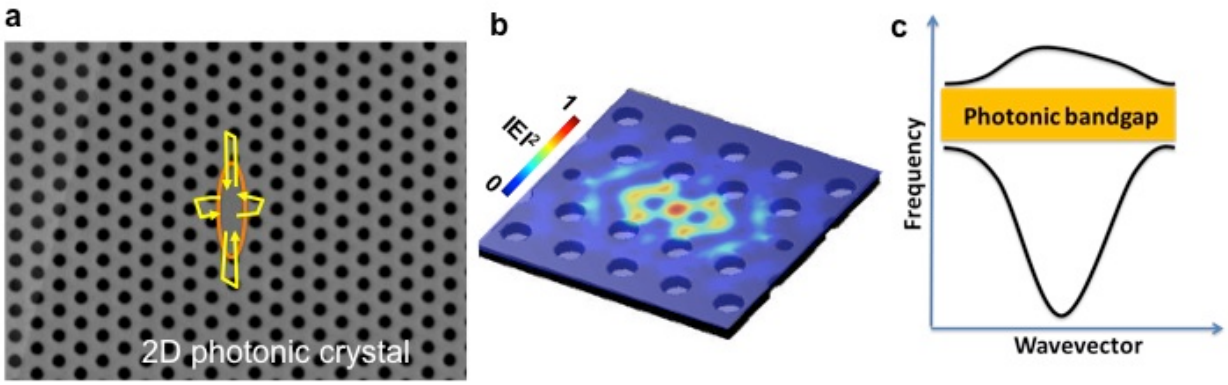

Figure 3.1. 2D photonic crystal cavity. a, SEM image of a PhCC made with a GaP membrane. It shows its structure consisting of an array of empty holes. The cavity is defined by missing holes (L3 type cavity), where the light is confined. b, the normalized electric field intensity profile of the fundamental mode in the cavity, simulated by FDTD method. c, Similar to the crystalline structure made with atoms for electronic states, this periodic optical structure gives rise to bands and bandgaps for photons, scratched in c.

3.3 PURCELL EFFECT AND CAVITY QED

When a light emitter is brought close enough to such an optical cavity, interesting phenomena arise in the concept of light-matter interaction. In a typical situation, such as a light bulb, photons coming from spontaneous emissions will escape from the emitter uncontrollably into free space. However, this is no longer true when an optical nanocavity is presented, which can reflect the emitted photons back to the emitter within a time comparable to one photon cycle. In this region, light-matter interaction needs to be formulated by the cavity quantum electrodynamics (QED). There are generally two regions of cavity QED, capturing weak and strong light-emitter coupling.

In the weak coupling region, one direct consequence is that the spontaneous emission rate of the emitter is altered (*72*). This so-called Purcell effect exists in a sense that the local density of optical states of the transitions is altered by the presence of a cavity, in comparison with the

free space density of states. This effect can lead to a significantly enhanced spontaneous emission rate in resonance with the cavity, benefiting or initiating a number of photonic devices, such as single photon source (*73*), quantum processing (*74*) and nanolasers (*75*, *76*).

Such enhancement can be characterized by Purcell factor. In an optical nanocavity, the maximum achievable Purcell factor, i.e., the peak enhancement of the emission rate can be calculated by (*70*):

$$F_{max} = \frac{3}{4\pi^2}\frac{Q}{V}\left(\frac{\lambda_c}{n}\right)^3 .$$

Here, F_{max} labels the maximum Purcell factor, Q describes the cavity quality factor, V is the mode volume, which is $\sim(\frac{\lambda_c}{n})^3$ for PhCC, n is the refractive index of the dielectric material (n ~3.1 for GaP in our case) and λ_c is the cavity emission wavelength. If one fabricate a PhCC resonating at λ_c ~740 nm with Q ~ 8000, we then obtain $F_{max} \sim 607$. The realistic Purcell factor in a functioning device, of course, is less than this optimal value, which will be further discussed later.

In the strong coupling region, photons and the emitting particles are tightly bounded, and each individually can't be treated as a good quantum number to describe the system. New quasi-particles, namely polaritons, which describe a type of photon-exciton composite particles, need to be introduced to characterize the system (*39*, *77*). The observation of both regions in PhCC system has been made through coupling the cavity with quantum wells or quantum dots (*78*). The strong coupling region (polariton state) for 2D semiconductors has also been reported recently using a cavity made with distributed Bragg reflectors (DBR) (*79*, *80*). In this chapter we will mainly focused on the weak coupling region (Purcell region) in 2D semiconductor / PhCC system.

3.4 CONVENTIONAL SYSTEMS *V.S.* 2D CRYSTAL BASED SYSTEMS

Conventionally emitters, such as quantum wells or quantum dots need to be embedded into the cavity, during the cavity's fabrication process, in order to be efficiently coupled (*75*, *81–83*). During the past few decades, the quantum well and quantum dot embedded nanocavity systems have triggered enormous investigation in this field. The fruitful achievements include the control of the spontaneous emission of the emitters (*72*), the demonstration of both pulsed (*81*) and continuous wave (CW) nanolasers (*75*) and the construction of efficient single photon sources (*73*). However, these conventional designs suffer potential difficulties in terms of practicality and compatibility with existing electronic circuits: (1) Electrical pumping is generally difficult since it is challenging to fabricate electrodes contacting to the light-active material to form electronic elements like transistors (*76*); (2) in quantum well systems, light extraction efficiency is limited due to the finite light cone (from which light can escape the total internal reflection at the air-semiconductor surface) (*81*); (3) during fabrication process, a considerable amount (~30%) of the embedded quantum well needs to be etched away, which leads to the degradation of the quantum well's optical properties and reduces the device performance (*81*); (4) in the quantum dot systems, challenges such as the random positions and compositional fluctuations of the dots prevent their realistic applications (*84*).

We propose a new strategy to achieve emitter-cavity coupling using monolayer semiconductors (*85*, *86*). We demonstrate that the extreme thickness (sub-nanometer) of the monolayer allows us to achieve efficient coupling by directly placing the monolayer on top of a PhCC (Fig. 3.2). Numerical simulations suggests that the surface monolayer still experiences ~ 40% of the maximum field strength at the very center of the cavity (characterized by $|E|^2$ as shown in Fig.3.2c), ensuring a good coupling between monolayer excitons and the cavity field.

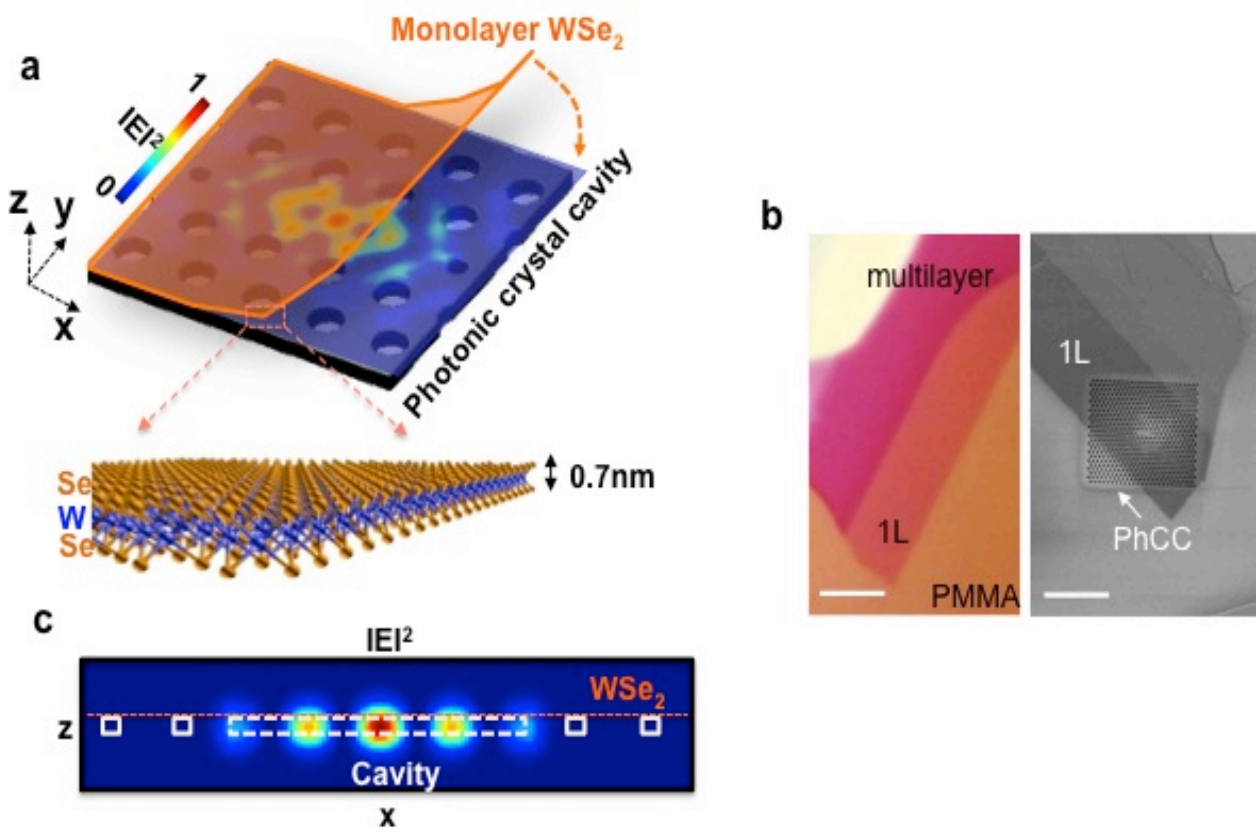

Figure 3.2. A typical 2D-crystal / PhCC coupled system. a, Cartoon depicting the surface-gain system. The monolayer is mechanically transferred onto the cavity with deterministic positions after the fabrication process of both the emitter and the cavity. The monolayer emitter and the cavity are thus combined nondestructively and maintain their high quality. b, the optical microscope image (left) of the monolayer WSe_2 (labeled by "1L") on PMMA substrate and the SEM image (right) of the cavity-WSe2 hybrid. Scale bars: 3 μm. c, The cross section of the electric field profile of the fundamental mode defined by the cavity. The white rectangular denotes of the position of empty holes in the PhC. The monolayer, which is about 0.7 nm, is sitting right on top of the cavity, still experiencing about 40% of the maximum field at the very center of the cavity.

Below we summarize the advantages of such systems.

(1) This surface geometry removes the requirement of “embedding”, and thus separates the fabrication procedures of cavity and the emitter. The monolayer is deposited to the cavity surface at the very end. Moreover, it allows for further fabrications of transparent top gates (such as graphene) to the monolayer, which may offer the opportunity for the integration to CMOS technologies. This approach hence provides compatibility with integrated electronic circuits.

(2) The transfer process of the monolayer is nondestructive and deterministic. Both the cavity and the emitter maintain their high quality during the whole fabrication process, in contrast to the conventional systems.

(3) It allows a much simpler way for achieving electrical injection of carriers than in conventional systems. Ion implantation, which is used to define p-n junction and electrically inject carriers in QD/PhCC lasers, leads to degradation of QD and limits their operation to low temperatures. In contrast, p-n junctions of 2D materials can be built easily either laterally or vertically.

(4) The gain medium, i.e., the monolayer semiconductor, can be obtained with very high quality by either mechanical exfoliation or CVD/PVD growth. The on-demand nano-fabrication and material growth don’t require MBE process. In principle, this approach also allows for the replacement of gain media in a laser after degradation – something that is challenging when employing QDs or QWs as gain material. This could be of importance in. e.g., systems integrated on a microprocessor chip.

3.5 CONTROL OF SPONTANEOUS EMISSION IN MONOLAYER SEMICONDUCTORS

The first device that we will describe is a monolayer WSe_2 coupled with a GaP 2D PhCC (L4 type). Monolayer WSe_2 has a relatively high PL quantum yield compared to other 2D semiconductors and it excitonic emission (free excitons) is located at ~750 nm at room temperature and blue shifts to ~ 720 nm at low temperatures. These emission energies match well with the GaP PhCC, which is typically used to fabricate cavities resonant at visible wavelengths. As shown in Fig.3.3a, we present our fabricated WSe_2/PhCC device with the cavity Q factor ~ 250 at resonance ~ 756 nm. The emission spectra taken at three different regions (on cavity, red; on PhC, black; and off PhC, green) are respectively plotted in Fig.3.3b. Two features can be summarized here. (1) The PL emission is greatly enhanced on PhC (black line) compared to off PhC (green line). The total integrated PL intensity is ~ 20 times larger when the WSe_2 is sitting on top of the PhC (Fig.3.3c). (2) There is a narrow emission peak parked at ~ 756 nm on top of the broad PL emission when the cavity region is under examination.

The first aspect indicates that PhC possibly enhances the radiative recombination of excitons in WSe_2. On one hand, we know that the PL quantum yield of a TMD monolayer is sensitive to the substrate and the surrounding environment (*12*). The light extraction efficiency also depends on the substrate. One the other, the photonic band-gap effect of the PhC could inhibit the spontaneous emission at lateral directions (*87*) and redistribute the emission into the vertical direction. Both effects may contribute to the PL enhancement on PhC in this device.

The second aspect demonstrates that the emitter-cavity coupling is indeed effective in such 2D crystal based surface geometry. The narrow peak emission is identified as originated from the cavity mode and is polarized along the x direction. Fig.3.3d shows the spatial map of the peak emission, which links the emission to the cavity region unambiguously. The mechanism

of this peak can be attributed to the Purcell effect, which describes the enhanced spontaneous emission rate of the monolayers in resonance with the cavity mode (*85*, *86*).

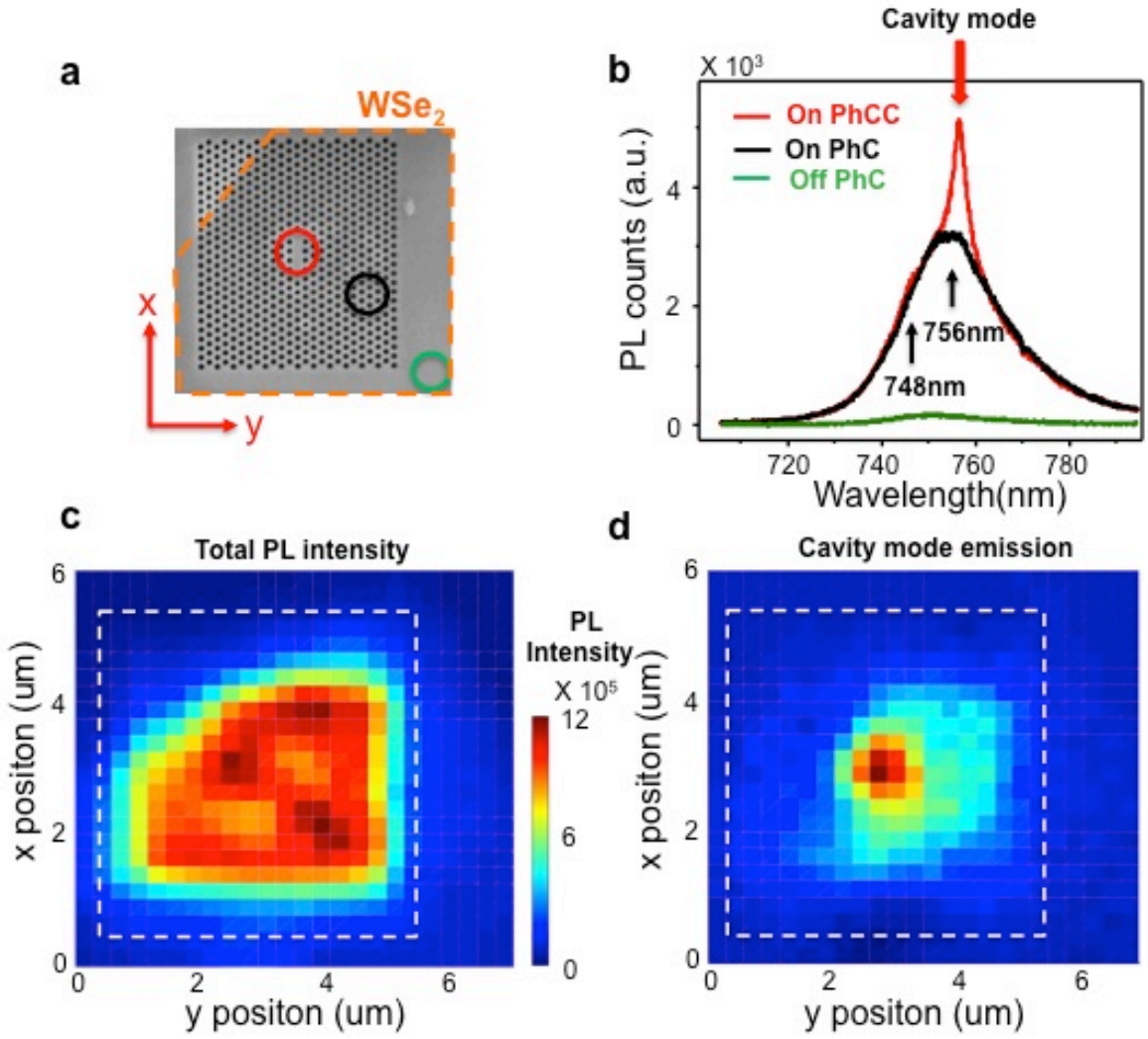

Figure 3.3. Emission properties of a WSe_2/PhCC hybrid system with a low Q factor cavity. a, SEM image of the device, where the orange dashed line outline the WSe_2 region. b, PL spectra taken from different spots (red, on PhCC; black, on PhC; and green, off PhC). c, Total PL intensity map of the device, showing the strong enhancement of the detected emission by PhC. the white dashed line indicated the PhC. d, the spatial map of the height of the 756 nm emission peak, locating the peak to the cavity region.

To better under the Purcell effect in our monolayer coupled cavity system, we here estimate the Purcell factor taking account multiple realistic factors (*24*). Previously, we have provided a formula for estimating the maximum achievable Purcell factor F_{max} for a PhCC. In our device, there are several factors reducing this value. First, the spatial displacement in z direction shifts the emitter from the optimal position. Second, it is known that the random dipole directions of excitons could reduce the Purcell factor. Considering these two effects, the Purcell factor should be:

$$F = F_{max}|\psi(s)|^2 < \cos^2\xi >,$$

where $|\psi(s)|^2 = |\frac{E(s)}{E_{max}}|^2 \sim 0.4$ describes the effect of spatial detuning, which is the field intensity ratio between the surface and the very central. ξ describes the angle between exciton dipole direction, which is random in x-y plane, and the polarization direction of the electric field. $< \cos^2\xi > = \frac{1}{2\pi}\int_0^{2\pi} \cos^2\xi \, d\xi = \frac{1}{2}$. A relatively realistic estimation of the Purcell factor will then be F ~ 3.8 for Q = 250 and $\lambda_c \sim 756\, nm$, where the excitons are on the cavity resonance and located right above the center of the cavity.

In real situations, other effects could further reduce this value. For instance, transferring a monolayer on top of the cavity may reduce the Q factor. The spatial displacement of excitons in lateral directions is neglected in the above considerations, but may also play a role; the spectral fluctuations of the emission linewidth might lead to time-dependent variations in the Purcell factor. However, the observed cavity mode in the PL emission clearly reveals the effectiveness of this geometry and the Purcell effect is indeed important in controlling the spontaneous emission rate of the monolayer semiconductors.

3.6 CONTROL OF SPATIAL DISTRIBUTION OF MONOLAYER LIGHT EMISSION

In this section, we will discuss the control of far-field emission pattern of the 2D excitons enabled by the PhC, which employs its diffraction grating effect. We will return to the cavity's effect in the next section. To observe the far-field emission patter, we perform momentum-resolved microcopy, which images the back focal plane of the objective lens in front of the emitter. The momentum distribution of the PL emissions can then be mapped out by a CCD camera. The details of the measurements can be found in Ref. (*85*).

We inspected the emission from monolayer WSe_2 on top of variant substrates, including SiO_2, off-PhC region on the GaP membrane, and on PhC (Fig. 3.4a, b and c). For the SiO_2 and off-PhC GaP region, the light emission patterns show similar behavior with a maximum intensity at the center, although on SiO_2 the PL is more vertically directed. However, the pattern obviously changes when the monolayer is placed on a PhC, where the PL is highly directed in a region that is defined by a ring outlined by the dashed lines (corresponding to polar angles, i.e., the angle between the emitting direction and the vertical direction, $34^o < \theta < 48^o$). This reveals that the in-plane momenta of the emitted photons from the on-PhC region are strongly localized between $0.55k_0$ and $0.75k_0$, where $k_0 = 2\pi/\lambda$ is the amplitude of the photon's wave vector at wavelength λ.

Fig.3.3d plots from the different emission profiles along a fixed line ($k_x = 0$) versus polar angle θ for on and off PhC region. We also include a Lambertian emission (green line) for comparison. One can see that the light emission from planar substrates, such as SiO_2 and the GaP membrane, tends to have Lambertian-like emission. However, the PhC direct the emission significantly different from the Lambertian behavior. Instead, the emission is selectively directed to certain polar angles. In Fig. 3.3e, we plot the emission pattern from another device, where the

PhCC lattice constant is increased to 375nm, rather than the 200 nm of the aforementioned device. In this device, the emission is directed not only to certain polar angles, but also to the azimuthal angles. Due to this azimuthal non-uniformity, the emission now shows separated islands in the map.

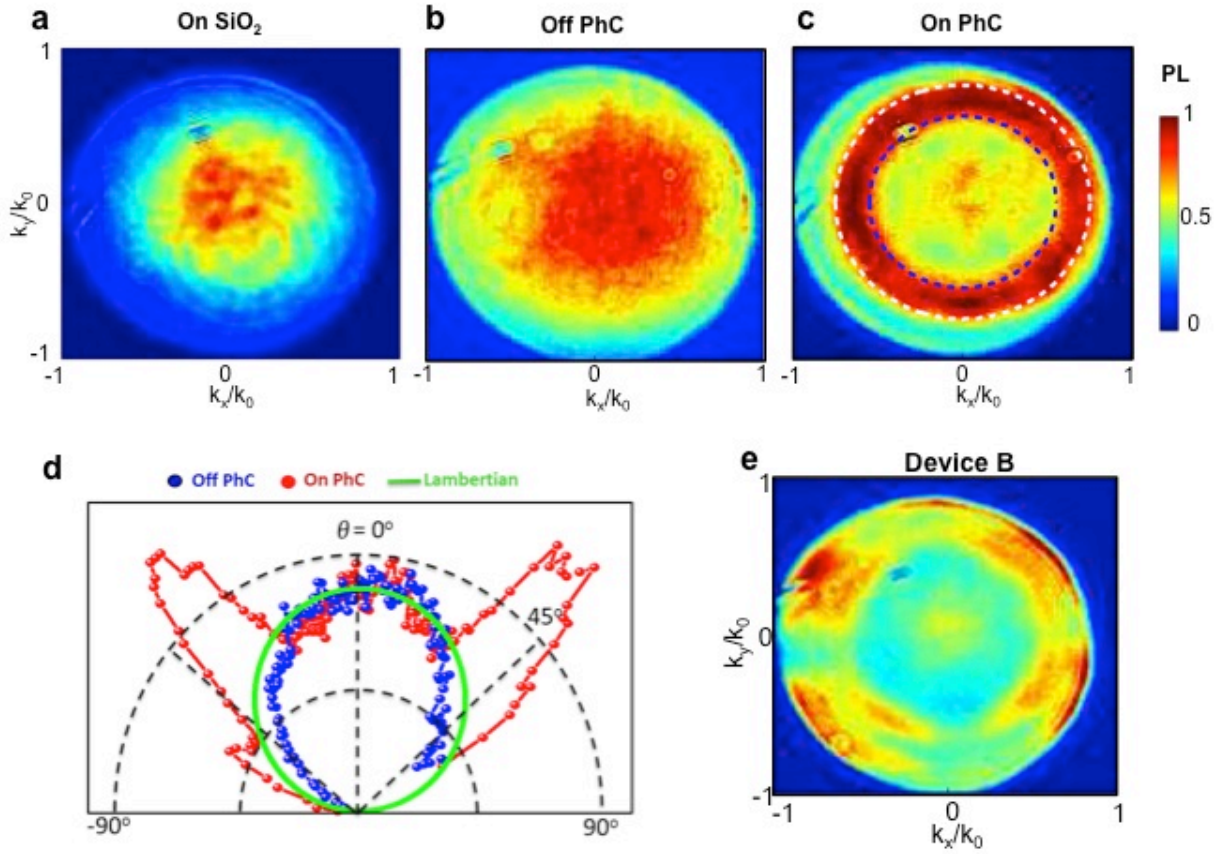

Figure 3.4. Control of the spatial distribution of the 2D excitonic light emission by a PhCC. a, momentum space microscopic map of the excitonic emission when a monolayer WSe_2 is placed on top of SiO_2 substrate b, for GaP substrate but off-PhC region. c, on a PhC region of the first device. d, Polar plot of the emission along k_x =0 for different substrate. The green line is the theoretical Lambertian emission. d, the emission pattern from second device. All the data are taken at room temperature.

This interesting observation in the momentum distribution of the emission can be understood by the diffraction grating effect of the PhC. In the far field, the light coming from such a periodic pattern interferes since the photons from different holes (bright emission spots)

undergo different optical path lengths. The effect can be simulated using a 2D triangular diffraction grating. Due to the lattice constant d being smaller than the wavelength λ, the diffraction equation $\sin\theta = m\lambda/d$ only holds for $m = 0$. The momentum-dependent emission intensity can then be calculated by: $I(\vec{k}) = |\sum_{\vec{\alpha_l}} A_l e^{i2\pi\vec{k}\cdot\vec{\alpha_l}/|\vec{k}|\lambda}|$, where $I(\vec{k})$ is the intensity with wave vector $\vec{k}$, $\vec{\alpha_l}$ is the 2D lattice vector locating the l^{th} hole in the PhC lattice and A_l is the radiation amplitude of the hole. For simplicity we assume $A_l = 1$. We find that this diffraction grating effect well captures our observation, reproducing both emission patterns for the two devices, if proper hole-patterns are selected in the simulations (details in Ref. (*85*)).

Our observations thus demonstrate that the PhC affects not only the spontaneous emission of the monolayer excitons but also the spatial and momentum distributions of the emission. This effect may be further utilized in the future for novel monolayer semiconductor based light sources, such as LEDs and single photon sources.

3.7 HIGH Q CAVITY: NANOLASING

In this section, we will explore the effect of high-Q factor cavities. With improved fabrication techniques, high Q GaP cavity on resonance with WSe_2 emissions can be obtained and we achieved a Purcell factor with about an order of magnitude improvement. The device we present here uses a L3 type PhCC with Q ~ 8000 at wavelength 740 nm (*24*). F can thus be as large as ~ 118. The key to achieving such a high Q factor is to optimize the thickness-to-lattice-constant ratio, and more importantly, to improve sidewall-verticality by lowing the aspect ratio of the etched holes. It is known that an enhanced spontaneous emission rate at the cavity wavelength can reduce the lasing threshold of the emitter. A great outcome is that one may eventually achieve a low threshold laser system with a nanoscale footprint, fast modulation rate and also

low power consumption (*84*, *88–91*). Indeed, such a nanolaser system has been successfully developed in quantum-dot embedded PhCC systems (*75*, *76*). Here we will discuss the possibility of such a nanolaser in the 2D-crystal based surface-gain geometry, which has obvious advantages over conventional systems.

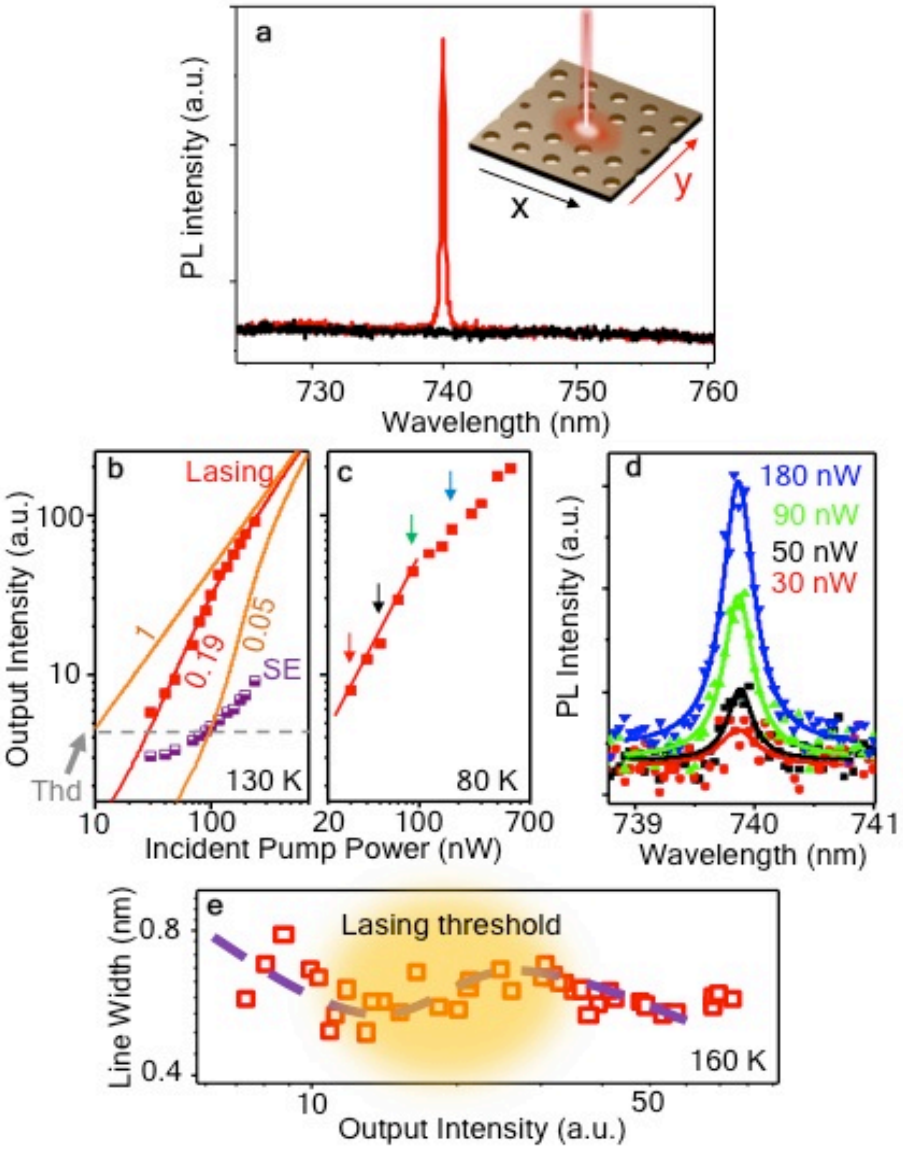

Figure 3.5. Evidences for 2D-crystal-based nanolasing. a, light emission from the monolayer/PhCC hybrids, where the peak is from the cavity mode. The Q factor of bare cavity in this device is ~ 8000. The red (black) curve corresponds to the PL component polarized in y (x) direction. b and c, L-L curves of the device . The lasing characteristic is seen by the superlinear

behavior in the L-L curve of the cavity emission, while the spontaneous emission (SE) is sublinear. The solid curves are simulated from laser rate equations with the corresponding β factor labled. d, the emission spectra at selected pump power near the threshold region, indicated by the arrows in c. e, Linewidth of the emission as a function of the output intensity near the threshold.

Fig. 3.5a shows the emission spectra of this device taken at 80 K. The cavity peak (~ 740 nm) in this high-Q case dominates the emission from the cavity region, where the broad spontaneous emission is inhibited. The polarization of this peak (i.e. y polarized) agrees with the fundamental mode of the cavity. We extract ~ 0.3 nm linewidth of this emission spectrum.

One hallmark signature of a lasing behavior is the superlinear "kink" around the threshold in the light-in-light-out plot. Such a plot is often called L-L curve, which describe the emission intensity as a function of the pump power in log scale. This "kink" indeed can be seen in this device, as shown in Fig. 3.5b and c for temperatures at 130 K and 80 K, respectively. Several selected spectra at 80 K has also been plotted in Fig. 3.5d, which clearly show the superlinear increment of the emission intensity below ~ 90 nW pump power. In Fig. 2.5b, we also plot a set of the off-resonance spontaneous emission, where no such "kink" is observed.

Another signature is the linewidth evolution around the lasing threshold (*92*, *93*). Fig. 3.5e shows the extracted spectral linewidth as a function of emission intensity at 160 K. We also see a clear "kink" behavior around the threshold. When the pump power is below the threshold, the linewidth decreases from about 0.75 nm to about 0.50 nm in response to the increasing power. At the threshold regime, the linewidth re-broadens to about 0.65 nm, and then decreases again to about 0.55 nm. Such "kink" behavior in linewidth is a well-known feature (*84*, *92*, *93*) for semiconductor lasing and has been observed in several developed semiconductor nanocavity lasers. It appears during the phase transition from spontaneous emission into stimulated

emission, where gain-refractive-index coupling significantly affects the linewidth and creats a linewidth plateau (i.e., the kink). This plateau, together with the superlinear "kink" in L-L curve, reveals the lasing behavior of our WSe_2/PhCC hybrid system.

The lasing threshold can be extracted by fitting the experimental data with laser rate equations. One essential parameter to describe a nanolaser is the spontaneous emission coupling factor β, which is the ratio between the emission rate into the cavity mode and the total spontaneous emission rate. The rate equation describes the time-evolution of exciton number N and the photon number P in the cavity (*24*) by:

$$\dot{N} = R_{ex} - \frac{N}{\tau_{SE}} - \frac{aNP}{\tau_{cav}},$$

$$\dot{P} = -\frac{P}{t_c} + \Gamma\frac{N}{\tau_{cav}} + \Gamma\frac{aNP}{\tau_{cav}},$$

$$\beta = \frac{\tau_{SE}}{\tau_{cav}}.$$

R_{ex} describes the optical pumping rate. ${\tau_{SE}}^{-1}$ labels the total spontaneous emission rate. ${\tau_{cav}}^{-1}$ labels the emission rate into the cavity mode. ${t_c}^{-1}$ labels the cavity photon decay rate. The stimulated emission is proportional to $N \cdot P$ with coefficient a. Γ describes the cavity confinement factor. Here we ignore any non-radiative relaxation processes.

The steady state solution of these equations can be found by setting $\dot{N} = 0$ and $\dot{P} = 0$ and we obatin

$$R_{ex} = \frac{P}{\Gamma t_c(1 + aP)}\left(\frac{1}{\beta} + aP\right)$$

The lasing threshold is defined as when the spontaneous emission is equal to the stimulated emission into the cavity, i.e., $aP = 1$. Lasing behavior occurs if $aP > 1$, when the stimulated emission dominates in the system. Our experimental data can then be fitted by with above

equation (Fig. 3.5b), which shows that $\beta = 0.19$ is the best fit at 130 K. We extract the lasing threshold as low as 27 nW, which is comparable to the performance achieved in the quantum-dot/PhCC nanolasers.

Other details, such as the temperature dependent behaviors of this new type of nanolasers, can be found in ref. (*24*). We here summarize that our demonstration points to a new means of constructing nanolasers and also other types of nanoscale photonic devices. Further investigation of such devices, such as their photon statistics, is necessary to establish the emission's coherence properties and substantiate the realistic quality of the devices.

3.8 OTHER INTEGRATED 2D SEMICONDUCTOR-CAVITY SYSTEMS

In addition to the monolayer/PhCC system that we investigated here, there are also reports of other optical nanocavity systems that are coupled with 2D semiconductors, including planar microcavities based on DBR (*79*, *80*), optical microspheres (*26*) and optical microdisks (*25*). 2D TMD lasing characteristics have also been observed in some of these systems, such as monolayer WS_2 embedded in an optical microdisk consisting of Si_3N_4 (bottom) and hydrogen silsesquioxane (top) layers (*25*), along with few layer MoS_2 embedded in an interface between an optical microsphere and a microdisk (*26*). The reported lasing thresholds are very different, which could be due to the large differences in mode volumes and Q factors of these cavities as well as the variant PL quantum yield of the emitters. Future studies are necessary to understand the details of the performances in these systems.

The strong coupling region has also been observed in 2D TMD-cavity system, in particular, MoS_2, $MoSe_2$ or WS_2 embedded in optical nanocavities (*79*, *80*, *94*). Exciton-polariton have been observed and the vacuum Rabi splitting in these structures have been

extracted to be tens of meV. These observations open the door to study 2D-crystal based polariton Bose-Einstein condensation and polariton lasing (*78*).

3.9 FUTURE OUTLOOKS

The field of 2D-crystal based nanophotonics starts from the effort to couple graphene with optical nanocavities from roughly 2012 (*95*, *96*) and it accelerated after TMD monolayers came into play around 2013. Within only a few years, significant progress has been made. While we can foresee a bright future of such "atomic age" of photonics, there is no way to predict what it will look like: will 2D crystals just provide an upgraded version of the existing technologies, or will 2D crystal lead to new possibilities of quantum optics and photonic applications? In the near future, however, there are several directions that may be further developed.

(1) Electrically pumped lasers.

It is clearly important that the electrically pumped lasers need to be developed in order to meet the on-chip optical communication and computation. 2D-crystal based nanolaser offers unprecedented means to achieve such goal. Experimentally, both the concepts of monolayer LEDs and optically pumped lasers have been demonstrated, and the combination of both can potentially be achieved with immediate efforts. Considering the valley and spin physics of monolayer TMDs, future devices harnessing these novel degrees may also be possible.

(2) Devices compatible with silicon photonics.

The current device mostly employs the four kinds of TMDs, which have visible wavelengths. Another direction is to find monolayer semiconductors, or their heterostructures, that emit photons compatible with silicon photonics. On one hand, the silicon optical cavities, such as silicon PhCC, can have much higher Q factors due

to the mature fabrication techniques. This may allow for the observations of interesting phenomena that are unavailable in other systems and allow for improved device performance. On the other, such devices may accelerate the transformation of 2D-crystal based photonic devices.

(3) Nonlinear quantum optics and quantum control.

With improved device quality, one may be able to perform quantum optical studies based on 2D crystals, such as nonlinear optics, photonic blockade, and photonic quantum control (*97*, *98*). Considering the easy fabrication of electrical gates and electrodes to the monolayers, these devices may offer new external knobs to control the states.

(4) Cavity coupled single-photon source.

As we have discussed before, monolayer semiconductors provide unique defect states that emit single photons (*59*). However, the quality of such single photon sources needs to be improved for realistic applications. To couple such a single defect state to an optical cavity is a practical way to achieve this goal and can potentially be achieved by aligning the defects to a PhCC or by embedding a monolayer into a planar optical microcavity. The strong confinement of both light and the defect exciton could also give rise to interesting effects.

(5) Strong coupling region.

Exploration in the strong coupling region has led to the observation of polaritons. Optimizing these systems may eventually lead to the observation of superfluidity of exciton-polaritons and the investigation of polariton-based device applications (*78*).

Chapter 4. 2D OPTOELECTRONICS: PHOTOCURRENTS IN GRAPHENE SUPERLATTICES

In the previous chapters, we mainly focused on 2D TMDs. In this chapter, we will turn to discuss our observations in graphene, focusing on its photocurrent studies. The devices are made from van der Waals heterostructures between graphene and hBN. We will demonstrate the unique optoelectronic properties of such heterostructures, which we find can be utilized to improve the performance of graphene devices. The unique photocurrent responses in both the classical region (low magnetic field) and quantum (high magnetic field) regions will be discussed.

The outline of this chapter is summarized here. In the beginning, we will briefly discuss the current understanding of graphene's quantum Hall effects and graphene photocurrent generations. We then introduce aligned graphene/BN heterostructures, where a moiré superlattice is formed with long wavelengths. The physical consequences of the superlattices will be discussed in both classical and quantum regions and the major results of our photocurrent studies will be presented in both regions. In the classical region, we discuss how this superlattice structure enables multiple hot-carrier collection per photon absorption in graphene. In the quantum region, we discuss the optical responses of the emergent Hofstadter's spectrum, in which transitions of Chern numbers determine the photocurrent generations.

4.1 ELECTRONS IN GRAPHENE: DIRAC FERMIONS AND QUANTUM HALL EFFECTS

Here we briefly review graphene's band structure and its quantum Hall effects (QHEs). Two outstanding features can be found in graphene's electronic energy dispersion: Dirac points (DPs) and van Hove singularities (VHSs). At low energies, electrons in graphene are located close to Dirac points and are described by massless Dirac fermions with both spin and valley degeneracy (*1*, *3*). At high energies, these linearly dispersed cones centered at DPs become nonlinear and meet, creating saddle point VHSs in bands. These VHSs locate at ~ 3 eV above and below the DPs (*1*). Since graphene's discovery, a large number of interesting phenomena have been reported regarding the DPs. Although fascinating phenomena, such chiral superconductivity, have also been predicted with these VHSs, experimental access, i.e., lifting the Fermi surface up to VHSs, is extremely hard and prevent the investigation of graphene VHSs. In the following sections, we will discuss how we can reduce the energy scale of VHSs in graphene and how we can probe and utilize them.

Under magnetic field, massless Dirac fermions develop Landau levels n = 0, ±1, ±2, …, with four-fold degeneracy in each, leading to a unique QHE in graphene (*2*, *3*, *99*). The observed main sequence of the quantized Hall conductivity in unit of e^2/h is $\nu = \pm 2, \pm 6, \pm 10, \ldots$ for monolayer graphene, where ν is the filling factor, h is the plank constant, and e is the electron charge. Under high magnetic field and high carrier mobility, the spin and valley degeneracy may be broken (*100*), leading to a symmetry broken state at $\nu = 0, \pm 1, \pm 3, \pm 4, \pm 5, \ldots$. Up to date the nature of the $\nu = 0$ state is still not clear, which represents one of the mysteries in graphene physics (*101*). Fractional states such as $\nu = \pm 1/3, \pm 2/5, \pm 2/3, \pm 4/3, \ldots$, can be further developed with increasing fields (*4*). In the following sections, we will discuss how additional (anomalous) quantum states emerges from the graphene/BN heterostructures, leading to a remarkably

enriched scenario of QHE, described by Hofstadter's butterfly (*5–7*). We will present the first optoelectronic studies of graphene Hofstadter's butterfly.

4.2 GRAPHENE/BN HETEROSTRUCTURES

When graphene is placed on top of hBN, two effects have been discovered: The first concerns mobility engineering and the second one relates to band engineering. One key feature of graphene's electronic performance is the carrier mobility, which is sensitive to substrate since the 2D states are directly exposed to it. The insulating hBN can be exfoliated into flakes with few to tens of nanometer thickness and can be naturally used as the atomically flat substrate for graphene, in sharp comparison to the rough SiO_2 surface (*102*). Significant improvement of graphene's device performance has been achieved using this idea, including the early design of merely bottom hBN (*102*) and a recent design of hBN/Graphene/hBN sandwich structures (*103*). In the latter, the room temperature mobility of ~ 100,000 cm^2/Vs at a carrier density ~ 10^{12} cm^{-2} has been demonstrated, which approaches the theoretical phonon limits.

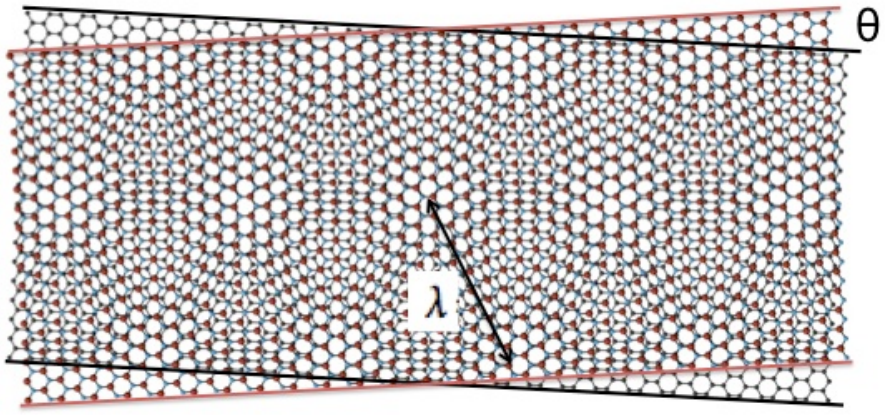

Figure 4.1. Long-wavelength Moiré pattern in graphene/hBN heterostructures when the two crystal lattices are close to be aligned.

The band engineering of graphene through hBN substrate becomes significant when the two lattices are aligned. In this situation, long-wavelength moiré pattern forms (*104*), as shown in Fig. 4.1. The moiré wavelength λ can be determined by: $\lambda = (1+\delta)\, a / \sqrt{[\, 2(1+\delta)(1-\cos\theta) + \delta^2 \,]}$, where a is the graphene lattice constant, δ is the lattice mismatch between hBN and graphene and θ is the twist angle between the two lattices. As a result, the wavelength λ is solely determined by θ given that the two lattices are not strained. The maximum λ is about 14 nm, achieved by precise lattice alignment, i.e., $\theta = 0$, and λ decays quickly to almost zero when θ is driven away from zero.

This Moiré pattern modulates the electron's potential with a much longer periodicity in comparison to its pristine lattice. It thus can open up a way to tune the behaviors of Bloch electrons (*104–106*). In particular, owing to the carrier's Dirac fermion nature, this superlattice modulation in 2D will generate new Dirac fermions and mimic graphene's original spectrum within a reduced BZ (superlattice BZ), instead of opening a bandgap as would expected for the Schrödinger fermions.

Fig. 4.2a plots the simulated band structure at one valley for $\theta = 0$ case (following Ref (*107*)). We can see that in addition to the main DP at zero energy, new secondary DPs (sDPs) emerges at both electron and hole bands, where new minibands develop owing to the superlattice. They locate at ~ 0.2 eV away from DP, which is accessible by simply electrostatic tuning the Fermi surface. This energy location sensitively depends on the twist angle θ. With increased θ, the sDPs will move to high energy and can't be accessed if $\theta > 1^{o}$. This is exceptional because hBN can either provide an excellent substrate without modifying its electronic properties (large θ) or engineer graphene's band structure to a high degree ($\theta < 1^{o}$). In addition to DPs, superlattice minibands also contain saddle point VHS, similar to those at high

energies of pristine graphene bands. Fig. 4.2b shows the calculated electronic density of states (DOS) corresponding to the superlattice energy bands. We can clearly see sharp peaks at both sides of the two sDPs, labeled by A-D. These peaks indicated the formation of VHS at low energies in the minibands. In the following sections, we will provide experimental observations of these VHSs.

This van der Waals band engineering has led to several interesting observations. (1) It has been revealed that the massless Dirac fermions in graphene become massive due to the bandgap opening at DP and sDPs (*6*). (2) Upon the bandgap opening and inversion symmetry broken induced by hBN lattice, the two degenerate valleys become distinguishable, leading to the observation of topological valley transport (*44*). (3) In addition to the sDPs, third generation of DPs emerges in the system if a high magnetic field is applied perpendicularly (*7*). Under this circumstance, the long-pursued Hofstadter's butterfly appears and creates fractal QHE (*5*–*7*). A review of Hofstadter's butterfly will be presented in next sections.

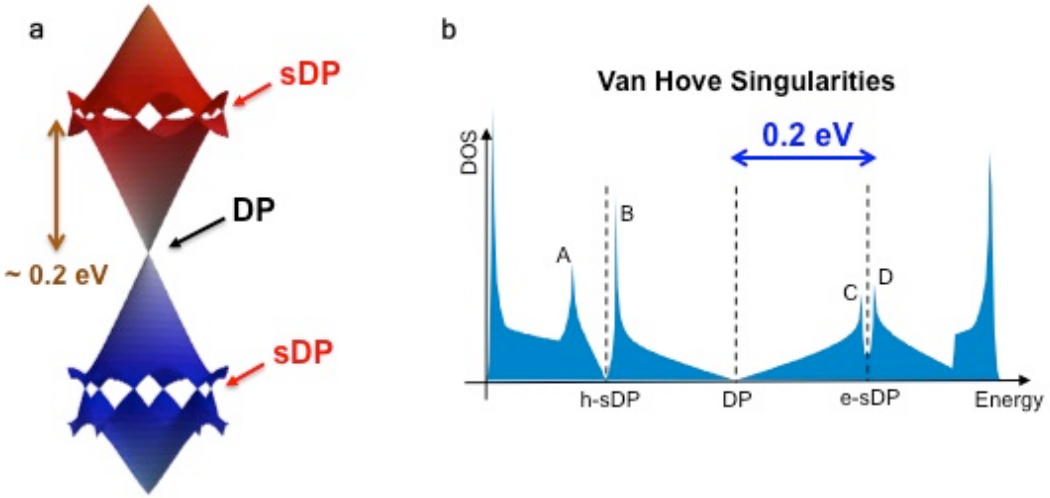

Figure 4.2. The simulated band structure of graphene superlattice. a, energy bands for one valley calculated by assuming θ = 0. Both DP and sDPs can be clearly seen. b, the DOS corresponding to a. Nearby sDPs, there are VHSs (A-D) located at both sides of each.

4.3 HOFSTADTER'S BUTTERFLY

In this section, we will discussion how the 2D electrons in graphene superlattices behave when they are simultaneously subjected to a perpendicular magnetic field. The question is to ask what the energy spectrum will look like if the period of electron's lattice potential is comparable to the magnetic length. In 1976, Hofstadter first published a solution to this question using 2D rectangular model, where he discovered a fascinating energy spectrum containing energy bands and gaps that exhibit fractal behaviors and self-similarities (*108*). This is before the discovery of QHE. Thanks to the observation of QHE, it was later realized that the gapped states in the Hofstadter spectrum are topologically distinguished from others. The topological invariants associated with the quantized states are the Chern numbers, which corresponds to the Hall conductivities in unit of e^2/h. Below we summarize the key features to understand the physics of Hofstadter's butterfly from both the "gap" and "band" points of view.

(1) Wannier diagram.

In Hofstadter's spectrum, there are empty regions where no states are allowed, forming energy gaps. In 1978, Wannier published his interesting results characterizing all the gaps in the spectrum (*109*). Instead of focusing on the eigenenergies, Wannier consider the spectral weight below a given gap (i.e., the electron density when the Fermi level is parked in the gap). This leads to the development of Wannier diagram, where the gaped states are described by Diophantine equations: $n/n_0 = t\,(\Phi/\Phi_0) + s$. Here n is the electron density in the system, $n_0 = 1/A_c$ is the inverse of the area (A_c) of a lattice unit cell, Φ is the magnetic flux penetrating the unit cell, $\Phi_0 = h/e$, is the flux quantum. s and t are two quantum numbers that describe the gaps, corresponding to the intercept and slope of the linear equations. In the quantized region, physical meanings of the two quantum numbers are clear: t is the Landau-level filling factor (i.e., the

Chern number) and s is the Bloch-band filling factor. In integer QHE (non-interacting region), t and s are both integers. In the limit of much shorter lattice wavelength than the magnetic length, one can only observe the quantized states associated with s = 0, i.e., the normal QHE. However, when the two lengths are comparable, s can be other integer values, leading to the observations of anomalously quantized states characterized by fractal QHE. In the interacting region, t can also be fractional numbers, such as 1/3, 2/3, which correspond to fractional QHE.

(2) Fractal bands.

In addition to looking at the gaps, one can also of course focus on the bands. The fractal bands of Hofstadter's spectrum recursively repeat themselves. This recursive behavior can be partly summarized as following: in the presence of magnetic flux $\Phi/\Phi_0 = p/q$, each single band at zero field is developed into q sub-bands (*108*); each sub-band is recursive to the original band. Here p and q are integers. There are two direct outcomes. First, at fractional flux, even though the applied external magnetic field is nonzero (or even large), the electrons effectively experience zero fields in an enlarged lattice (*7*, *110*). When the flux is tuned below (above) the fractional values, the effective magnetic field become negative (positive). Second, the features in the zero-field bands will be cloned in the high-field fractal bands, at different energy scales. For example, one interesting feature in a zero field band of a 2D lattice is the existence of a saddle point VHS, as we have disused before. Upon the applied field and the development of Hofstadter's spectrum, such VHS will recursively appear in every fractal band.

The observation of such Hofstadter's butterfly lies on two aspects: (1) The two length scales are comparable; (2) electrons moving in the system acquire high mobility, so that the QHE can be developed. Graphene/hBN superlattices thus provide an ideal platform to observe such fractal quantum phenomena. To one aspect, the superlattice wavelength can be as long as ~ 14

nm, corresponding to ~ 25 T in terms of magnetic length. To the other, electrons and holes has very high mobility when graphene is placed on top of BN. Indeed, in 2013, three independent groups reported their elegant observations of Hofstadter's butterfly in graphene superlattices (*5*–*7*). A recent observation in the interacting region revealed new states corresponding to fractional values of s, which calls for further understanding of QHE and Hofstadter's physics (*8*). Next we will turn to discuss the optoelectronic responses of graphene superlattice in both the classical region and quantum region.

4.4 GRAPHENE PHOTOCURRENTS: PHOTO-NERNST EFFECTS

Before we go into the details of our experiments on graphene superlattices, we briefly introduce the current understanding of (pristine) graphene's photocurrent response. Due to the weak electron-phonon interaction, photoexcited carriers in slightly doped graphene prefer to transfer their energies to electrons at Fermi surfaces through carrier-carrier heating during the initial relaxation stages (sub-ps), instead of transferring their energy directly to phonons (*111*–*114*). This can then heat up the electrons at the Fermi surface (Fig. 4.3), leading to hot-carriers located at the position of laser excitation. The thermal diffusion of hot-carriers from hot to cold places can develop photo-thermoelectricity (*111*), which is known to be the driving force for photocurrent generation in many graphene devices, such as graphene p-n junctions (*112*, *115*), single-bi-layer junction (*111*) and even graphene-metal junctions (*116*). This unique hot-carrier mechanism doesn't necessarily require a p-n junction or electrical bias to generate photocurrent. One good demonstration is the observation of the photo-Nernst effect (*117*), where the current is driven by Nernst effect of the hot carriers (Fig. 4.4). Two conditions need to be satisfied in order to observe photo-Nernst effect: (1) an anisotropic temperature gradient; (2) an external magnetic field. Below we discuss the details of this effect.

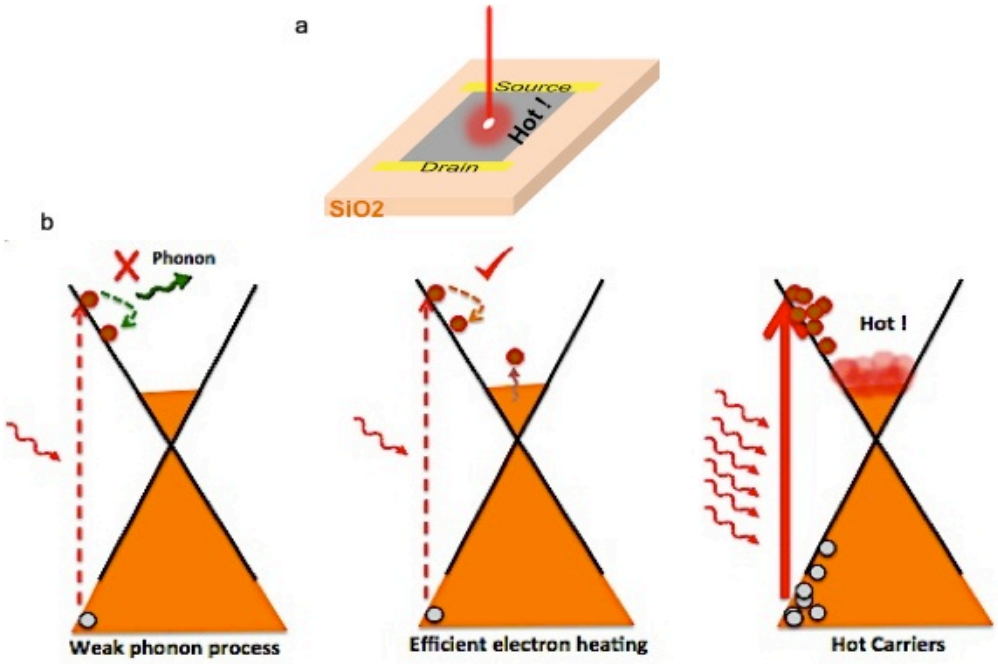

Figure 4.3. Hot carriers in graphene. a, hot center of a typical device on SiO_2 generated by a laser beam. b, the generation of hot carriers is due to the weak electron-phonon interaction. Instead of transferring their energy to phonons, the photoexcited high-energy carriers, at early stage, release energies though exciting the electrons at Fermi surface, creating hot carriers at the surface.

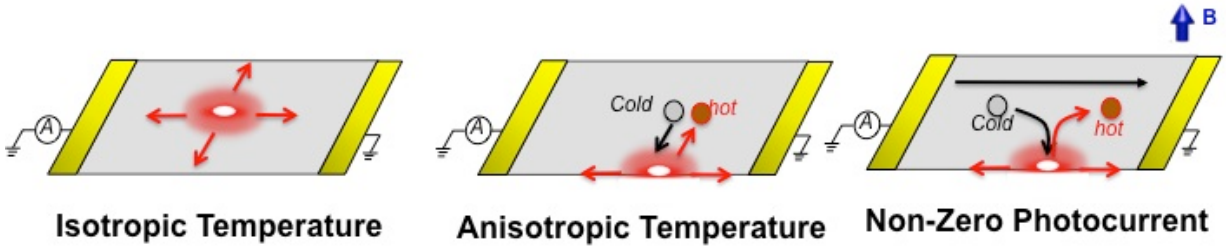

Figure 4.4. An intuitive picture of photo-Nernst effect. The diffusion of hot carrier occurs when the laser beam is focus onto the bulk of graphene, where no net photocurrent is observed. This is due to the isotropic temperature gradient in the bulk. If one moves the beam to graphene edge, an anisotropic temperature gradient forms; however, the photocurrent is still zero, due to the symmetric diffusion of both cold and hot carrier. When a perpendicular magnetic field is simultaneously applied, the trajectories of cold and hot carriers will bend, leading to photo-Nernst effect, where a net current along the transverse direction.

The first experimental demonstration of photo-Nernst current is by Cao et al in Ref. (*117*), where they measured the zero-bias photocurrents under magnetic field in a graphene FET on SiO_2. They revealed that the photo-Nernst current appears at the edges of graphene samples, and switches its sign either when the magnetic field is flipped or when the laser beam is moved to the opposite edge. The conversion efficiency of the observed current is comparable to, for example, p-n junction geometry, with a photoresponsivity about 1 mA/W.

The photo-Nernst mechanism can be formulated by relating the short-circuit current to the transverse thermoelectric power S_{xy}, which is proportional to the Nernst coefficient *N* and magnetic field strength B at low field limit (*117*). The relation can be written as: $I_{pc} = S_{xy}\langle\Delta T_{el}\rangle/\rho_{xx} \propto S_{xy} / K_{th}\,\rho_{xx}$, where $\langle\Delta T_{el}\rangle$ is the temperature gradient of the hot carrier, K_{th} is the electron's thermal conductivity and ρ_{xx} is the electron's longitudinal resistivity. $K_{th} \propto 1/\rho_{xx}$ if the Wiedemann-Franz law stands in the system. Therefore we have $I_{pc} \propto S_{xy} \equiv N\,B$. One can see that the photocurrent generation is determined solely by the Nernst coefficient given a fixed magnetic field. Next, we will discussion our observations of photon-Nernst effect in graphene/hBN superlattice.

4.5 PHOTO-NERNST EFFECTS IN GRAPHENE SUPERLATTICES

The devices we studied were graphene encapsulated between hBN layers placed on a graphite gate. The fabrication techniques were recently developed by Prof. Cory Dean and Prof. James Hone's groups at Columbia University, where they used polymer-free transfer procedures and an edge-contacted Hall-bar geometry (Fig. 4.5a) was employed to achieve high-quality performance. The samples discussed in this chapter were fabricated by the Columbia groups. In order to perform optical studies, a large (~ 100 μm^2) and clean area of the sandwiched structure was defined as the transport channel. Such devices allowed us to conduct spatially resolved

photocurrent measurements (Fig. 4.5b), as well as characterize resistivities in both longitudinal and transverse directions. Fig. 4.5c plots the longitudinal resistance R_{xx} as a function of gate voltage, where three peaks are clearly seen. These R_{xx} peaks are hallmark of the formation of long-wavelength Moiré superlattice structure, which could be due to the precise alignment between graphene and one of the two hBN sheets (*5–7*, *104*, *118*). The peaks indicate the location of DP and sDPs. Otherwise mentioned, all the measurements we discuss here were performed at 4.2 K in a superconducting magnet.

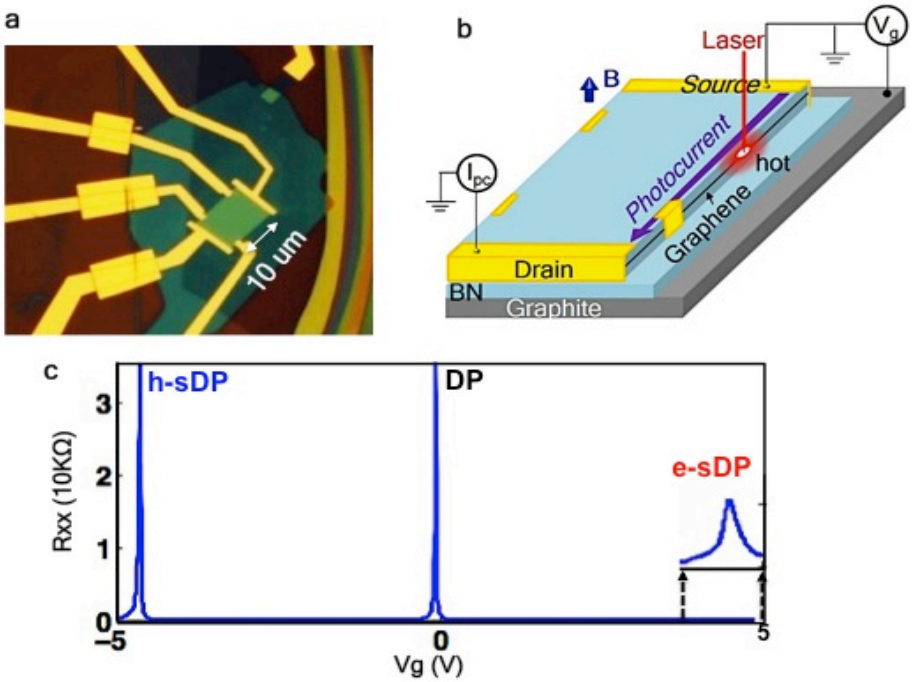

Figure 4.5. Graphene superlattice devices. a, an optical image of one typical device, where edge-contacted graphene encapsulated between BN sheets are fabricated into Hall-bar geometry. b, Cartoon depicting the measurement geometry. c, Rxx as a function of gate, showing three peaks. This is the hallmark feature of the formation of long-wavelength Moiré pattern in the device.

We then present the observed photocurrents in this device (*119*). We focused a 660 nm CW laser beam onto a selected graphene edge. The photocurrents were collected through the

drain contact while the drain was grounded (Fig. 4.5b). The bottom panel of Fig 4.6 shows the recorded zero-bias photocurrent as a function of gate under variant magnetic field B from -50 mT to 50 mT. The top panel shows the R_{xx}, indicating the location of DP, hole-side sDP (h-sDP) and electron-side sDP (e-sDP). Two types of interesting features can be identified in the photocurrent data: the first type is B-independent and the second type is B-dependent. The B-independent feature, such as the dip aligned with the h-sDP, indicated by grey arrow, is not understood currently. We here will only focus on the B-dependent features, such as the peaks shown by red arrows. These photocurrents will flip its sign when B is flipped to opposite direction. We also confirmed that they have opposite sign for opposite edge, all agreeing with the photo-Nernst effect (*117*). Indeed, in the following discussions we will unambiguously confirm their photo-Nernst nature.

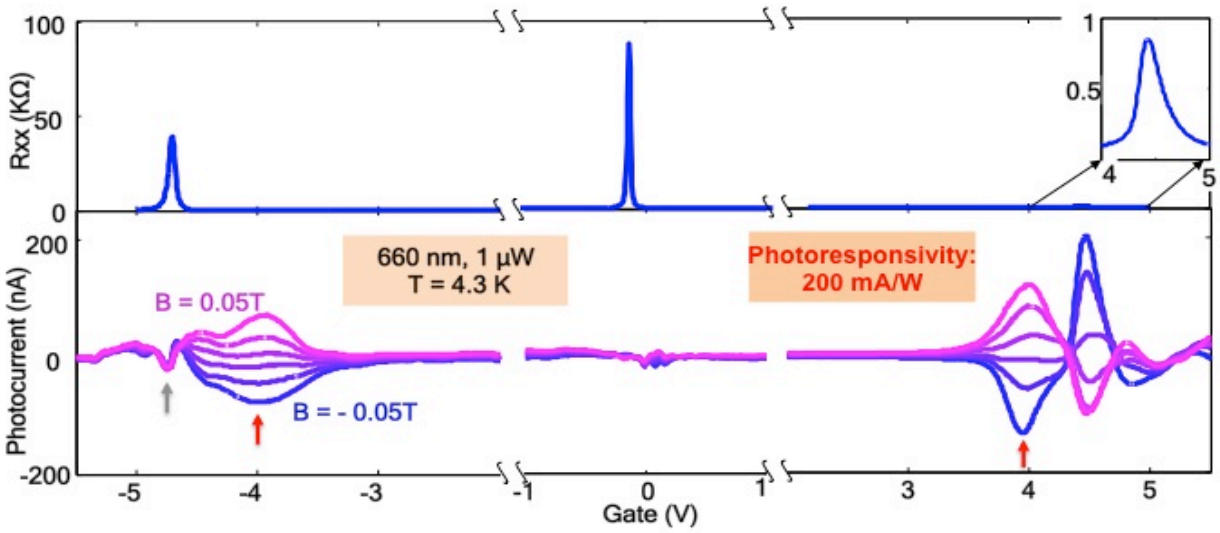

Figure 4.6. Photo-Nernst effect in a graphene superlattice. Top panel: R_{xx} as a function of gate voltage, indicating the positions of DP and sDPs. Bottom panel: the zero-bias photocurrents taken under variant magnetic field at a selected edge. The laser wavelength is 660 nm and the power is 1 uW before the objective.

Here we summarize two important properties of the features identified by the red arrows. (1) They are close to, but not aligned to, the sDPs, for both electron and hole sides. (2) They have a giant photoresponsivity ζ. At B = -50 mT, the maximum observed photocurrent already appears as large as ~ 200 nA with about 1 uW incident, which corresponds to a ζ ~ 0.2 A/W. It is about two orders of magnitude larger than previously reported photo-Nernst current in graphene on SiO_2 devices. Fig. 4.7 plots ζ at V_g = 4 V under variant B up to 0.5 T. It clearly shown that ζ can be as large as 0.3 A/W at 0.25 T. The photocurrents increases linearly under ~ 0.1 T, agreeing with the Nernst mechanism, where a linear relation between photocurrent and B is expected at low field. Such a giant ζ is more than 30 times larger than the reported values in any graphene photodetectors under the conditions of short-circuit and normal-incidence (*120*). In the next section, we will discuss the remarkable aspect of these giant photocurrents and explain them.

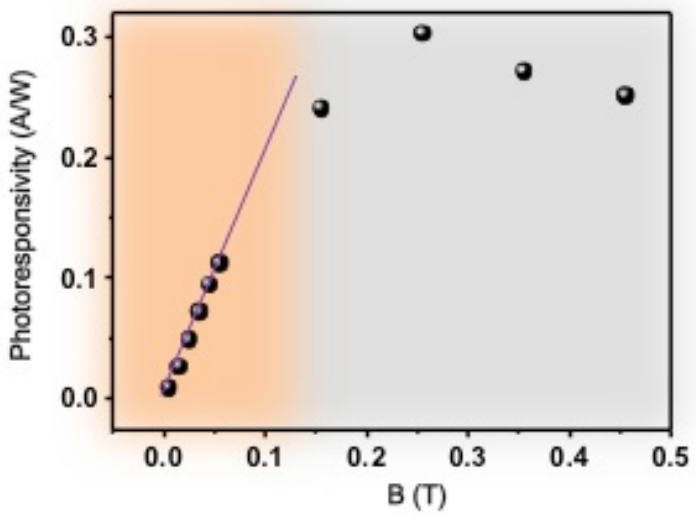

Figure 4.7. Photoresponsivity ζ as a function of B at Vg = 4 V. The solid line is an eye-guide to the low field data, which shows a linear relation between ζ and B, consistent with the photo-Nernst mechanism. The saturation at high fields is due to the transition into quantum region.

4.6 MULTIPLE HOT-CARRIER COLLECTION

It is very interesting to calculate the external quantum efficiency η of the device. η is another figure of merit of a photosensitive device, which describes the ratio between the number of collected carriers and the number of the incident photons. It can be calculated by $\eta = \frac{I_{pc}}{e} / \frac{p}{\hbar\omega} = \zeta\hbar\omega/e$, where I_{pc} labels photocurrent amplitude, p labels excitation power, and $\hbar\omega$ is the photon energy. We then obtain η exceeding 50% in our graphene superlattice device. As a result, the internal quantum efficiency largely exceeds 100% since the absorption of graphene is very low. The absorption coefficient α is expected to be ~ 2.3%, with an upper limit of ~ 10%, considering the modulation from superlattice structure. This tells us that at least 5 carriers are collected in our device upon the absorption of every single photon. This is rather conservative estimation, since the laser only illuminates the edge of the sample (i.e., a portion of incident power is off sample) and the absorption in reality could be less than its maximum value. Our observation thus unambiguously achieved the collection of multiple hot-carriers per photon absorption in a graphene device.

One immediate question regarding the above observations is: how is the multiple carrier collection possible in graphene superlattice?

To explain the origin of multiple hot-carrier collections, one needs to glue two pieces of graphene physics together. The first piece is the hot-carrier multiplication, which is simply a different point of view of the carrier heating process that we have previously discussion. In doped graphene, photo-excited carriers release their absorbed energy though exciting secondary electrons at the Fermi surface. As a result, these high-energy carriers undergo a cascade of relaxation and multiple hot carriers are generated. This process has been well studies in both theory (*113*, *114*, *121*) and experiments, where optical and ARPES measurements have

confirmed the picture (*121–125*). This is generally true in doped graphene samples with high quality.

The second piece is, however, unique to our superlattice structures. We have mentioned that the giant photocurrents happen at the vicinity of sDPs, but do not exactly locate at the sDPs. This reminds us the superlattice VHSs emerged at low energies (Fig. 4.2b), which also appear nearby each sDPs. It points to us that the photocurrents could be connected to the VHSs. This is not surprising because VHSs are known to create anomalies in material's fundamental properties. For example, they host very high electron density of states and the carrier's type undergoes a sudden change from electron-like to hole-like at VHSs. In Fig. 4.8a, we schematically draw the evolution of Fermi circles when the Fermi energy is tuned from h-sDP to DP, simulated for the superlattice BZ at one valley (details in Ref. (*119*)). One can clearly see that the carrier changes suddenly when the Fermi energy crosses the saddle point VHSs.

These electronic structures can significantly affect graphene's conductivity and thermoelectricity. The latter is of actually particular importance to graphene photocurrents, since they are usually driven by photo-thermoelectricity. In Fig. 4.8 b and c, we plot the measured conductivity in both transverse (σ_{xy}) and longitudinal (σ_{xx}) directions at 0.5 T. We can see that σ_{xx} contains striking peaks while at the same place σ_{xy} suddenly changes its sign (Lifshitz transition). These observations unambiguously demonstrate that the superlattice VHSs indeed exist in our devices and they can be identified by conductivities. In order to reveal the connection between the photocurrents and VHSs, in Fig. 4.8d we plot the photocurrents, where the enhanced structures are well aligned with the VHSs. This indicates that the giant photocurrents in graphene superlattices originate from the emergent VHSs. The slight misalignment of the I_{pc} peaks and σ_{xx} may be due to the optical doping effect induced by laser.

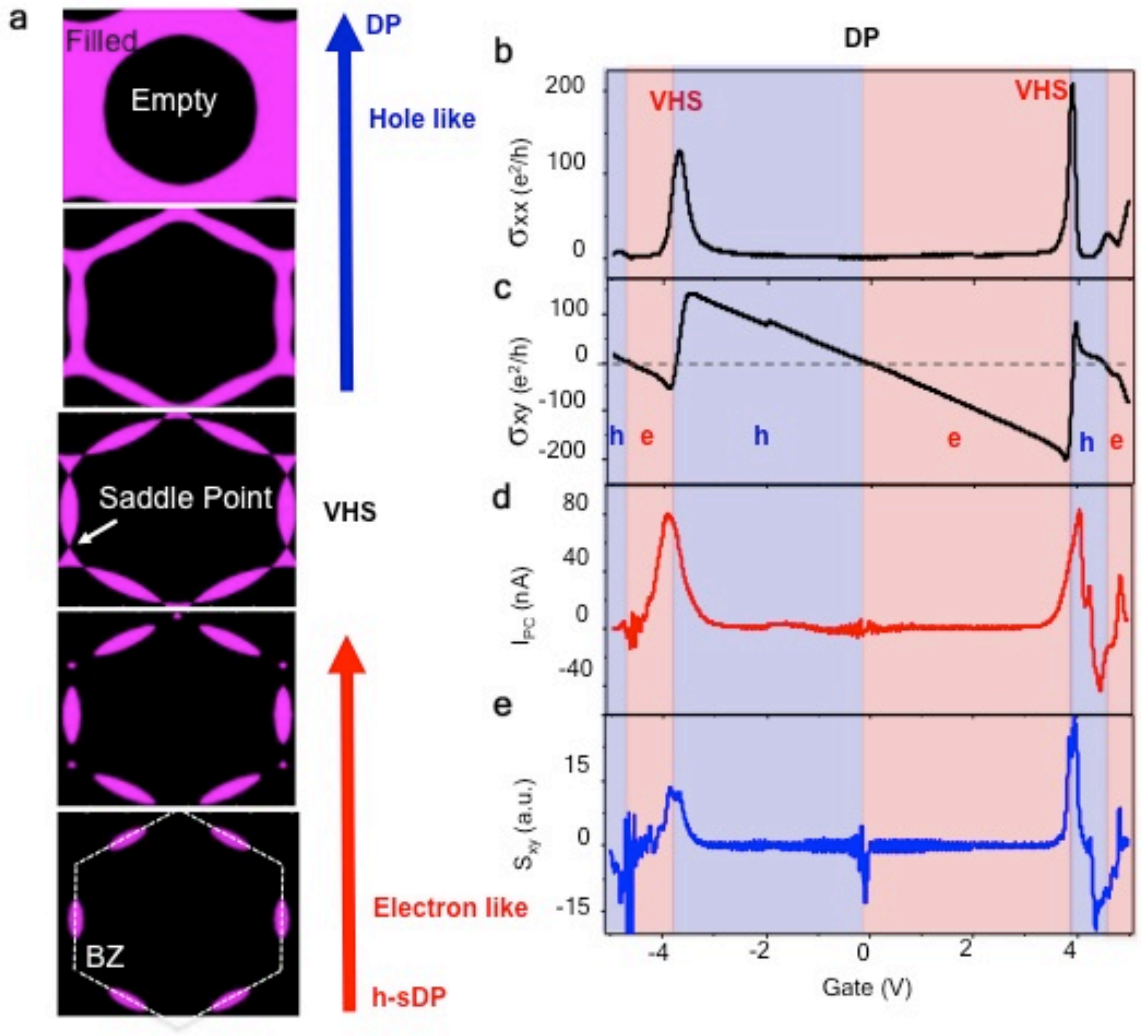

Figure 4.8. VHSs boost the collection of hot-carriers in graphene superlattice. a, Theoretical simulations show the evolution of Fermi circles when the Fermi energy is increase from h-sDP to DP, passing the VHSs. The carrier types changes suddenly from electron-like to hole-like, highlighting the Lifshitz transition. b, longitudinal conductivity σ_{xx} as a function of gate voltage taken at 0.5 T. c, the corresponding transverse conductivity σ_{xy}. d, The measured zero-bias edge photocurrent. e, The calculated S_{xy} from Mott formula.

The giant photocurrents can now be understood. At the Lifshitz transitions, the thermoelectric response is remarkably enhanced, leading to a large photo-Nernst current. We have pointed out that photo-Nernst current is proportional to transverse thermoelectric power S_{xy}, which can be calculated using the standard Mott formula, $S_{xy} \propto (\sigma^{-1})_{xx}\left(\frac{\partial\sigma}{\partial E_f}\right)_{xy} + (\sigma^{-1})_{xy}\left(\frac{\partial\sigma}{\partial E_f}\right)_{yy}$, where E_f is Fermi energy (*126*). We plot the result in Fig. 4.8e, where we can see that the features in I_{pc} can be reproduced in S_{xy}, except the disagreement at the exact DP and sDPs where the Mott formula may be not valid. We thus can confirm that (1) the observed photocurrent is arising from, indeed, the photo-Nernst effect; and (2) it is the Lifshitz transitions at superlattice VHSs that enables the giant photocurrent generations.

Now we can glue the two pieces of physics together. When one park the Fermi level at the VHSs formed in graphene superlattice, the photoexcited carriers efficiently transfer their energies by creating multiple hot-carriers at the VHSs. These multiplied hot carriers can subsequently be efficiently extracted forming current, due to the significantly enhanced thermoelectric power at VHSs. The combination of an efficient hot carrier generation and extraction enable the multiple hot-carrier collections in our systems.

In summary we have demonstrated how to utilize graphene's unique hot-carrier multiplication process and points to a new means to enhance photocurrent generation by engineering VHSs. In the context of broader interest, carrier multiplication was developed in quantum dot system initially, with a hope to improve the energy-converting efficiency of optoelectronic devices, such as solar cells (*127*). It is believe that with a material that can achieve multiple carrier collection, one may be able to overcome the Shockley-Queisser efficiency limit for converting light into electricity. However, no clear picture of how the realistic device can be

made and how the collection of multiplied carriers can be achieved in traditional systems. In our case based on graphene, we have taken one step forward by realizing the collection of multiple carriers.

4.7 HIGH FIELD: PHOTOCURRENT HOFSTADTER'S BUTTERFLY

In this section, we turn to discuss the photocurrent generation in graphene superlattices in the quantum region by sweeping the magnetic field (up to 17.5 T). We keep the measurement setups the same as the previous. Fig. 4.9a plots the recorded photocurrent "fan diagram" with two axes of B and Vg. The white color corresponds to zero current, while the red (blue) indicates positive (negative) photocurrents. There are a few interesting features can be identified in this photocurrent diagram. The purpose of this section and the following two sections is to understand these features.

It will be useful to compare the photocurrent fan diagram with the resistance (R_{xx}) fan diagram, as shown in Fig. 4.9b. The R_{xx} fan clearly reveals the physics of Hofstadter's butterfly (*5*), where t)he gaped quantum Hall states (QHSs) can be identified by the blue (i.e., minimum value) linear traces and the DP, sDP and the third generation of DPs (tDPs) are the focal points of the gapped traces. As we have discussed before, the gapped QHSs in the Hofstadter's butterfly can be well characterized by Wannier diagram, which is shown in Fig. 4.9c. In this Wannier diagram, we generate the traces by plotting Diophantine equations: $n/n_0 = t\ (\Phi/\Phi_0) + s$. The experimentally observed gaped-state traces are highlighted in the diagram, where the black traces correspond to the main QHSs starting from main DP and sDPs, the blue traces correspond to the symmetry broken states, and the pink traces correspond to the anomalous QHSs due to the fractal nature of Hofstadter's spectrum. We also label the associated (s, t) quantum numbers selectively.

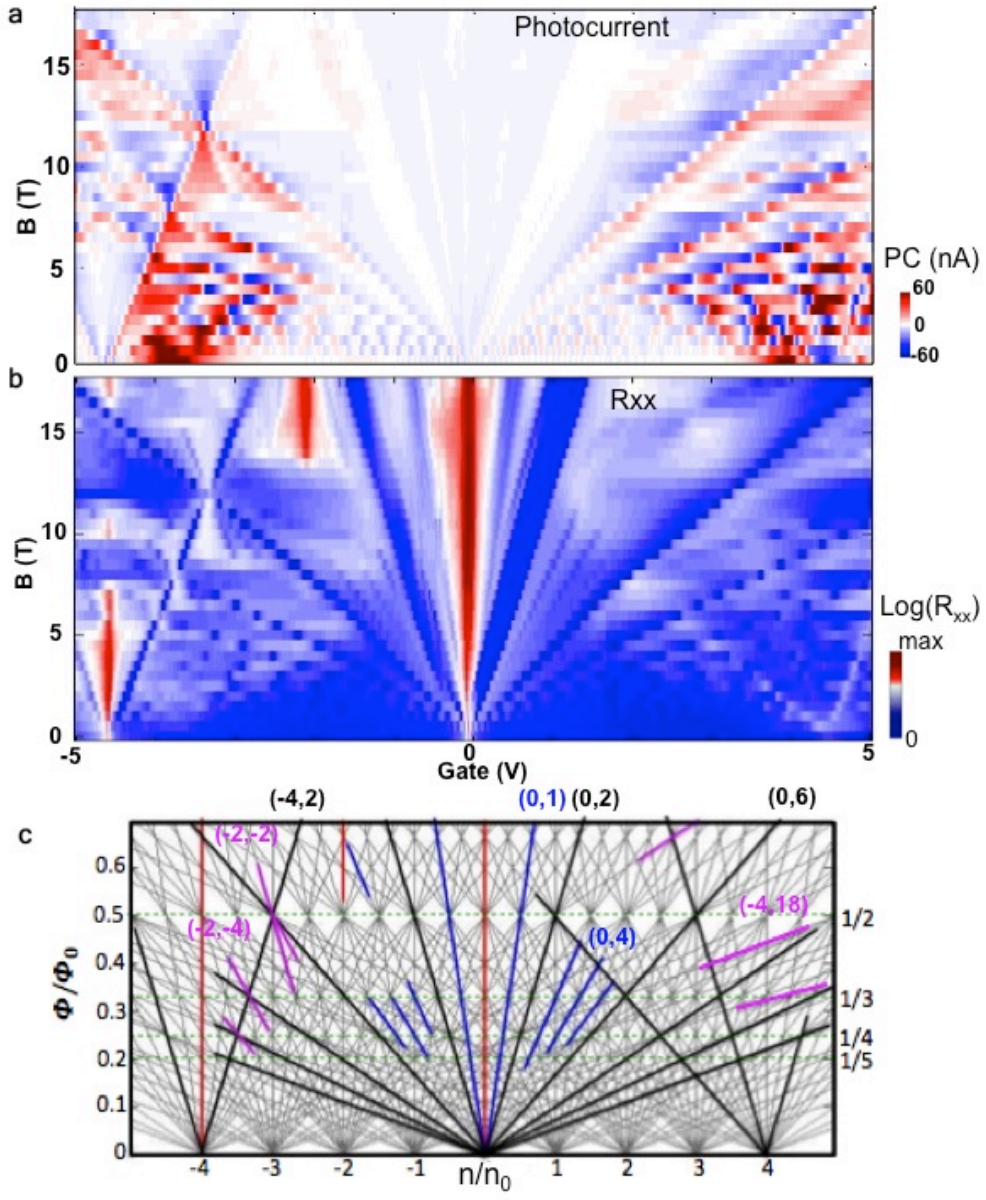

Figure 4.9. Photocurrent Hofstadter's butterfly. a, Photocurrent fan diagram, taken under the photo-Nernst geometry as previously discussed. b, the R_{xx} fan diagram, which shows the standard resistance behaviors of a butterfly device with a long-wavelength superlattice structure. c, the Wannier diagram, capturing the observed QHSs. The highlighted traces capture the experimentally observed states and the colors labels the states with different properties (see in the text). The green dashed lines indicate the locations with fractional values of magnetic flux, where the tDPs appear.

One can immediately see that, similar to the resistance diagram, the photocurrent diagram also captures the Hofstadter's physics, where the white traces ("zeros" of photocurrents) directly reveal the gapped states. In addition to these photocurrent zeros, we here also summarize several other interesting features in photocurrents that capture the quantum structure of the system: (1) The photocurrent changes its sign frequently in the diagram; (2) distinct structures appear at DP, sDP and tDPs; (3) the photocurrents are significantly larger at the two sides of the diagram, where the fractal bands live. Next, we will explain all these features.

4.8 PHOTO-NERNST EFFECT UNDER HIGH FIELDS

We first demonstrate that, even under high magnetic fields, the observed photocurrents are still photo-Nernst currents. One can simply check that the current indeed switch its polarity when either the direction of B or the edge is switched to the opposite, consistent with photo-Nernst mechanism. As we've known, the smoking-gun evidence can be obtained by comparing the current with $S_{xy,}$ which can be computed through Mott formula if one knows the fan diagrams of both conductivities σ_{xx} and σ_{xy}. We present the result in Fig. 4.10. It clearly shows similarity between the two fan diagrams of S_{xy} and I_{pc}. Except at the very vicinity of DP and sDPs, where the Mott formula may be invalid, the calculated S_{xy} (*126*) captures most of the features appearing in the photocurrents. Therefore, in such clean samples, the photo-thermoelectricity still dominates the photocurrent generation in graphene. This is interesting because it suggests that, even in the quantum region, the photo-excited carriers in graphene maintains their uniqueness and they can be hot while the lattice stays cold.

Although we have confirmed the photo-Nernst nature of the currents, the underlying physics of the photocurrent current, i.e., the origins of the Nernst coefficient, is still unclear.

Next we will reveal that the observed photocurrents are a direct manifestation of the topological transitions in the Hofstadter's butterfly.

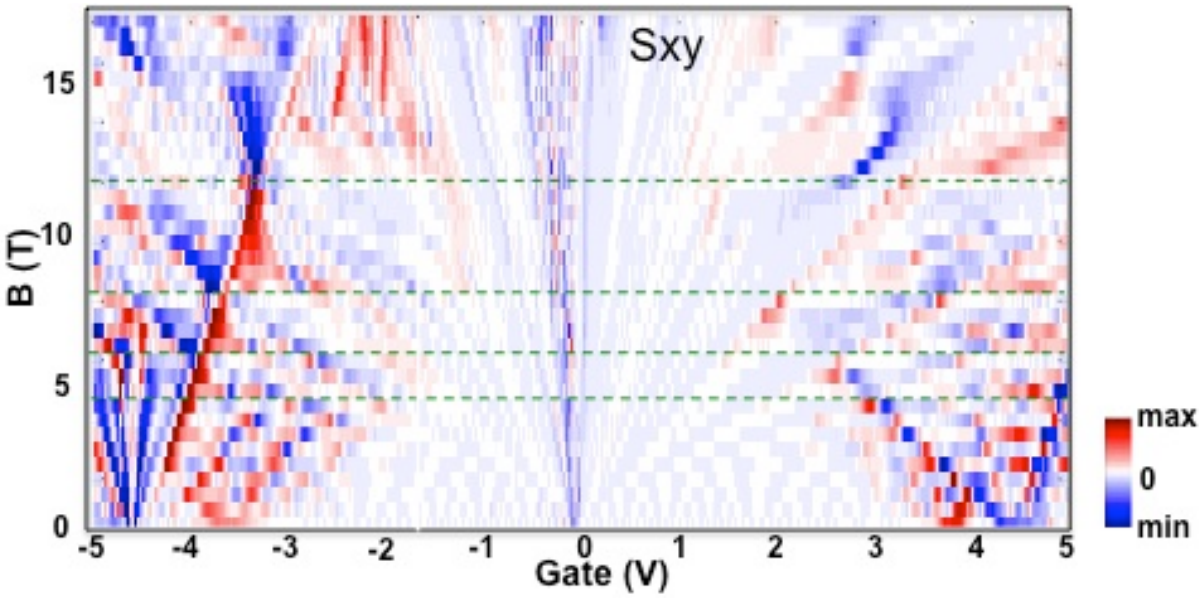

Figure 4.10. Calculated S_{xy} fan diagram from Mott formula and measured conductivities. The green dashed lines indicate the locations of fractional magnetic flux.

4.9 CHERN NUMBER TRANSITIONS: STEP TRANSITIONS AT LANDAU LEVES

It is helpful to think about the Hofstadter's butterfly from the view of Chern numbers, which topologically characterize the gaped states in the spectrum. The spectrum of a graphene superlattice under magnetic field is therefore a collection of Chern numbers. For example, in the sequence of the QHSs originated from the main DP, the associated Chern numbers are $\nu = \pm 2$, ± 6, ± 10 and ± 14, …. The Chern numbers thus undergo a step transition at each Landau level, and become a fixed integer (topological invariant) when the Fermi level is located in the gaps between Landau levels (Fig. 4.11a). In the fully quantized region, there are no carriers responsible for the thermoelectric transport in the gaped region, and we thus expect zero plateaus for both S_{xy} and I_{pc}. During the Chern number step transitions, non-zero photocurrent will be

generated due to the finite S_{xy}, whose sign change once within each Landau level due that the carrier changes its type from electron-like to hole-like. Such behaviors are summarized in Fig. 4.11b, where each step transitions of Chern numbers leads to one period of oscillation of photocurrent. This is indeed what we have seen from our photocurrent fan diagram, where both photocurrent zeros are seen for the gaped QHSs and a rapid sign changes are developed between gaps.

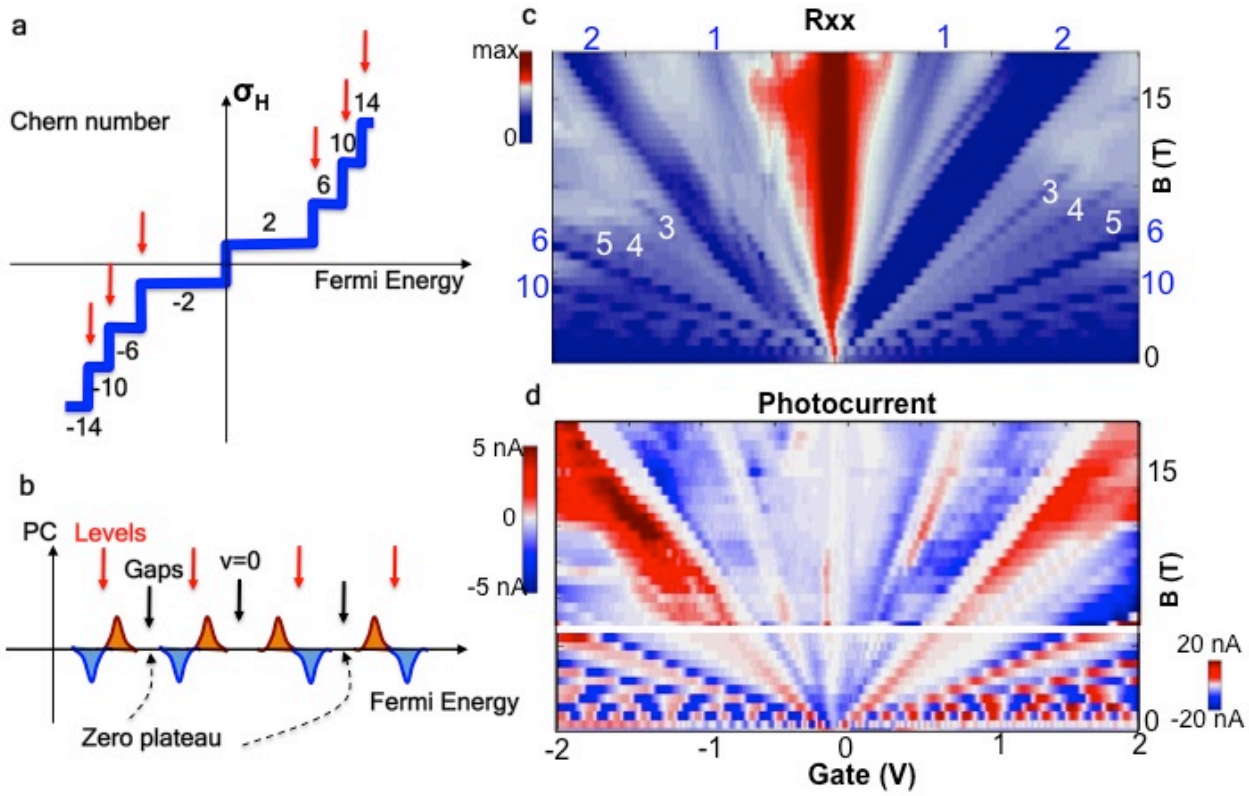

Figure 4.11. Photocurrents as a manifestation of Chern number step transitions. a, Chern numbers of QHSs and transitions at Landau levels. b, Theoretical expected photo-Nernst currents at Chern number transitons. c, R_{xx} fan diagram for the main QHSs originated from DP. d, the corresponding I_{pc} fan diagram, where the upper and bottom parts are plotted in different color scale, in order to highlight both the low and high field features.

To better see this, we plot both R_{xx} and I_{pc} for the main QHSs near DP in Fig. 4.11 c and d. The regions with integer filling factors, or well-defined Chern numbers, can be identified

through the R_{xx} fan. One can clearly see the zero photocurrent plateaus at these integer filling factors and also oscillating photocurrent developed in the fan. This observation demonstrates that the photocurrent is a direct manifestation of the step transition of Chern numbers. It is also true for the entire Hofstadter's spectrum, which is a mosaic of Chern numbers. In Fig. 4.9a we can see that the zero plateaus also develop for the anomalous QHSs and this explains why the photocurrent fan captures the topological texture of the butterfly (i.e., Wannier diagram).

4.10 CHERN NUMBER TRANSITIONS: COLLAPSE AT VHSS

In section 4.3, we have pointed out that in the Hofstadter's spectrum each energy band at 1/q flux splits into q fractal bands, in which electron experiencing zero effective fields, and each fractal bands contains a VHS. These fractal VHS is recursive to the zero-field VHS. Intriguingly, a VHS has a topological characteristic in butterfly physics. At fractional (e.g., 1/q) magnetic flux, the Chern number is ill defined. If the magnetic flux is slightly offset from 1/q at the vicinity of VHS, the Chern number displays an interesting behavior. It continuously undergoes step transition with increasing value when the Fermi energy is tuned towards the VHS from both sides, but the sign of the Chern number is opposite (Fig. 4.12a). In other words, the Chern number undergoes a sudden collapse at VHSs (*128–130*). This behavior can be better understood if one compares it with the Hall conductivity measured at low fields (Fig. 4.8c). The difference is that in the quantum case, the Hall conductivity is quantized and the quantization is characterized by Chern numbers. The collapse is another kind of topological transitions hosted by the Hofstadter's spectrum, is different from the Chern number step-transitions at Landau levels. We next reveal that such transitions play an important role in understanding the photocurrent fan diagram.

We have learned from section 4.6 that such VHS create anomalies in conductivities, thermoelectric coefficients and photocurrents. In Fig. 4.12b we summarize the expected behaviors of these physical quantities at fractal band VHSs in fan diagram. Due to the high electron density of states, σ_{xx} will display a peak at each VHS. Due to the Lifshitz transitions and the effectively zero magnetic field at fractional flux, σ_{xy} will display a four-fold polarity pattern. The S_{xy} and I_{pc} have the same pattern under the physics of photo-Nernst effect, and they will display a two-fold polarity pattern.

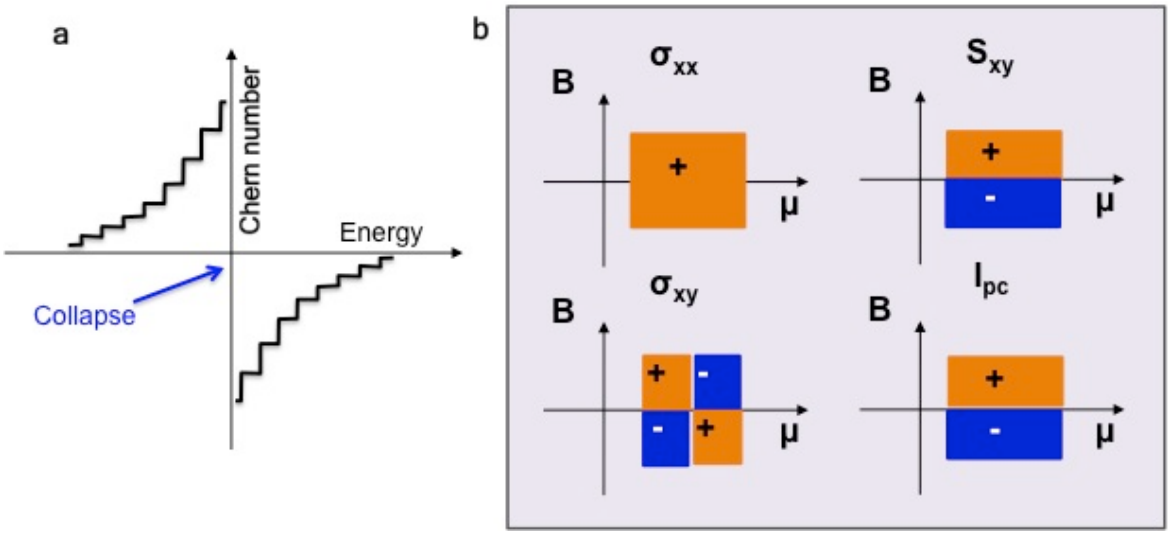

Figure 4.12. Chern number collapse at fractal VHSs. a, the behavior of Chern numbers at the vicinity of a fractal band VHS, where the magnetic flux is slightly offset from the fractional value. b, the theoretically expected polarity patterns of the conductivities, S_{xy} and I_{pc} at fractal VHSs.

Indeed, experimentally we have observed such patterns. In Fig. 4.9a we can clearly see enhanced photocurrents in the miniband regions near each fractional mangnetic flux $\Phi/\Phi_0 = 1/2$, 1/3, 1/4, ... The two-fold polarity pattern is also seen in the Fan diagram. We note that this argument then naturally explains the significantly enhanced photocurrents at the two sides of the Fan diagram. It is due to the VHSs in the fractal bands (which are compactly distributed at the

two sides) that lead to such enhancement. To better show this, in Fig. 4.13 we present the data (with higher resolution) of σ_{xy} and I_{pc}, taken from another superlattice device. In this device, the Moiré wavelength is about 10 nm. The dashed circles indicate the locations of Chern number collapses (VHSs) in fractal minibands. Indeed, at VHSs, the σ_{xy} displays a four-fold polarity pattern and the Ipc displays a two-fold pattern.

In summary, we have demonstrated that the photocurrent generation of graphene/hBN moiré superlattices is a direct manifestation of its topological textures and topological phase transitions. There are two kinds of topological transitions that are essential to the photocurrents: the Chern number step transitions at Landau levels and the Chern number collapses in fractal minibands. The features summarized in section 4.7 can now all be understood.

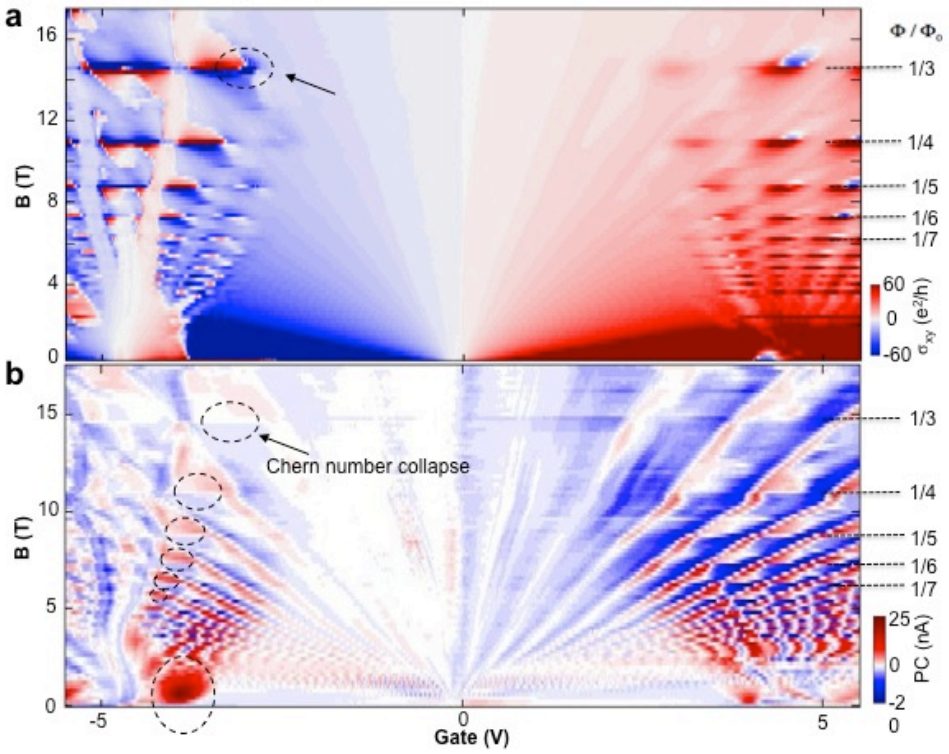

Figure 4.13. Photocurrent Hofstadter's butterfly observed from a second graphene superlattice. The Moiré wavelength in this device is ~ 10 nm. a, σ_{xy} fan diagram. b, I_{pc} fan diagram.

4.11 FUTURE OUTLOOKS: A NEW PROBE TO QHE

In this chapter, we have discussed the optoelectronic responses of graphene/hBN superlattice structure, under the presence of both weak and strong magnetic fields. At weak magnetic fields, we have demonstrated a unique way to achieve multiple hot-carrier collections enabled by the superlattice VHSs. At high fields, we have revealed that the optoelectronic response of such structure is inherently determined by its topological textures and transitions. We believe these studies point out a new point of view to consider graphene's roles both as a candidate material for optoelectronic applications and as a platform for probing new QHE physics. Below I outline the possible future directions for both aspects.

(1) Optoelectronic devices

Although we have achieved device implementations of multiple hot-carrier collections, the experimental conditions are extreme: it requires both low temperature (~4 K) operation and a present of a magnetic field (although weak). Future efforts need to be focus on searching for optimal device geometry that operates under less extreme conditions. For example, fabrication of a sample on a ferromagnetic layer (*131*) may allow us to remove the external magnetic field. Investigation on the p-n junctions of graphene superlattice may be another option, in which the longitudinal thermoelectric power can be employed.

(2) A new probe to QHE

Our measurements have also demonstrated an interesting opportunity of using such optoelectronic probe for detecting the physics of integer and fractional QHE. The fact that the photo-thermoelectricity still dominates the photocurrent generation in QH region is encouraging. It suggests that, in the present of QHE, graphene allows such an interesting region, in which the photoexcited carriers are thermally decoupled from the lattice, i.e., the electrons can be hot while

the lattice stays cool. This can be directly utilized to study the thermal or thermoelectric transport of quantized electronic system. Consequently, the laser in this case can be naturally regarded as a local electronic heater, which avoids complicated fabrication processes in conventional designs. This heater will allow us to minimize the effect of the lattice since only electrons are heated. It can also be scanned spatially, which provides another advantages.

It will allow for the study of some open questions in QHE. For example, it is known that the thermal transport is also quantized similar to the electronic transport in QH region (*132*). However, experimental investigation of heat transport in QHE is extremely difficult. Another example is the existence of a charge-neutral mode in fractional QHE, which is anti-propagating with the charge mode (*133*). This has been long regarded as an essential component in the edge physics of fractional QHE. We envision that, from long-term view, the unique optoelectronic probe presented in this chapter could be helpful in solving these long-standing questions.

Chapter 5. 2D GROWTH: SCALABILITY AND IN-PLANE EPITAXY

In this chapter, we will present a scalable method to synthesize 2D materials, in particular, 2D semiconductors. This is important for any future application of 2D semiconductor. Mechanical exfoliation, although good for much fundamental research, is however, incompatible with any large-scale applications. Available 2D TMD synthesis methods range from liquid exfoliation (*134*), hydrothermal synthesis (*135*), soft sulfurization (*136*), to chemical vapor deposition (CVD) (*137–141*). The CVD method, which was initially developed in 2012 for MoS_2 monolayer growth using a layer of Mo film (*137*) (or MoO_3 powder (*138*)) and sulfur powder as the reactants, is one of the most popular methods. In 2013, we employed physical vapor deposition (PVD), which directly used the TMD powder, for the growth of monolayer semiconductors (*47*, *142*, *143*). This provided a new and simple way to obtain TMD monolayers with high quality. Based on PVD, we have successfully obtained monolayer samples of MoS_2, WSe_2, and $MoSe_2$ and WS_2, in the forms of both isolated single crystals and also a large-area multi-crystalline film, as well as bilayer samples. By slightly modifying our original growth method, we, for the first time, achieved a 2D seamless epitaxial growth of semiconductor lateral heterostructures between WSe_2 and $MoSe_2$. In the following sections, we will discuss the details of PVD synthesis of monolayer TMDs.

5.1 Physical Vapor Deposition

Our growth method is depicted in Fig. 5.1. We place TMD (such as MoS_2) powder source in a crucible that is then loaded into the hot center of a tube furnace system (e.g., CARBOLITE 12/600 1200C Tube Furnace with 1 inch tube diameter). A clean substrate is placed downstream, away from the oven center in a cooler region. The tube is pumped to low pressure and the oxygen contamination is minimized before growth. A carrier gas, typically Ar, will then flow into the tube with constant rate ~ 20 sccm. During growth, the hot center is heated up to ~ 900 or 1000 ^{o}C and the substrate region is kept at ~ 650 ^{o}C. The growth period generally lasts for few minutes to tens of minutes before the furnace is allowed to naturally cool down.

The growth mechanism can be qualitatively understood as following. At the oven center, the surface of MoS2 power evaporates at the high temperature. With the assistance from the carrier gas, the vapor can transport to the cold downstream region and metal and sulfur species deposit onto the substrate. Under right conditions, the deposition can be organized into a single crystal of monolayer TMDs, on variant substrates (*47*).

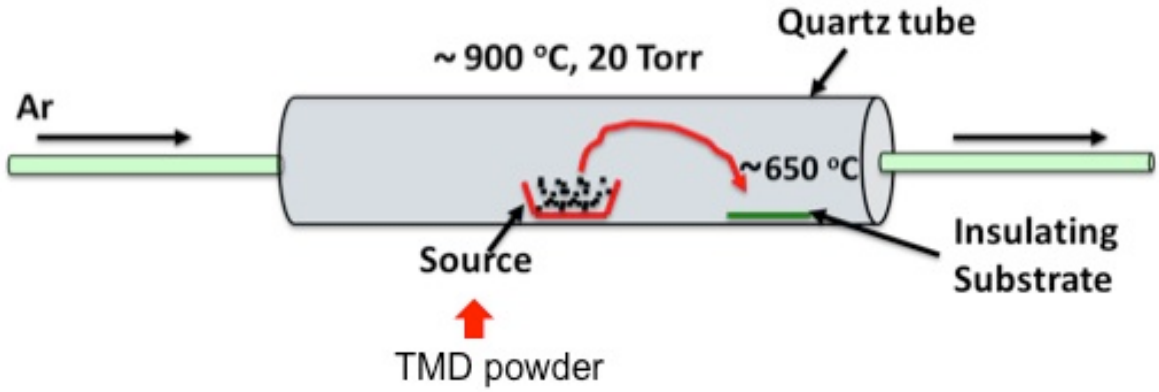

Figure 5.1. Schematic depiction of the PVD growth of TMD monolayers. The TMD powder is loaded to the hot center. During growth, the MoS2 vapor will transport from the hot center to the cold region with the assistance from carrier gas (e.g. Ar). The vapor will then deposit onto the substrate and form a monolayer crystal under proper conditions.

5.2 MONOLAYER TMDS: TRIANGLES

We here present our growth results of monolayer TMDs, in particular MoS_2, on variant insulating substrates, as shown in Fig. 5.2 a-c. Due to the atomic crystal structures, typically the as-grown monolayers yield a triangular shape with lateral size on the order of tens of micrometers. These triangles usually are randomly distributed over a large region on the substrate satisfying the growth conditions. We have succeeded in our growth on three different kinds of substrates: sapphire, 285 nm SiO_2/Si, and glass. In the optical images of the growth, one can also find thick layer depositions other than the monolayers (the white, blue, or black spots), which are usually of much smaller size than the monolayers. The monolayer nature of the growth has been identified by Raman measurements, PL measurements, and atomic force microscopy (AFM) measurements. In Fig. 5.2d, we present a typical AFM image of an as-grown monolayer, where we can see a clean surface and a thickness of ~ 0.75 nm, indicating the formation of high quality monolayers. The characterization details can be found in Ref. (*47*).

The triangular shape is interesting because it suggests the gown monolayers are single crystals. Although it remains unclear what their edge structures are, e.g., whether they are the "zigzag" or the "armchair" configuration (one needs TEM to tell the difference), the advantage over mechanical exfoliation is that the crystal orientation can be readily identified by an optical image, despite the fact that it is indistinguishable between 0^o and 60^o.

We here emphasize that these as-grown monolayers have very high optical quality, indicated by its near-unity valley polarization at low temperature, room temperature PL polarization, and valley coherence. The data has been presented in section 2.5. In comparison, the observation in exfoliated MoS_2 samples identifies no room temperature PL polarization and no valley coherence.

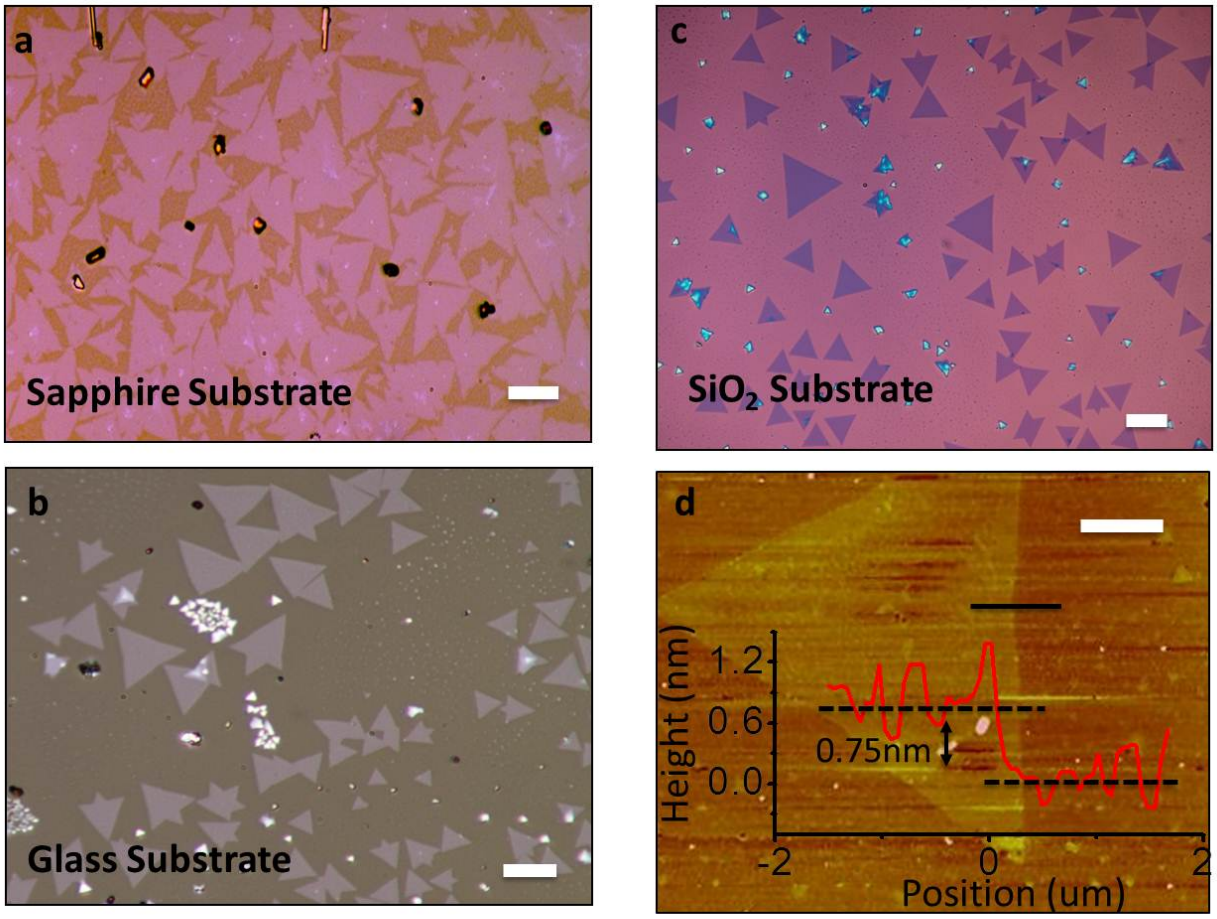

Figure 5.2. Growth of monolayer MoS_2 on variant insulating substrates. a, optical image of a typical monolayer as-grown on sapphire substrate; b, on SiO_2/Si substrate; c, on glass substrate. Scale bars: 10 μm. d, the AFM image and thickness measurement of a grown monolayer triangle. Scale bar: 3 μm. Images are adapted from ref. (*47*), with permission.

5.3 MONOLAYER TMDS: FILMS

In addition to obtain the sparsely distributed monolayer islands, we can also achieve a wafer scale film of TMD monolayer by slighting adjusting the growth conditions. In Fig 5.3, we present our as-grown TMD films (a, MoS_2; b, WS_2) on SiO_2 substrate. One can see that uniform films with millimeter scale can be deposited successfully using our PVD method. We believe that the size of the as-grown monolayers is limited by the size of our tube furnace. Different from the single crystal structures of the above triangles, the films are a polycrystalline structure. They naturally form if the single crystal islands extend their facets and meet at grain boundaries. We find that all the four kinds of TMDs can form such film structures under proper conditions, which allows us to fabricate large arrays of devices using 2D semiconductors from the same growth.

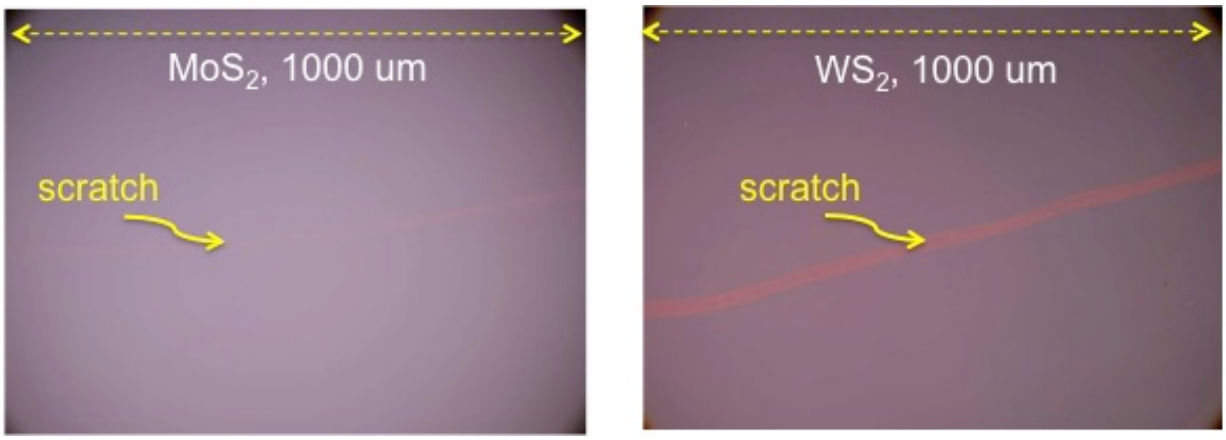

Figure 5.3. Optical images of as-grown TMD monolayer films on wafer scale. a, MoS_2 film; b, WS_2 monolayer film; grown on SiO_2/Si substrates. The scratches are made intentionally on the film by tweezers, in order to enhance the view.

5.4 BILAYER TMDS: AA AND AB STACKING

PVD growth can also give rise to the formation of bilayer TMDs. In this section we will present our growth of bilayer $MoSe_2$ as an example. One can obtain bilayer TMDs from mechanical exfoliation, such as those discussed in section 2.6. In general, exfoliated bilayers (at least for the reported ones) are of inversion symmetry, due to its AB stacking order (Fig. 2.6) (*49*). It is already known that, in such AB stacked bilayer, the bandgap is indirect and consequently the PL quantum yield is much lower than the monolayer samples (*12*). However, we find in our growth bilayers, there are two types.

Fig. 5.4a shows a selected as grown $MoSe_2$ flake, where we can see that one layer is grown on top of the other, forming a bilayer region in connection to single layer regions. The room temperature PL of both the single and bi-layer regions, indicated by the black and red arrow in a respectively, are shown in Fig. 5.4b. It clearly shows that the bilayer PL is not weak compared to the monolayer, as one would expect for AB stacked bilayers. Instead, the PL is as strong as the monolayer samples and behaves actually like two monolayers with slightly different energies. This provides us a clue to associate such bilayer flakes with AA stacking order, where the two layers are simply related by a vertical shift. This is in contrast to the AB stacked bilayers.

In fact, the signatures of both AA and AB stacked bilayer samples can be found in our growth. Fig. 5.4 c and d shows the PL spectra taken at 30 K from two selected as-grown bilayers (see the inset for the optical images). The bilayer in c exhibits very weak PL emission, agreeing with the AB stacked bilayer. The bilayer in d is, however, about ~ 25 times stronger in peak height. In fact, very recently there is a report about the two types of bilayers using CVD growth method (*144*). Further studies are necessary to reveal the true nature of these two bilayer types.

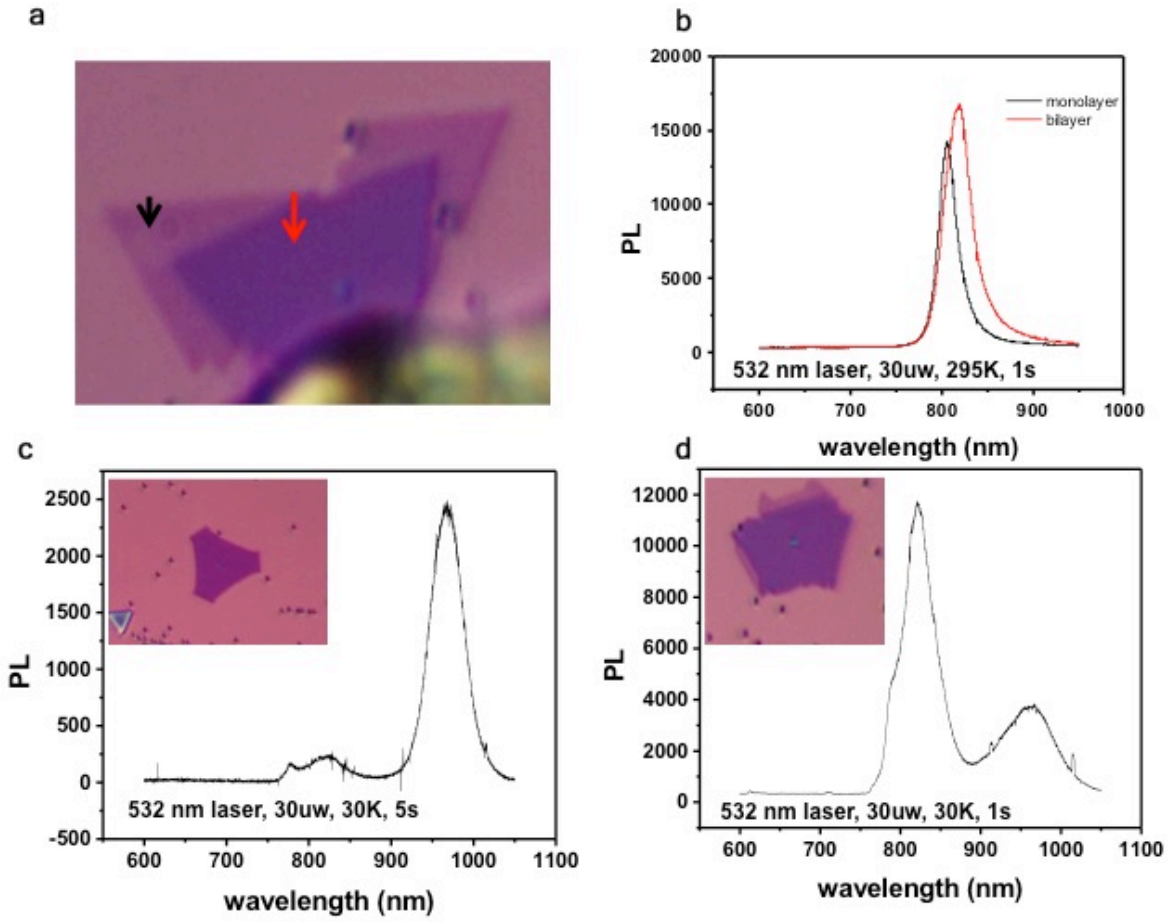

Figure 5.4. PVD as-grown $MoSe_2$ bilayers. a, optical microscope image of a selected piece, where one layer is grown on top of the other, forming both $MoSe_2$ single layer and bilayer regions. b, the PL spectrum taken from single and bi- layer region, indicated by the black and red arrows in a. In this bilayer, the PL spectrum behaves like a combination of two monolayer peaks, indicating a AA stacking order. c and d, Another two bilayer flakes of as-grown $MoSe_2$. The corresponding low-temperature (30K) PL behaves distinctly from each other. One is very weak (c), consistent with the indirect bandgap of AB stacked bilayer. The other (d) is about 25 times stronger than (c), indicating the formation of AA stacked bilayer. All the PL measurements are taken with a 532 nm CW laser with 30 μW excitation power. Insets in c and d are the optical images of the corresponding bilayer flakes. The size of all the three flakes are about ~ 10 um laterally.

5.5 OPTICAL SHG OF THE GROWTH

Second harmonic generation (SHG) is a nonlinear optical process that can be directly used to detect the crystal inversion symmetry. It has been demonstrated that polarization-resolved SHG microscopy can immediately tell us the relative crystal rotations of the present flakes (*147*, *148*). We here present our SHG microscopic data of our as-grown TMD flakes, using a 900 nm laser excitation. Fig 5.5 a and b shows the SHG images taken on PVD grown MoS_2 flakes. One can see that monolayer triangles give rise to strong SHG signals, which is due to the inversion symmetry breaking in the crystal (*36*, *145–148*). In Fig. 5.5b, we have highlighted a piece of two connected flakes, and one isolated flake with a clearly identified center point of growth. Two phenomena can be summarized here. (1) At the grain boundary (*141*) of the two connected flakes, the SHG is enhanced. (2) At the growth center of the isolated flakes, the SHG is also significantly enhanced. With further investigation, these interesting observations may be able to provide new structural information of the grain boundaries and the growth center.

In Fig. 5.5 c and d, we present the data taken from PVD grown WSe_2 flakes. The growth in c exhibits a hexagonal shape of the monolayers, while those in d exhibit triangular shapes. A significantly enhanced SHG at the six edges of each hexagon are found. In contrast, no such edge enhancement has been found to the triangles. We believe this is interesting and further understanding will require the identification of the atomic structures of these edges and also their chemical environments.

Another interesting observation can be made in Fig 5.5d. We found that, in addition to the monolayer triangles, there are also other types of triangular flakes with either enhanced or quenched SHG signal. This agrees well with our previous identification of AA (inversion asymmetric) and AB (inversion symmetric) stacked bilayers.

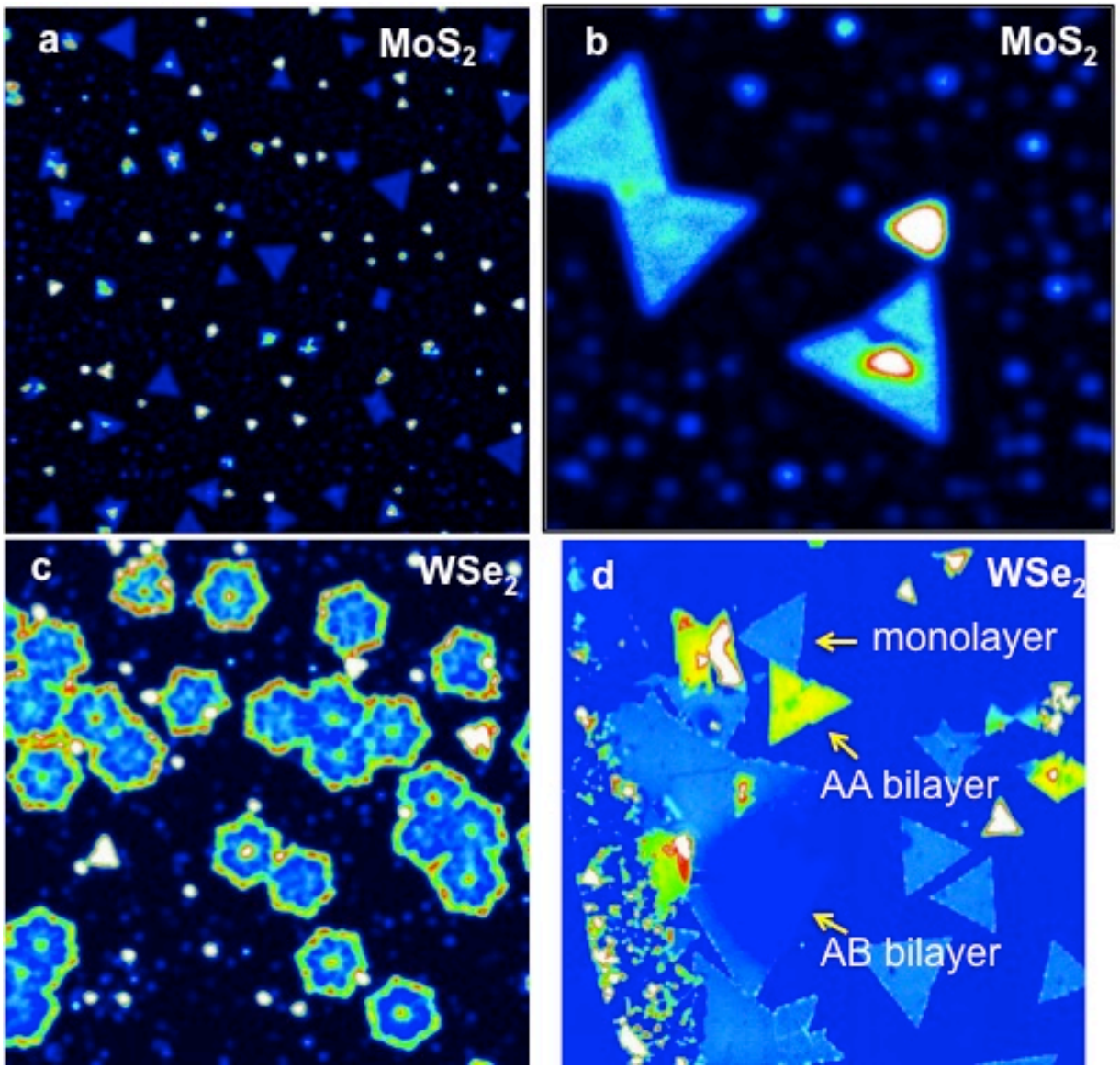

Figure 5.5. SHG microscopic images of as-grown TMD flakes. a and b, monolayer triangles of MoS_2. c, Hexagonal flakes of monolayer WSe_2. The edge of the flakes shows enhanced SHG signal. d, Triangular flakes of monolayer and bilayer WSe_2. Through the SHG intensity, we have identified the flakes of monolayer, AA stacked bilayer, and AB stacked bilayer. Darker color: lower intensity; Brighter color: higher intensity. The lateral size of each triangular or hexagon is on the order of ten micrometers.

5.6 BEYOND ONE CRYSTAL: IN-PLANE EPITAXIAL GROWTH

Epitaxial heterojunctions between 3D Semiconductors plays an important role in developing LEDs, diode lasers and high-speed transistors. It achieves atomically seamless junctions between two semiconducting crystals with similar lattice structures. Here we propose one way to achieve such epitaxial heterostructures between 2D semiconductors, which represents an epitaxial growth technique in an atomic plane (*142*, *149–155*).

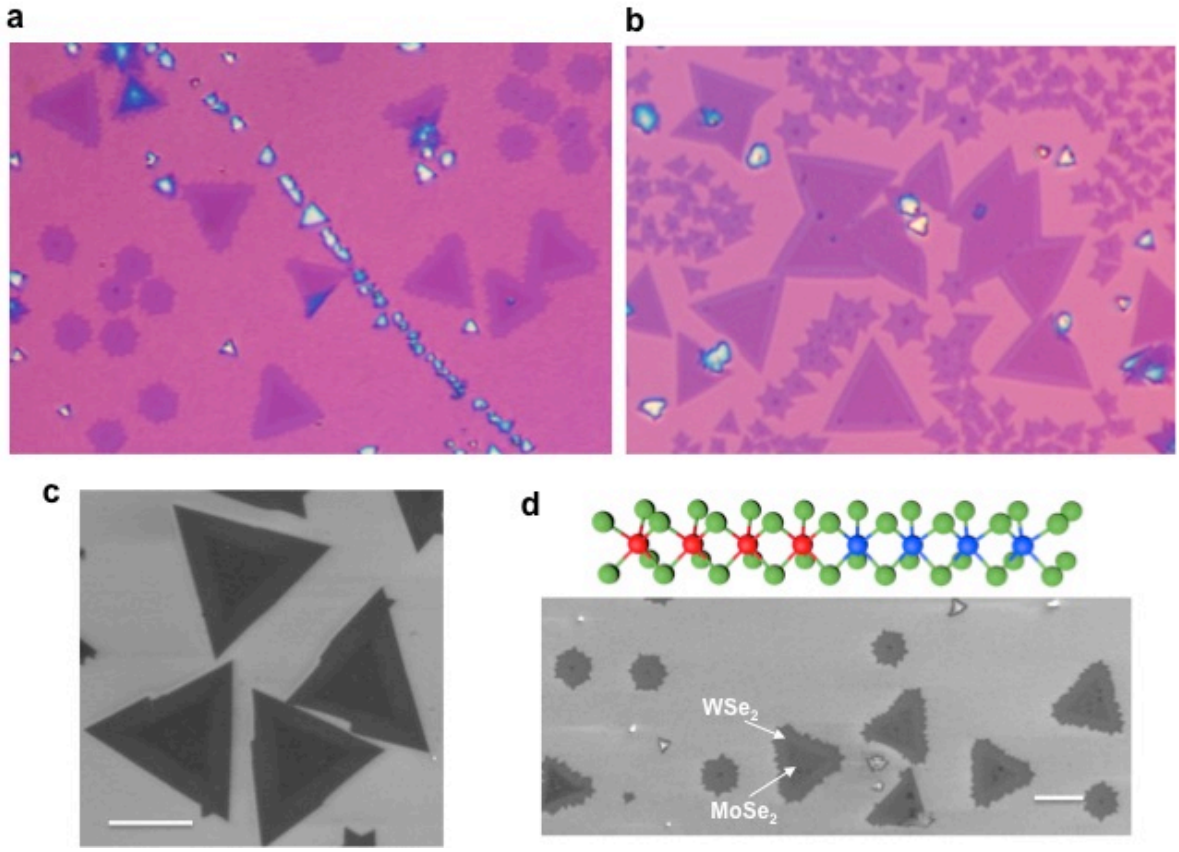

Figure 5.6. As-grown structures when the powder source is an equal mixture of MoS_2 and WSe_2. a and b, optical images of two different growths. One can find that, in each flake, there are concentric triangular shapes, indicating the formation of two different materials in a single monolayer piece. c and d, SEM images of the flakes, which also confirms the concentric shapes. Carton in d depicting the lateral heterojunction of $MoSe_2$ and WSe_2.

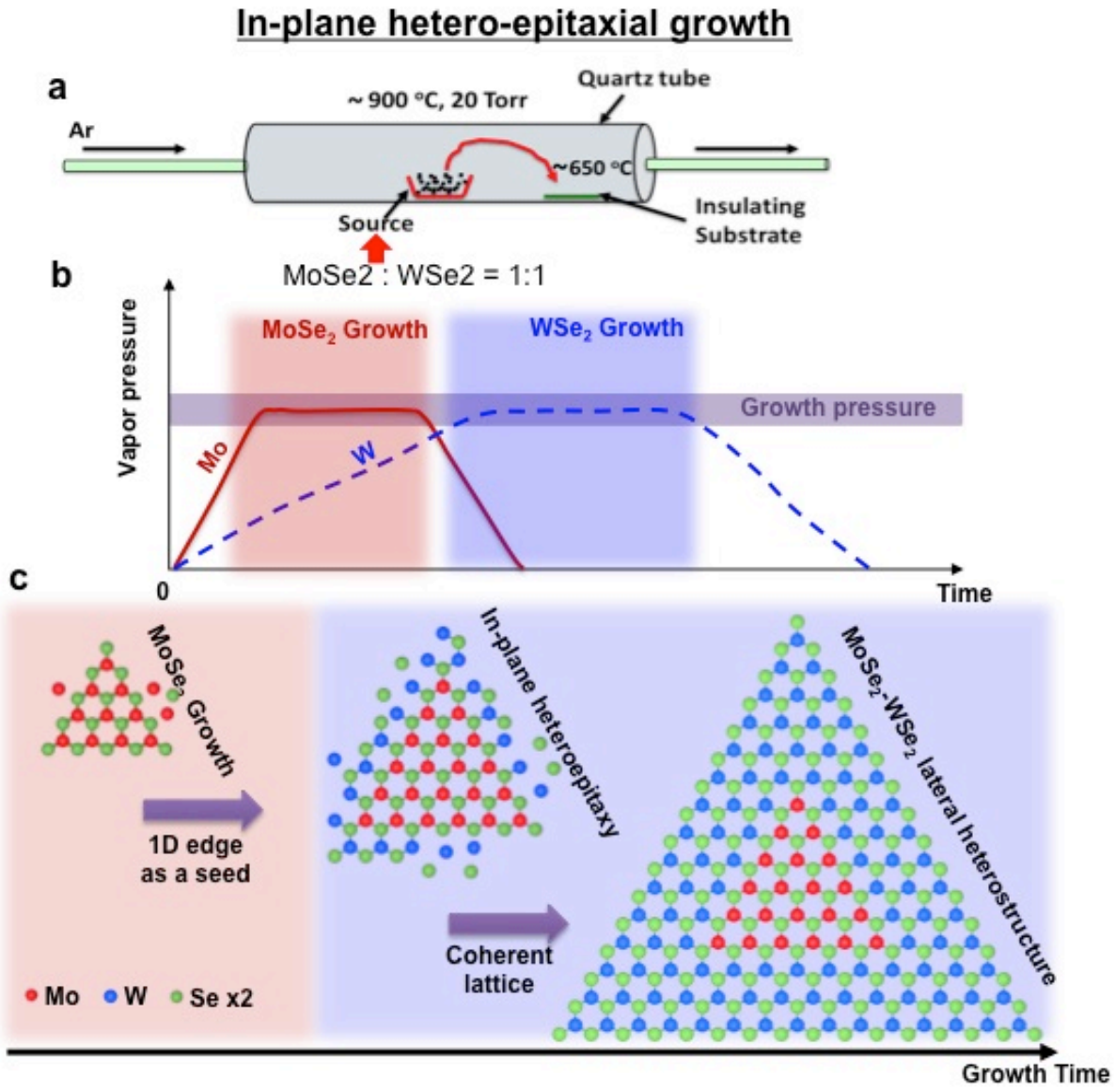

Figure 5.7. In-plane epitaxial growth mechanism. a, Cartoon depicting the growth conditions, where the source is placed by an equal mixture of WSe_2 and $MoSe_2$. b, The proposed mechanism during growth. Upon the heating by oven, $MoSe_2$ is first vaporized and deposited onto the substrate, leading to the $MoSe_2$ monolayer growth with nucleation on the substrate. After a certain time, the surface $MoSe_2$ degrades and the monolayer stops growing, while the W species starts vaporizing. The growth of WSe_2 seeds on the existing $MoSe_2$ crystals and the in-plane heteroepitaxy begins. A coherent lattice structure between the two different monolayer materials forms. At the end, the W vapors also degrade due to the surface depletion of the source. This process is summarized in c.

The method is naturally allowed in our PVD method, by simply replacing the source of a single species of TMD powders by an equal mixture of two species. For example, in Fig. 5.6 we show our results on a SiO_2/Si substrate after we put a 1:1 mixture of WSe_2 and $MoSe_2$ in the crucible and run a growth. WSe_2 and $MoSe_2$ have the same crystal structure, where only the transition metal is substituted - even the lattice constant matches very well from each other (3.280 Å and 3.288 Å). Fig. 5.6 a and b show the optical images from two different growths. Although there are differences between the edges of flakes, there are obviously two concentric triangles in every single flake for both growths. We can further confirm such concentric structures by scanning electron microscopic (SEM) images in Fig. 5.6 c and d. It is strikingly different from the growth with single TMD sources. We will later confirm that this is due to the formation of a lateral WSe_2-$MoSe_2$ heterostructure in the atomic plane. The inside darker triangle is a monolayer $MoSe_2$ and the outside brighter region is a monolayer WSe_2. The two kinds of monolayer semiconductors are seamless connected with crystalline perfection, forming a 2D epitaxial semiconductor heterojunction.

We propose the growth mechanism as follows. During the early process $MoSe_2$ is favored potentially due to the different vaporization temperature of the two materials. Pure $MoSe_2$ monolayers randomly grow on the substrate just similar to the single-source growth. However, after certain time, the growth conditions, such as the vapor pressure of transition metal atoms, switch in favor of the growth of WSe_2 (Fig. 5.7 a and b). Unlike $MoSe_2$ growth, the WSe_2 growth can directly seed on the edges of existing $MoSe_2$ crystals due to the similarity between the two crystals. This will finally leads to a coherent lattice structure between the two different monolayer materials and forms a 2D lateral heterojunction. We suspect that the switch between the two growths can be understood by two effects: (1) the different volatility of the $MoSe_2$ and

WSe_2 source powders and (2) the depletion of the powder surfaces. Combining the two conditions, we can sketch the growth process in Fig. 5.7b, where the MoSe2 and WSe2 growth are naturally separated in time. It allows a 2D epitaxial growth without any external action during the time of growth. This method therefore maintains ideal conditions for epitaxy with minimal disturbance and contamination.

5.7 LATERAL HETEROSTRUCTURES

The detailed characterization of the lateral heterostuctures can be found in Ref. (*142*). We here only present our inspection of the junction region under high-resolution scanning transmission electron microscope (STEM). The measurement was performed in University of Warwick at UK. Fig. 5.8a shows the data, where the brightness of the dots can be used to identify the atomic species (see the inset). One can clearly see the transition from $MoSe_2$ (left bottom, darker) to WSe_2 (right top, brighter), confirming the lateral $MoSe_2$-WSe_2 junction. The Fourier transform of the entire image (in a) is shown in Fig. 5.8 b, where a single hexagonal lattice is seen. It demonstrates the coherent lattice structure between the two different monolayer regions, confirming the 2D epitaxial growth in our method.

The current growth, although successful in obtaining the seamless heterojunctions, has not achieved an atomically sharp interface, which can also be seen in the STEM image. The region of atomic substitutions is on the order of few nanometers, containing randomly distributed "defects" mostly in WSe_2 lattice. We summarize two types of defects in Fig. 5.8 c and d, where the W atom is substituted by Mo atom with either a single site or multiple sites. With future improvement on the furnace conditions, we expect to see a sharper transition.

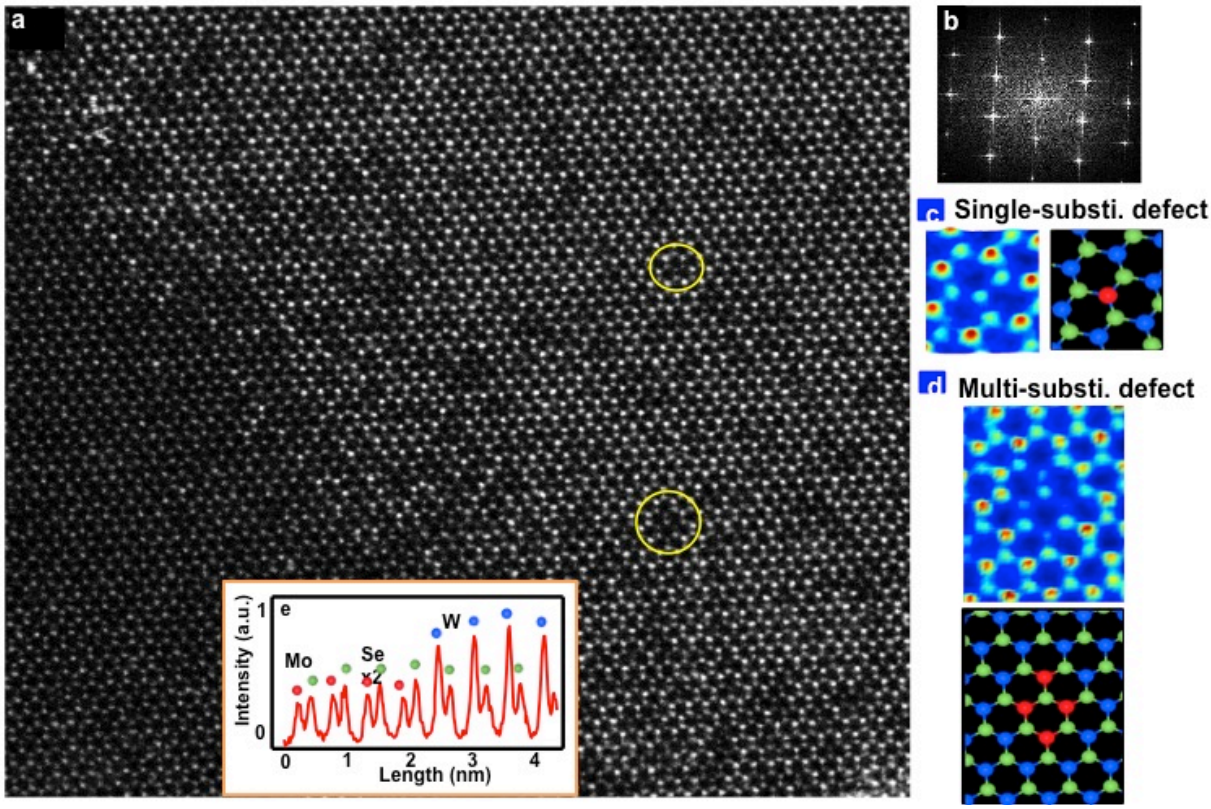

Figure 5.8. High-resolution STEM image of the lateral $MoSe_2$-WSe_2 heterojunction. a, the aberration-corrected TEM image shows the lattice structure of the heterointerfaces. The intensity (brightness) of the dot identifies the atomic spices since it directly reflects the atomic weight. Inset shows the intensity along a selected line of atoms. b, the FFT image of a, which shows a single hexagonal lattice of the heterojunction, indicating the coherent lattice. c, colored SEM image and its cartoon depiction of a defect with single metal substitution, shown by the smaller yellow circle in a. d,the same for a defect with multiple metal substitutions, shown by the bigger yellow circle in a.

5.8 FUTURE OUTLOOKS

In this chapter, we have presented our PVD method for 2D semiconductor growth. It provides a scalable way to synthesize TMD monolayers in response to the future large-scale applications. We have demonstrated the ability of PVD to grow isolated monolayers, continuous wafer-scale

film, bilayers and also lateral heterostructures. We believe that PVD growth technique can be widely applied to synthesize variant interesting 2D structures, both for fundamental studies and also for device applications. Here we summarize the potential future directions related to the topics presented in the above sections.

We have only presented the synthesis of novel structures, such as the bilayer TMDs and lateral heterostructures. There are a lot of opportunities in studying their physical properties. For example, we have already known that at the lateral heterostructures, there are significantly enhanced PL and we have also presented interesting SHG data of the grown structures. Efforts need to be directed to understand these observations, reveal the electronic and optoelectronic properties and also construct functional devices.

One may further improve the growth techniques in the future. For example, an upgraded PVD system equipped with multiple temperature zones with independent heaters will allow us to perform precise control over the growth stages. This will significantly increase the freedom in designing the growth, which, for instance, could lead to a programmable growth of heterostructure. Based on such improvements, we may also be able to synthesize new atomic structures in 2D. One example could be a 1D quantum-well in the atomic plane, where one material with only atomically narrow width is sandwiched in between a different material through the 2D epitaxial technique. Such 1D interface effects could be very interesting in many directions, ranging from atomic scale electronics and photonics to the search for topological electronic states.

The growth of other 2D crystals, beyond the four kinds of semiconducting TMD presented above, will also be interesting. In the family of TMD, there are also semi-metallic species, such as WTe_2 and $MoTe_2$, and superconducting species such as $NbSe_2$ and NbS_2. There

are also many kinds of perovskites whose monolayers have never been obtained. PVD synthesis of new kinds of 2D materials will certainly generate interest.

BIBLIOGRAPHY

1. A. H. Castro Neto, N. M. R. Peres, K. S. Novoselov, A. K. Geim, The electronic properties of graphene. *Rev. Mod. Phys.* **81**, 109–162 (2009).

2. Y. Zhang, Y.-W. Tan, H. L. Stormer, P. Kim, Experimental observation of the quantum Hall effect and Berry's phase in graphene. *Nature*. **438**, 201–4 (2005).

3. K. S. Novoselov *et al.*, Two-dimensional gas of massless Dirac fermions in graphene. *Nature*. **438**, 197–200 (2005).

4. K. I. Bolotin, F. Ghahari, M. D. Shulman, H. L. Stormer, P. Kim, Observation of the fractional quantum Hall effect in graphene. *Nature*. **462**, 196–9 (2009).

5. C. R. Dean *et al.*, Hofstadter's butterfly and the fractal quantum Hall effect in moiré superlattices. *Nature*. **497**, 598–602 (2013).

6. B. Hunt, J. Sanchez-Yamagishi, Massive Dirac fermions and Hofstadter butterfly in a van der Waals heterostructure. *Science*. **340**, 1427–1431 (2013).

7. L. a Ponomarenko *et al.*, Cloning of Dirac fermions in graphene superlattices. *Nature*. **497**, 594–7 (2013).

8. L. Wang *et al.*, Evidence for a fractional fractal quantum Hall effect in graphene superlattices. *Science (80-.).* **350**, 1231–4 (2015).

9. K. S. Novoselov *et al.*, Two-dimensional atomic crystals. *Proc. Natl. Acad. Sci. U. S. A.* **102**, 10451–3 (2005).

10. A. K. Geim, I. V Grigorieva, Van der Waals heterostructures. *Nature*. **499**, 419–25 (2013).

11. J. Ge *et al.*, Superconductivity above 100 K in single-layer FeSe films on doped SrTiO3. *Nat. Mater.* **14**, 285–9 (2015).

12. K. F. Mak, C. Lee, J. Hone, J. Shan, T. F. Heinz, Atomically Thin MoS2: A New Direct-Gap Semiconductor. *Phys. Rev. Lett.* **105**, 136805 (2010).

13. A. Splendiani *et al.*, Emerging photoluminescence in monolayer MoS2. *Nano Lett.* **10**, 1271–5 (2010).

14. D. Xiao, G.-B. Liu, W. Feng, X. Xu, W. Yao, Coupled Spin and Valley Physics in Monolayers of MoS2 and Other Group-VI Dichalcogenides. *Phys. Rev. Lett.* **108**, 196802 (2012).

15. D. Xiao, W. Yao, Q. Niu, Valley-contrasting physics in graphene: Magnetic moment and topological transport. *Phys. Rev. Lett.* **99** (2007), doi:10.1103/PhysRevLett.99.236809.

16. W. Yao, D. Xiao, Q. Niu, Valley-dependent optoelectronics from inversion symmetry breaking. *Phys. Rev. B*. **77**, 235406 (2008).

17. A. Pospischil, M. M. Furchi, T. Mueller, Solar-energy conversion and light emission in an atomic monolayer p-n diode. *Nat. Nanotechnol.* **9**, 257–61 (2014).

18. B. W. H. Baugher, H. O. H. Churchill, Y. Yang, P. Jarillo-Herrero, Optoelectronic devices based on electrically tunable p-n diodes in a monolayer dichalcogenide. *Nat. Nanotechnol.* **9**, 262–7 (2014).

19. B. Radisavljevic, A. Radenovic, J. Brivio, V. Giacometti, A. Kis, Single-layer MoS2 transistors. *Nat. Nanotechnol.* **6**, 147–50 (2011).

20. O. Lopez-Sanchez, D. Lembke, M. Kayci, A. Radenovic, A. Kis, Ultrasensitive photodetectors based on monolayer MoS2. *Nat. Nanotechnol.* **8**, 497–501 (2013).

21. J. S. Ross *et al.*, Electrically tunable excitonic light-emitting diodes based on monolayer WSe2 p-n junctions. *Nat. Nanotechnol.* **9**, 268–72 (2014).

22. A. Pospischil, M. M. Furchi, T. Mueller, Solar-energy conversion and light emission in an atomic monolayer p-n diode. *Nat. Nanotechnol.* **9**, 257–61 (2014).

23. R. S. Sundaram *et al.*, Electroluminescence in single layer MoS2. *Nano Lett.* **13**, 1416–21 (2013).

24. S. Wu *et al.*, Monolayer semiconductor nanocavity lasers with ultralow thresholds. *Nature*. **520**, 69–72 (2015).

25. Y. Ye *et al.*, Monolayer excitonic laser. *Nat. Photonics*. **9**, 733–737 (2015).

26. O. Salehzadeh, M. Djavid, N. H. Tran, I. Shih, Z. Mi, Optically Pumped Two-Dimensional MoS2 Lasers Operating at Room-Temperature. *Nano Lett.* **15**, 5302–6 (2015).

27. X. Xu, W. Yao, D. Xiao, T. F. Heinz, Spin and pseudospins in layered transition metal dichalcogenides. *Nat. Phys.* **10**, 343–350 (2014).

28. T. Cao *et al.*, Valley-selective circular dichroism of monolayer molybdenum disulphide. *Nat. Commun.* **3**, 887 (2012).

29. H. Zeng, J. Dai, W. Yao, D. Xiao, X. Cui, Valley polarization in MoS2 monolayers by optical pumping. *Nat. Nanotechnol.* **7**, 490–3 (2012).

30. K. F. Mak, K. He, J. Shan, T. F. Heinz, Control of valley polarization in monolayer MoS2 by optical helicity. *Nat. Nanotechnol.* **7**, 494–8 (2012).

31. J. S. Ross *et al.*, Electrical control of neutral and charged excitons in a monolayer semiconductor. *Nat. Commun.* **4**, 1474 (2013).

32. K. F. Mak *et al.*, Tightly bound trions in monolayer MoS2. *Nat. Mater.* **12**, 207–11 (2013).

33. K. Kheng *et al.*, Observation of negatively charged excitons X- in semiconductor quantum wells. *Phys. Rev. Lett.* **71**, 1752–1755 (1993).

34. A. M. Jones *et al.*, Optical generation of excitonic valley coherence in monolayer WSe2. *Nat. Nanotechnol.* **8**, 634–8 (2013).

35. K. He *et al.*, Tightly bound excitons in monolayer WSe2. *Phys. Rev. Lett.* **113** (2014), doi:10.1103/PhysRevLett.113.026803.

36. H. Zeng *et al.*, Optical signature of symmetry variations and spin-valley coupling in atomically thin tungsten dichalcogenides. *Sci. Rep.* **3**, 1608 (2013).

37. Z. Ye *et al.*, Probing Excitonic Dark States in Single-layer Tungsten Disulfide. *Nature*. **5**, 214–218 (2014).

38. Y. You *et al.*, Observation of biexcitons in monolayer WSe2. *Nat. Phys.* (2015), doi:10.1038/nphys3324.

39. H. M. Gibbs, G. Khitrova, S. W. Koch, Exciton–polariton light–semiconductor coupling effects. *Nat. Photonics*. **5**, 273–273 (2011).

40. X. Liu, T. Galfsky, Z. Sun, F. Xia, E. Lin, Strong light-matter coupling in two-dimensional atomic crystals. *arXiv:*, 1406.4826 (2014).

41. H. Yu, X. Cui, X. Xu, W. Yao, Valley excitons in two-dimensional semiconductors. *Natl. Sci. Rev.* **2**, 57–70 (2014).

42. H. Yu, G.-B. Liu, P. Gong, X. Xu, W. Yao, Dirac cones and Dirac saddle points of bright excitons in monolayer transition metal dichalcogenides. *Nat. Commun.* **5**, 3876 (2014).

43. S. Wu *et al.*, Electrical tuning of valley magnetic moment through symmetry control in bilayer MoS2. *Nat. Phys.* **9**, 149–153 (2013).

44. R. V Gorbachev *et al.*, Detecting topological currents in graphene superlattices. *Science*. **346**, 448–51 (2014).

45. Y. Zhang *et al.*, Direct observation of a widely tunable bandgap in bilayer graphene. *Nature*. **459**, 820–3 (2009).

46. M. Sui *et al.*, Gate-tunable topological valley transport in bilayer graphene. *Nat. Phys.* **11**, 1027–1031 (2015).

47. S. Wu *et al.*, Vapor-solid growth of high optical quality MoS_2 monolayers with near-unity valley polarization. *ACS Nano*. **7**, 2768–72 (2013).

48. Y. Wu, Q. Tong, G.-B. Liu, H. Yu, W. Yao, Spin-valley qubit in nanostructures of monolayer semiconductors: Optical control and hyperfine interaction. *Phys. Rev. B*. **93**, 045313 (2016).

49. S. Wu *et al.*, Electrical tuning of valley magnetic moment through symmetry control in bilayer MoS2. *Nat. Phys.* (2013), doi:10.1038/nphys2524.

50. S. Wu *et al.*, Electrical tuning of valley magnetic moment through symmetry control in bilayer MoS2. *Nat. Phys.* (2013), doi:10.1038/nphys2524.

51. P. L. Mak, Kin Fai, McGill, K. L., Park, J. McEuen, Observation of the valley Hall effect. *submitted* (2014).

52. G. Aivazian *et al.*, Magnetic control of valley pseudospin in monolayer WSe2. *Nat. Phys.* **11**, 148–152 (2015).

53. A. Srivastava *et al.*, Valley Zeeman effect in elementary optical excitations of monolayer WSe2. *Nat. Phys.* **11**, 141–147 (2015).

54. D. MacNeill *et al.*, Breaking of valley degeneracy by magnetic field in monolayer MoSe2. *Phys. Rev. Lett.* **114**, 037401 (2015).

55. C. H. Lui *et al.*, Trion-induced negative photoconductivity in monolayer MoS2. *Phys. Rev. Lett.* **113**, 166801 (2014).

56. F. Withers *et al.*, Light-emitting diodes by band-structure engineering in van der Waals heterostructures. *Nat. Mater.* **14**, 301–6 (2015).

57. A. Srivastava *et al.*, Optically active quantum dots in monolayer WSe2. *Nat. Nanotechnol.* **10**, 491–6 (2015).

58. C. Chakraborty, L. Kinnischtzke, K. M. Goodfellow, R. Beams, A. N. Vamivakas, Voltage-controlled quantum light from an atomically thin semiconductor. *Nat. Nanotechnol.* **10**, 507–11 (2015).

59. Y.-M. He *et al.*, Single quantum emitters in monolayer semiconductors. *Nat. Nanotechnol.* **10**, 497–502 (2015).

60. M. Koperski *et al.*, Single photon emitters in exfoliated WSe2 structures. *Nat. Nanotechnol.* **10**, 503–6 (2015).

61. D. Yoon *et al.*, Atomically thin quantum light emitting diodes. *arXiv:1603.08795* (2016).

62. P. Rivera *et al.*, Observation of long-lived interlayer excitons in monolayer MoSe2-WSe2 heterostructures. *Nat. Commun.* **6**, 6242 (2015).

63. P. Rivera *et al.*, Valley-polarized exciton dynamics in a 2D semiconductor heterostructure. *Science (80-.).* **351**, 688–691 (2016).

64. L. Ju *et al.*, Topological valley transport at bilayer graphene domain walls. *Nature*. **520**, 650–5 (2015).

65. J. M. Lu *et al.*, Evidence for two-dimensional Ising superconductivity in gated MoS_2. *Science (80-.).* **350**, 1353–7 (2015).

66. Y. Saito *et al.*, Superconductivity protected by spin–valley locking in ion-gated MoS2. *Nat. Phys.* **12**, 144–149 (2015).

67. X. Xi *et al.*, Ising pairing in superconducting NbSe2 atomic layers. *Nat. Phys.* **12**, 139–143 (2015).

68. F. Xia, H. Wang, D. Xiao, M. Dubey, A. Ramasubramaniam, Two-dimensional material nanophotonics. *Nat. Photonics*. **8**, 899–907 (2014).

69. K. F. Mak, J. Shan, Photonics and optoelectronics of 2D semiconductor transition metal dichalcogenides. *Nat. Photonics*. **10**, 216–226 (2016).

70. J. D. Joannopoulos, P. R. Villeneuve, S. Fan, Photonic crystals: putting a new twist on light. *Nature*. **386**, 143–149 (1997).

71. K. Rivoire, A. Faraon, J. Vuckovic, Gallium phosphide photonic crystal nanocavities in the visible. *Appl. Phys. Lett.* **93**, 063103 (2008).

72. N. Susumu, F. Masayuki, A. Takashi, Spontaneous-emission control by photonic crystals and nanocavities. *Nat. Photonics* (2007).

73. W.-H. Chang *et al.*, Efficient single-photon sources based on low-density quantum dots in photonic-crystal nanocavities. *Phys. Rev. Lett.* **96**, 117401 (2006).

74. T. Yoshie *et al.*, Vacuum Rabi splitting with a single quantum dot in a photonic crystal nanocavity. **432**, 9–12 (2004).

75. S. Strauf *et al.*, Self-Tuned Quantum Dot Gain in Photonic Crystal Lasers. *Phys. Rev. Lett.* **96**, 127404 (2006).

76. B. Ellis *et al.*, Ultralow-threshold electrically pumped quantum-dot photonic-crystal nanocavity laser. *Nat. Photonics*. **5**, 297–300 (2011).

77. L. Andreani, F. Bassani, Exchange interaction and polariton effects in quantum-well excitons. *Phys. Rev. B*. **41**, 7536–7544 (1990).

78. H. Deng, H. Haug, Y. Yamamoto, Exciton-polariton Bose-Einstein condensation. *Rev. Mod. Phys.* **82**, 1489–1537 (2010).

79. X. Liu *et al.*, Strong light–matter coupling in two-dimensional atomic crystals. *Nat. Photonics*. **9**, 30–34 (2014).

80. S. Dufferwiel *et al.*, Exciton-polaritons in van der Waals heterostructures embedded in tunable microcavities. *Nat. Commun.* **6**, 8579 (2015).

81. O. Painter *et al.*, Two-dimensional photonic band-Gap defect mode laser. *Science*. **284**, 1819–21 (1999).

82. S. Noda, Photonic crystal lasers — ultimate nanolasers and broad-area coherent lasers [Invited]. **27**, 1–8 (2010).

83. S. Eshlaghi, W. Worthoff, A. D. Wieck, D. Suter, Luminescence upconversion in GaAs quantum wells. *Phys. Rev. B - Condens. Matter Mater. Phys.* **77** (2008), doi:10.1103/PhysRevB.77.245317.

84. S. Strauf, F. Jahnke, Single quantum dot nanolaser. *Laser Photon. Rev.* **5**, 607–633 (2011).

85. S. Wu *et al.*, Control of two-dimensional excitonic light emission via photonic crystal. *2D Mater.* **1**, 011001 (2014).

86. X. Gan *et al.*, Controlling the spontaneous emission rate of monolayer MoS2 in a photonic crystal nanocavity. *Appl. Phys. Lett.* **103**, 181119 (2013).

87. M. Fujita, S. Takahashi, Y. Tanaka, T. Asano, S. Noda, Simultaneous inhibition and redistribution of spontaneous light emission in photonic crystals. *Science*. **308**, 1296–8 (2005).

88. M. Nomura, N. Kumagai, S. Iwamoto, Y. Ota, Y. Arakawa, Laser oscillation in a strongly coupled single-quantum-dot–nanocavity system. *Nat. Phys.* **6**, 279–283 (2010).

89. O. Painter, Two-Dimensional Photonic Band-Gap Defect Mode Laser. *Science (80-.).* **284**, 1819–1821 (1999).

90. M. Khajavikhan *et al.*, Thresholdless nanoscale coaxial lasers. *Nature*. **482**, 204–7 (2012).

91. Y.-J. Lu *et al.*, Plasmonic nanolaser using epitaxially grown silver film. *Science*. **337**, 450–3 (2012).

92. G. Björk, A. Karlsson, Y. Yamamoto, On the linewidth of microcavity lasers. *Appl. Phys. Lett.* **60**, 304 (1992).

93. C. Henry, Theory of the linewidth of semiconductor lasers. *Quantum Electron. IEEE J.*, 259–264 (1982).

94. J. M. S. Lucas C. Flatten, Zhengyu He, David M. Coles, Aurelien A. P. Trichet, Alex W. Powell, Robert A. Taylor, Jamie H. Warner, Room-temperature exciton-polaritons with two-dimensional WS2. *arXiv:1605.04743* (2016) (available at http://arxiv.org/abs/1605.0474).

95. X. Gan *et al.*, Strong enhancement of light-matter interaction in graphene coupled to a photonic crystal nanocavity. *Nano Lett.* **12**, 5626–31 (2012).

96. A. Majumdar, J. Kim, J. Vuckovic, F. Wang, Electrical control of silicon photonic crystal cavity by graphene. *Nano Lett.* **13**, 515–8 (2013).

97. J. L. O'Brien, A. Furusawa, J. Vučković, Photonic quantum technologies. *Nat. Photonics*. **3**, 687–695 (2009).

98. A. Majumdar *et al.*, Hybrid 2D Material Nanophotonics: A Scalable Platform for Low-Power Nonlinear and Quantum Optics. *ACS Photonics*. **2**, 1160–1166 (2015).

99. K. S. Novoselov *et al.*, Electric field effect in atomically thin carbon films. *Science (80-.).* **306**, 666–9 (2004).

100. Y. Zhao, P. Cadden-Zimansky, Z. Jiang, P. Kim, Symmetry breaking in the zero-energy Landau level in bilayer graphene. *Phys. Rev. Lett.* **104**, 066801 (2010).

101. M. Kharitonov, Phase diagram for the $\nu = 0$ quantum Hall state in monolayer graphene. *Phys. Rev. B*. **85**, 155439 (2012).

102. C. R. Dean *et al.*, Boron nitride substrates for high-quality graphene electronics. *Nat. Nanotechnol.* **5**, 722–6 (2010).

103. L. Wang *et al.*, One-dimensional electrical contact to a two-dimensional material. *Science*. **342**, 614–7 (2013).

104. M. Yankowitz *et al.*, Emergence of superlattice Dirac points in graphene on hexagonal boron nitride. *Nat. Phys.* **8**, 382–386 (2012).

105. C. Park, L. Yang, Y. Son, M. L. Cohen, S. G. Louie, Anisotropic behaviours of massless Dirac fermions in graphene under periodic potentials. *Nat. Phys.* **4**, 213–217 (2008).

106. C.-H. Park, L. Yang, Y.-W. Son, M. L. Cohen, S. G. Louie, New generation of massless Dirac fermions in graphene under external periodic potentials. *Phys. Rev. Lett.* **101**, 126804 (2008).

107. J. R. Wallbank, a. a. Patel, M. Mucha-Kruczyński, a. K. Geim, V. I. Fal'ko, Generic miniband structure of graphene on a hexagonal substrate. *Phys. Rev. B*. **87**, 245408 (2013).

108. D. R. Hofstadter, Energy levels and wave functions of Bloch electrons in rational and irrational magnetic fields. *Phys. Rev. B*. **14**, 2239 (1976).

109. G. H. Wannier, A Result Not Dependent on Rationality for Bloch Electrons in a Magnetic Field. *Phys. Status Solidi*. **88**, 757–765 (1978).

110. J. Zak, Magnetic Translation Group. *Phys. Rev.* **134**, A1602–A1606 (1964).

111. X. Xu, N. M. Gabor, J. S. Alden, A. M. van der Zande, P. L. McEuen, Photo-thermoelectric effect at a graphene interface junction. *Nano Lett.* **10**, 562–6 (2010).

112. N. M. Gabor *et al.*, Hot carrier-assisted intrinsic photoresponse in graphene. *Science*. **334**, 648–52 (2011).

113. J. Song, M. Rudner, C. Marcus, L. Levitov, Hot carrier transport and photocurrent response in graphene. *Nano Lett.*, 4688–4692 (2011).

114. J. C. W. Song, K. J. Tielrooij, F. H. L. Koppens, L. S. Levitov, Photoexcited carrier dynamics and impact-excitation cascade in graphene. *Phys. Rev. B*. **87**, 155429 (2013).

115. D. Sun *et al.*, Ultrafast hot-carrier-dominated photocurrent in graphene. *Nat. Nanotechnol.* **7**, 114–8 (2012).

116. K. J. Tielrooij *et al.*, Generation of photovoltage in graphene on a femtosecond timescale through efficient carrier heating. *Nat. Nanotechnol.* **10**, 437–443 (2015).

117. H. Cao *et al.*, Photo-Nernst current in graphene. *Nat. Phys.* (2015), doi:10.1038/nphys3549.

118. W. Yang *et al.*, Epitaxial growth of single-domain graphene on hexagonal boron nitride. *Nat. Mater.* **12**, 792–7 (2013).

119. S. Wu *et al.*, Multiple hot-carrier collection in photo-excited graphene Moiré superlattices. *Sci. Adv.* **1**, 1–7 (2016).

120. F. H. L. Koppens *et al.*, Photodetectors based on graphene, other two-dimensional materials and hybrid systems. *Nat. Nanotechnol.* **9**, 780–793 (2014).

121. T. Winzer, A. Knorr, E. Malic, Carrier multiplication in graphene. *Nano Lett.* **10**, 4839–43 (2010).

122. K. J. Tielrooij *et al.*, Photoexcitation cascade and multiple hot-carrier generation in graphene. *Nat. Phys.* **9**, 248–252 (2013).

123. J. C. Johannsen *et al.*, Tunable carrier multiplication and cooling in graphene. *Nano Lett.* **15**, 326–31 (2015).

124. T. Plötzing *et al.*, Experimental verification of carrier multiplication in graphene. *Nano Lett.* **14**, 5371–5 (2014).

125. D. Brida *et al.*, Ultrafast collinear scattering and carrier multiplication in graphene. *Nat. Commun.* **4**, 1987 (2013).

126. Y. M. Zuev, W. Chang, P. Kim, Thermoelectric and Magnetothermoelectric Transport Measurements of Graphene. *Phys. Rev. Lett.* **102**, 096807 (2009).

127. C. A. Nelson, N. R. Monahan, X.-Y. Zhu, Exceeding the Shockley–Queisser limit in solar energy conversion. *Energy Environ. Sci.* **6**, 3508 (2013).

128. G. Naumis, I. Satija, Topological Map of the Hofstadter Butterfly Macroscopic Chern Annihilations and Van Hove Singularities. *arxiv*. **1507.0813** (2015) (available at http://arxiv.org/abs/1507.0813).

129. R. Markiewicz, The topological significance of saddle point van Hove singularities: a comparison of orbital switching and magnetic breakdown. *J. Phys. Condens. Matter*. **6**, 3059–3072 (1994).

130. Y. Hatsugai, T. Fukui, H. Aoki, Topological analysis of the quantum Hall effect in graphene: Dirac-Fermi transition across van Hove singularities and edge versus bulk quantum numbers. *Phys. Rev. B*. **74**, 205414 (2006).

131. P. Wei, et al, Strong Interfacial Exchange Field in 2D Material / Magnetic-Insulator Heterostructures : Graphene / EuS. *arXiv:1510.05920* (2015).

132. C. L. Kane, M. P. A. Fisher, Quantized thermal transport in the fractional quantum Hall effect. *Phys. Rev. B*. **55**, 15832–15837 (1997).

133. A. Bid *et al.*, Observation of neutral modes in the fractional quantum Hall regime. *Nature*. **466**, 585–90 (2010).

134. G. Eda *et al.*, Photoluminescence from chemically exfoliated MoS2. *Nano Lett.* **11**, 5111–6 (2011).

135. Y. Peng *et al.*, Hydrothermal Synthesis and Characterization of Single-Molecular-Layer MoS2 and MoSe2. *Chem. Lett.*, 772–773 (2001).

136. H. Hadouda, J. Pouzet, J. C. Bernede, A. Barreau, MoS2 thin film synthesis by soft sulfurization of a molybdenum layer. *Mater. Chem. Phys.* **42**, 291–297 (1995).

137. Y. Zhan, Z. Liu, S. Najmaei, P. M. Ajayan, J. Lou, Large-Area Vapor-Phase Growth and Characterization of MoS2 Atomic Layers on a SiO2 Substrate. *Small*. **8**, 966–971 (2012).

138. Y.-H. Lee *et al.*, Synthesis of large-area MoS2 atomic layers with chemical vapor deposition. *Adv. Mater.* **24**, 2320–5 (2012).

139. X. Lu *et al.*, Large-area synthesis of monolayer and few-layer MoSe2 films on SiO2 substrates. *Nano Lett.* **14**, 2419–2425 (2014).

140. J.-K. Huang *et al.*, Large-Area and Highly Crystalline WSe2 Monolayers: from Synthesis to Device Applications (2013) (available at http://arxiv.org/abs/1304.7365).

141. A. M. van der Zande *et al.*, Grains and grain boundaries in highly crystalline monolayer molybdenum disulphide. *Nat. Mater.* **12**, 554–61 (2013).

142. C. Huang *et al.*, Lateral heterojunctions within monolayer MoSe2–WSe2 semiconductors. *Nat. Mater.* **13**, 1096–1101 (2014).

143. G. Clark *et al.*, Vapor-transport growth of high optical quality WSe2 monolayers a. *APL Mater.* **2**, 101101 (2014).

144. M. Xia *et al.*, Spectroscopic Signatures of AA' and AB Stacking of Chemical Vapor Deposited Bilayer MoS2. *ACS Nano*. **9**, 12246–54 (2015).

145. N. Kumar *et al.*, Second harmonic microscopy of monolayer MoS2. *Phys. Rev. B*. **87**, 161403 (2013).

146. L. M. Malard, T. V. Alencar, A. P. M. Barboza, K. F. Mak, A. M. de Paula, Observation of intense second harmonic generation from MoS2 atomic crystals. *Phys. Rev. B*. **87**, 201401 (2013).

147. K. L. Seyler *et al.*, Electrical control of second-harmonic generation in a WSe2 monolayer transistor. *Nat. Nanotechnol.* (2015), doi:10.1038/nnano.2015.73.

148. X. Yin *et al.*, Edge nonlinear optics on a MoS_2 atomic monolayer. *Science (80-.).* **344**, 488–90 (2014).

149. M. P. Levendorf *et al.*, Graphene and boron nitride lateral heterostructures for atomically thin circuitry. *Nature*. **488**, 627–32 (2012).

150. Z. Liu *et al.*, In-plane heterostructures of graphene and hexagonal boron nitride with controlled domain sizes. *Nat. Nanotechnol.* **8**, 119–24 (2013).

151. L. Liu *et al.*, Heteroepitaxial growth of two-dimensional hexagonal boron nitride templated by graphene edges. *Science (80-.).* **343**, 163–7 (2014).

152. X. Duan *et al.*, Lateral epitaxial growth of two-dimensional layered semiconductor heterojunctions. *Nat. Nanotechnol.* **9**, 1024–30 (2014).

153. Y. Gong *et al.*, Vertical and in-plane heterostructures from WS2/MoS2 monolayers. *Nat. Mater.* **13**, 1135–42 (2014).

154. X. Zhang, C. Lin, Y. Tseng, K. Huang, Y. Lee, Synthesis of lateral heterostructures of semiconducting atomic layers. *Nano Lett.* **15**, 410–5 (2015).

155. M.-Y. Li *et al.*, Epitaxial growth of a monolayer WSe2-MoS2 lateral p-n junction with an atomically sharp interface. *Science (80-.).* **349**, 524–8 (2015).

VITA

Wu was born to Qilai Xie and Youfang Wu in a village near the city of Hefei in Anhui province of China. He attended Hefei 168 high school in 2003, where he started to gain curiosity in physics. After graduation, he went to study physics at the University of Science and Technology of China in the same city in 2006. It is during this period he greatly enjoyed the beauty of physics and he learned how to think as a physicist. After graduation in 2010, he spent a short time at the College of William and Mary at Williamsburg, and in 2011 he moved to University of Washington at Seattle for his Ph.D. study in experimental condensed matter physics. After five years of research in a laboratory, working with his advisor, Prof. Xiaodong Xu, he learned how to discover and solve problems as a physicist.